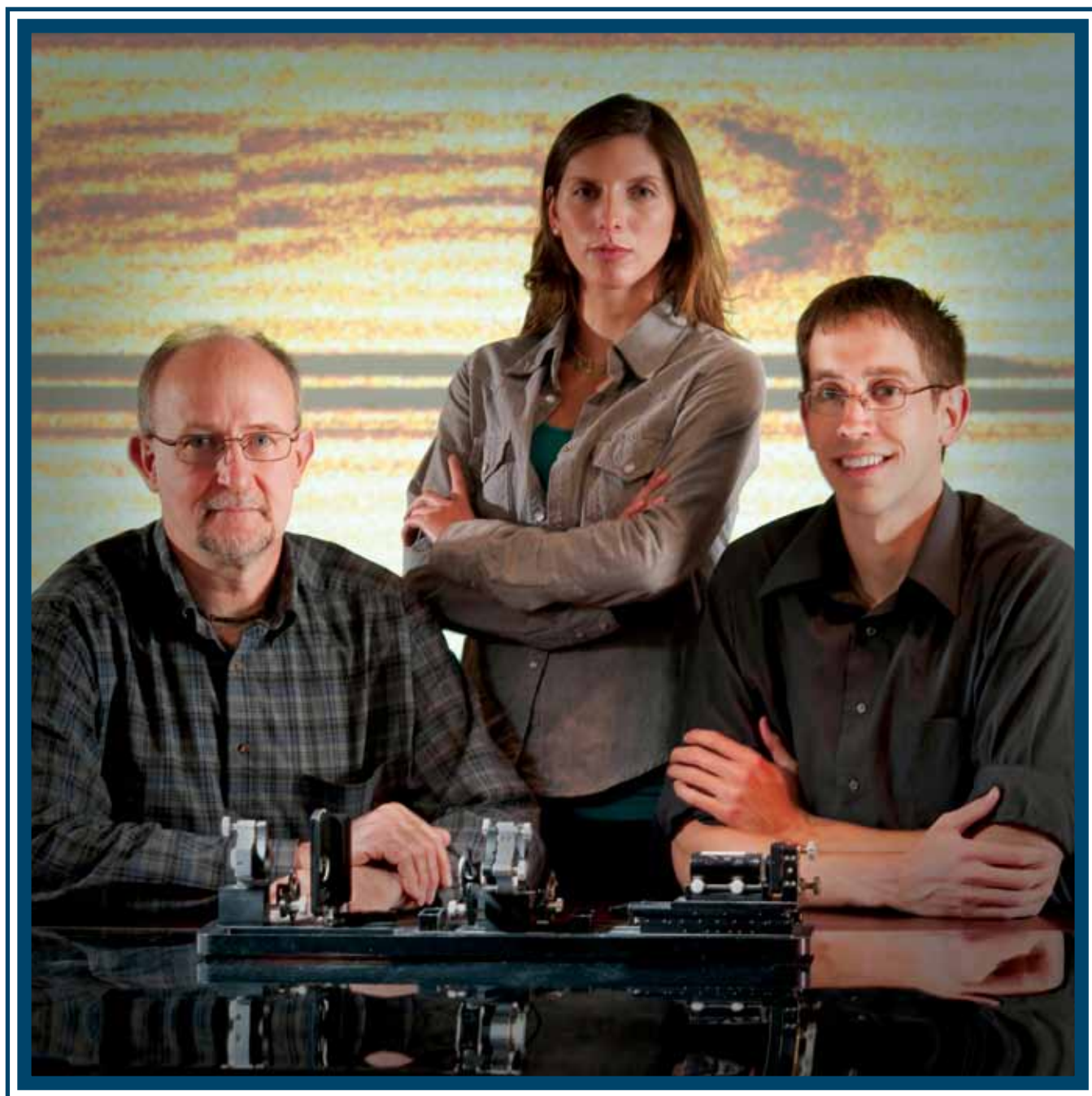


LLE Review

Quarterly Report



About the Cover:

A critical part of the National Ignition Campaign (NIC) is the accurate timing of the shock waves used to quasi-isentropically compress the fuel before its implosion. To accomplish this, a series of tuning experiments will be performed at the National Ignition Facility (NIF). A team of scientists from LLE, LLNL, and SNL, led by LLE Scientist Tom Boehly, have used the OMEGA Laser System to investigate and demonstrate the necessary techniques to measure the timing of shock waves in ignition targets on the NIF (see "Demonstration of the Shock-Timing Technique for Ignition Targets at the National Ignition Facility," p. 1). In the cover photo, Dr. Boehly (left) is shown with Ph.D. students Maria Barrios and Dayne Fratanduono (right), who study shock waves and the behavior of materials at high pressures. In the foreground is a velocity interferometer for any reflector (VISAR) from the OMEGA Laser System. The background is an image of the VISAR streak camera data from a shock-timing experiment conducted on OMEGA (see Fig. 117.8).



The inside-cover photo shows a complete VISAR system (identical to the one on the OMEGA Laser System) that was used to produce the measurements for the feature article. The system pictured will be installed on OMEGA EP to study the behavior of materials at extreme pressures. To the right are two ROSS (Rochester Optical Streak System) cameras (gray boxes) that detect and image the VISAR signals. To the left are two interferometers (black optical assemblies) that detect shock velocity. Experimental Laboratory Engineer Mike Cruz (pictured) designed and fabricated the VISAR systems for both the OMEGA and OMEGA EP Laser Systems.

This report was prepared as an account of work conducted by the Laboratory for Laser Energetics and sponsored by New York State Energy Research and Development Authority, the University of Rochester, the U.S. Department of Energy, and other agencies. Neither the above named sponsors, nor any of their employees, makes any warranty, expressed or implied, or assumes any legal liability or responsibility for the accuracy, completeness, or usefulness of any information, apparatus, product, or process disclosed, or represents that its use would not infringe privately owned rights. Reference herein to any specific commercial product, process, or service by trade name, mark, manufacturer, or otherwise, does not necessarily constitute or imply its endorsement, recommendation, or favoring

by the United States Government or any agency thereof or any other sponsor. Results reported in the LLE Review should not be taken as necessarily final results as they represent active research. The views and opinions of authors expressed herein do not necessarily state or reflect those of any of the above sponsoring entities.

The work described in this volume includes current research at the Laboratory for Laser Energetics, which is supported by New York State Energy Research and Development Authority, the University of Rochester, the U.S. Department of Energy Office of Inertial Confinement Fusion under Cooperative Agreement No. DE-FC52-08NA28302, and other agencies.

Printed in the United States of America
Available from
National Technical Information Services
U.S. Department of Commerce
5285 Port Royal Road
Springfield, VA 22161
Price codes: Printed Copy A04
Microfiche A01

For questions or comments, contact Wade A. Bittle, Editor, Laboratory for Laser Energetics, 250 East River Road, Rochester, NY 14623-1299, (585) 273-3053.

Worldwide-Web Home Page: <http://www.lle.rochester.edu/>

LLE Review



Quarterly Report

Contents

In Brief	iii
Demonstration of the Shock-Timing Technique for Ignition Targets at the National Ignition Facility	1
Cryogenic Target Performance and Implosion Physics Studies on OMEGA	12
Diagnosing Fuel ρR and ρR Asymmetries in Cryogenic DT Implosions Using Charged-Particle Spectrometry on OMEGA	20
Plasma Density Determination from X-Ray Radiography of Laser-Driven Spherical Implosions	26
Integrated Simulations of Implosion, Electron Transport, and Heating for Direct-Drive Fast-Ignition Targets	31
Shear Stress in Magnetorheological Finishing for Glasses	42
Effective Verdet Constant in Terbium-Doped-Core Phosphate Fiber	51
Publications and Conference Presentations	

In Brief

This volume of the LLE Review, covering October–December 2008, features “Demonstration of the Shock-Timing Technique for Ignition Targets at the National Ignition Facility” by T. R. Boehly, V. N. Goncharov, S. X. Hu, J. A. Marozas, T. C. Sangster, D. D. Meyerhofer (LLE), D. Munro, P. M. Celliers, D. G. Hicks, G. W. Collins, H. F. Robey, O. L. Landen (LLNL), and R. E. Olson (SNL). In this article (p. 1) the authors report on a technique to measure the velocity and timing of shock waves in a capsule contained within hohlraum targets. This technique is critical for optimizing the drive profiles for high-performance inertial-confinement-fusion capsules, which are compressed by multiple precisely timed shock waves. The shock-timing technique was demonstrated on OMEGA using surrogate hohlraum targets heated to 180 eV and fitted with a re-entrant cone and quartz window to facilitate velocity measurements using velocity interferometry. Cryogenic experiments using targets filled with liquid deuterium further demonstrated the entire timing technique in a hohlraum environment. Direct-drive cryogenic targets with multiple spherical shocks were also used to validate this technique, including convergence effects at relevant pressures (velocities) and sizes. These results provide confidence that shock velocity and timing can be measured in NIF ignition targets, thereby optimizing these critical parameters.

Additional highlights of recent research presented in this issue include the following:

- V. A. Smalyuk, R. Betti, T. R. Boehly, R. S. Craxton, J. A. Delettrez, D. H. Edgell, V. Yu. Glebov, V. N. Goncharov, D. R. Harding, S. X. Hu, J. P. Knauer, F. J. Marshall, R. L. McCrory, P. W. McKenty, D. D. Meyerhofer, P. B. Radha, S. P. Regan, T. C. Sangster, W. Seka, R. W. Short, S. Skupsky, J. M. Soures, C. Stoeckl, B. Yaakobi (LLE), D. Shvarts (Nuclear Research Center, Negev, Israel), J. A. Frenje, C. K. Li, R. D. Petrasso, and F. H. Séguin (Plasma Science Fusion Center, MIT) review recent progress in direct-drive, cryogenic implosions at the Omega Laser Facility (p. 12). Ignition-relevant areal densities of $\sim 200 \text{ mg/cm}^2$ in cryogenic D_2 implosions with peak laser-drive intensities of $\sim 5 \times 10^{14} \text{ W/cm}^2$ were previously reported. The laser intensity is being increased to $\sim 10^{15} \text{ W/cm}^2$ to demonstrate ignition-relevant implosion velocities of 3 to $4 \times 10^7 \text{ cm/s}$, providing an understanding of the relevant target physics. Planar-target acceleration experiments show the importance of the nonlocal electron-thermal-transport effects for modeling the laser drive. Nonlocal, hot-electron preheat is observed to stabilize the Rayleigh–Taylor growth at the peak drive intensity of $\sim 10^{15} \text{ W/cm}^2$. The shell preheat caused by the hot electrons generated by two-plasmon-decay (TPD) instability was reduced by using Si-doped ablaters. The measured compressibility of planar plastic targets driven with high-compression, shaped pulses agrees well with 1-D simulations at these intensities. Shock mistiming has contributed to compression degradation of recent cryogenic implosions driven with continuous pulses. Multiple-picket (shock-wave) target designs make it possible for a more robust tuning of the shock-wave arrival times. Cryogenic implosions driven with double-picket pulses demonstrate improved compression performance at a peak drive intensity of $\sim 10^{15} \text{ W/cm}^2$.
- J. A. Frenje, C. K. Li, F. H. Séguin, D. T. Casey, R. D. Petrasso (Plasma Science Fusion Center, MIT), T. C. Sangster, R. Betti, V. Yu. Glebov, and D. D. Meyerhofer (LLE) describe a new method for analyzing the spectrum of knock-on deuterons (KOD's) elastically scattered by primary DT neutrons, from which a fuel ρR can be inferred for values up to $\sim 200 \text{ mg/cm}^2$ (p. 20). This new analysis method, which used Monte Carlo modeling of a cryogenic DT implosion, significantly improves the previous analysis

method in two fundamental ways: First, it is not affected by significant spatial-yield variations, which degrade the diagnosis of fuel ρR (spatial-yield variations of about $\pm 20\%$ are typically observed), and secondly, it does not break down when the fuel ρR exceeds ~ 70 mg/cm².

- F. J. Marshall, P. W. McKenty, J. A. Delettrez, R. Epstein, J. P. Knauer, V. A. Smalyuk (LLE), J. A. Frenje, C. K. Li, R. D. Petrasso, F. H. Séguin (Plasma Science Fusion Center, MIT), and R. C. Mancini (Department of Physics, University of Nevada, Reno, Nevada) describe a method from which the cold fuel layer density is inferred from framed x-ray radiographs of a laser-driven spherical implosion (p. 26). The density distribution is determined by using Abel inversion to compute the radial distribution of the opacity κ from the observed optical depth τ . With the additional assumption of the mass of the remaining cold fuel, the absolute density distribution can be determined. This is demonstrated on the Omega Laser Facility with two x-ray backlighters of different mean energies that lead to the same inferred density distribution independent of backlighter energy.
- A. A. Solodov, K. S. Anderson, R. Betti, V. Gotcheva, J. Myatt, J. A. Delettrez, S. Skupsky, W. Theobald, and C. Stoeckl (LLE) present integrated simulations of implosion, electron transport, and heating for direct-drive fast-ignition targets (p. 31). A thorough understanding of future integrated fast-ignition experiments combining compression and heating for high-density thermonuclear fuel requires hybrid (fluid + particle) simulations of the implosion and ignition process. Different spatial and temporal scales need to be resolved to model the entire fast-ignition experiment. The two-dimensional (2-D) axisymmetric hydrocode *DRACO* and the 2-D/three-dimensional hybrid-PIC code *LSP* have been integrated to simulate the implosion and heating of direct-drive, fast-ignition targets. *DRACO* includes the physics required to simulate compression, ignition, and burn of fast-ignition targets. *LSP* simulates the transport of hot electrons from their generation site to the dense fuel core where their energy is absorbed. The results from integrated simulations of cone-in-shell CD targets designed for fast-ignition experiments on the OMEGA-OMEGA EP Laser System are presented. Target heating and neutron yields are computed. The results from *LSP* simulations of electron transport in solid-density plastic targets are also presented. They confirm an increase in the electron-divergence angle with the laser intensity in the current experiments. The self-generated resistive magnetic field is found to collimate the hot-electron beam and increase the coupling efficiency of hot electrons with the target. Resistive filamentation of the hot-electron beam is also observed.
- C. Miao, S. N. Shafrir, J. C. Lambropoulos, J. Mici, and S. D. Jacobs (LLE) report *in-situ*, simultaneous measurements of both drag and normal forces in magnetorheological optical finishing (MRF) using a spot-taking machine (STM) as a test bed to take MRF spots on stationary optical parts (p. 42). The force measurements are carried out over the entire removal area, produced by the projected area of the MRF removal function/spot on the part surface, using a dual-force sensor. This approach experimentally addresses the mechanisms governing material removal in MRF for optical glasses in terms of the hydrodynamic pressure and shear stress, applied by the hydrodynamic flow of magnetorheological (MR) fluid at the gap between the part surface and the STM wheel. This work demonstrates that the volumetric removal rate shows a positive linear dependence on shear stress. Shear stress exhibits a positive linear dependence on a material figure of merit that depends on Young's modulus, fracture toughness, and hardness. A modified Preston's equation is proposed that will better estimate MRF material removal rate for optical glasses by incorporating mechanical properties, shear stress, and velocity.

- L. Sun, J. D. Zuegel, J. R. Marciante (LLE), and S. Jiang (AdValue Photonics, Inc.) propose and experimentally validate the concept of effective Verdet constant to describe the Faraday rotation characteristics of optical fiber (p. 51). The effective Verdet constant of light propagation in fiber includes contributions from the materials in both the core and the cladding. This article presents a measured Verdet constant in 25-wt% terbium-doped-core phosphate fiber to be -6.2 ± 0.4 rad/Tm at a wavelength of 1053 nm, which is $6\times$ larger than in silica fiber. The result agrees well with the Faraday rotation theory for optical fiber.

Wade A. Bittle
Editor

Demonstration of the Shock-Timing Technique for Ignition Targets at the National Ignition Facility

Introduction

Ignition experiments at the National Ignition Facility (NIF) will use x rays in indirect-drive (hohlraum) targets to drive implosions of capsules containing deuterium–tritium (DT) fuel.¹ These inertial confinement fusion (ICF) targets use three shock waves to quasi-isentropically compress the capsule before the main compression wave drives the implosion of the fuel assembly.² The goal is to minimize the required drive energy by minimizing the entropy imparted to the capsule as it is imploded. To achieve ignition, both the strength and timing of the shock and compression waves must be accurately set.

The National Ignition Campaign (NIC) is a multi-laboratory program³ that designed and will perform experiments that lead to ignition on the NIF. The campaign includes various tuning experiments that iteratively optimize the laser and target parameters to achieve specified conditions and maximize target performance. To achieve optimal shock conditions, experiments using optical diagnostics will detect the shock-velocity temporal profiles, providing both the strength and timing of the various shocks within the capsule fuel.⁴ The tuning campaign will use these data to adjust the laser (and, therefore, x-ray) drive until the shock strengths and timings meet design specifications. These experiments require surrogate targets that make it possible to diagnostically access the inside of the capsule but closely mimic the behavior of the ignition targets. The ignition capsule in these targets has a re-entrant Au cone filled with liquid deuterium and extends out beyond the hohlraum wall.⁵ With these targets, optical diagnostics can detect spherically converging shock waves within the deuterium-filled capsule.

Optical diagnostics can readily measure both shock velocity and timing to the precision and accuracy required for ignition target designs. These measurements, taken in a cryogenic capsule embedded in a hohlraum and driven to radiation temperatures in excess of 150 eV, present considerable challenges. To demonstrate that this is a viable technique for the NIF, experiments were performed at the Omega Laser Facility.⁶ This article discusses the resolution of several issues associated with

this approach and demonstrates that this technique is a valid method to time shocks in ignition targets on the NIF.

Shock Timing

ICF targets are spherical shells that have a layer of solid (cryogenic) DT fuel that must be compressed to 1000 g/cc on a low adiabat and then heated to ~5 keV to initiate ignition and burn.¹ This compression is produced by the ablation process that can be driven either directly or indirectly by laser beams. In the indirect case, the capsule is contained in a cylindrical hohlraum that is irradiated by many high-power laser beams that produce up to a 1×10^{15} W/cm² flux of thermal x rays that drive an ablative implosion of the capsule. Target design is a delicate optimization of maximizing fuel compression while minimizing the internal energy imparted to the pusher and fuel. The primary approach is to approximate an isentropic compression using a series of three shock waves of increasing strength, followed by a compression wave that drives the compressed shell of fuel to implode at velocities of $\sim 3.6 \times 10^7$ cm/s. Shock waves provide discrete “markers” that will be used to diagnose the compression history. The steps in drive pressure (that produce the shocks) are controllable parameters that make it possible for the compression to be optimized while controlling entropy increases. Shock waves are also desirable for ablators that may have a spatial structure that can be smoothed out by the melting produced by a first shock.⁷

In its simplest form, an ICF target is a two-layer system—an ablator surrounding a layer of DT ice. (Actual ablators have internal layers of varied composition to enhance the absorption and ablation processes.⁸) For optimal target performance each shock must have the correct strength. Specification requires that the velocity be set to a precision of 1%. The shocks must arrive at the inner DT-fuel surface in a tight sequence, with their launch times known to a precision of 50 ps (Ref. 4). The assembled mass is swept inward by the compression wave that must be timed to a precision of 100 ps. When properly tuned in strength and timing, the shocks minimize the adiabat (internal energy) of the DT fuel, keeping it on a low isentrope. By

arriving at the inner surface of the ice in a tightly controlled sequence, most of the fuel has been shocked and re-shocked along a low adiabat.

If the later, stronger shocks overtake the first shock too early, a large portion of the fuel is heated by this strong shock and will be on a higher adiabat and be harder to compress. Late coalescence means that previous shocks have time to unload significant material from the inner surface of the ice, creating a low-density blowoff that would be significantly heated by the subsequent shocks, again placing the fuel on a higher isentrope.

Temporal profiles of the laser and resultant radiation temperature need to produce the desired shock strengths and timing. The residual uncertainties in the calculated hohlraum drive and the opacity and equation of state (EOS) of the ablator and fuel require full-scale tuning experiments to achieve the precision required for ignition. The NIC includes experiments that will iteratively “fine tune” the drive to optimize shock timing. Critical to this effort are precise measurements of shock timing in surrogate targets that are equivalent to ignition targets.

Figure 117.1(a) depicts the Lagrangian trajectories of four shocks through the ablator and DT ice. For optimal performance, these shocks should arrive at the inner DT-ice surface in a tight temporal sequence.⁴ The laser pulse shape for ignition targets is shown schematically in Fig. 117.1(b), along with the expected radiation temperature in the hohlraum. The steps in the radiation temperature launch three successive shocks with pressures of approximately 0.8, 4, and 12 Mb in the DT fuel. The main compression wave begins with pressures greater than 40 Mb. (Individual designs vary these values slightly.)

Since the EOS of deuterium is known,⁹ a measurement of the shock velocity provides all the pertinent information about the shock wave. The NIC shock-timing campaign will use shock-velocity measurements to iteratively adjust the level and timing of each “step” in power to produce the desired shock velocity (pressure) and timing. Knowledge of the temporal velocity profiles provides, through integration, the positions of shock coalescence.

The velocity interferometry system for any reflector (VISAR)¹⁰ probe beam is reflected off the leading shock front (the one closest to VISAR). At these pressures, shock-compressed deuterium is a metal-like reflector that is opaque to visible light.¹¹ The following shock fronts cannot be viewed inside the opaque medium; instead, they are detected only when they overtake or coalesce with the leading shock front.

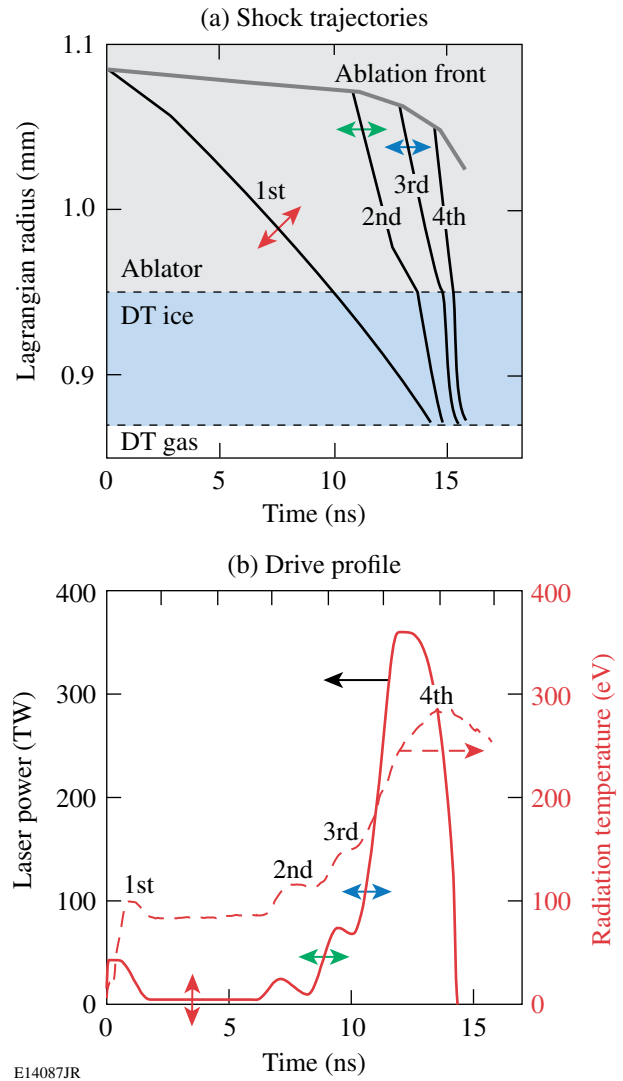


Figure 117.1

(a) Lagrangian trajectories of shocks in an ignition target showing optimal timing with shocks arriving at the inner DT-ice surface in a tight sequence. (b) Temporal history of laser intensity and resulting radiation temperature for an ignition target on the NIF. A shock-timing tuning campaign will iteratively adjust (arrows) the laser pulse shape to optimize shock timing.

The single-shock velocities corresponding to the pressures of the first three steps in the drive pulse (i.e., following coalescence) are approximately 20, 36, and 57 km/s, respectively. (Again, there are several designs and the specified velocities range by ~5% from those values, depending on how the implosion optimization is performed.) For a given design the velocity can have a 2% shot-to-shot variation, but to ensure proper timing, the shock velocities will be measured with a precision of 1% and the coalescence times to less than 30 ps. For the 75- μm -thick DT layer the transit time of the first shock is

~3.75 ns. By integrating the first shock velocity (known to 1%) up to the coalescence time (known to 30 ps), one can determine the coalescence position to a precision of $<2 \mu\text{m}$. The precision of the VISAR diagnostic is more than adequate to determine this position. The error budget for shock-strength and timing experiments is readily met if the velocity is measured to 1% and shock timing is measured to 30 ps.

A DT ignition capsule has a specific drive profile needed to achieve optimal performance. To guide the ignition-tuning campaign, that optimal drive profile is applied (in simulations) to a capsule containing liquid deuterium–deuterium (DD). The resultant shock structure (velocity profiles and timing) in that simulation then serves as the metric to which shock-timing experiments are gauged. The optimal shock strengths (velocities) in liquid DD are obtained from this simulation. Because the shock velocities (but not the shock pressures) are nearly the same in liquid DD as in solid DT, the optimal coalescence position for the shock-timing experiments is very close to that in the solid-DT layer of an ignition capsule. This simulation procedure introduces a surrogacy error that is estimated to be less than 1% in shock velocity.

Experimental Technique

1. VISAR Windows

VISAR has been extensively used to detect and measure laser-driven shock waves in transparent media and has a demonstrated shock-speed precision of 1%–2% and temporal accuracy of $<30 \text{ ps}$ (Refs. 12–14). Shock waves with pressures above $\sim 0.2 \text{ Mb}$ transform liquid deuterium (normally transparent) into a conducting medium;¹¹ as a result, the steep shock front (a conducting surface) readily reflects the VISAR probe beam at a wavelength of 532 nm (and similarly at 590 nm for the NIF VISAR). The arms of a VISAR interferometer have unequal optical paths and produce an output phase that is proportional to the Doppler shift of the reflected probe beam and to the difference in the unequal paths (usually expressed as a time delay). The time delay determines the velocity sensitivity of the interferometer and is adjustable (proportional to the thickness of a glass delay element placed in one arm of the interferometer). For these experiments, the VISAR on OMEGA had a velocity error of $\sim 1.7\%$. The NIF VISAR is designed to achieve 1% velocity measurements.

Cryogenic targets require a closed volume to retain the deuterium gas. In a standard target, the spherical shell is the boundary of that volume. In shock-timing experiments a line of sight is needed for VISAR to probe the shock-velocity profile. Various target configurations were considered, but the stringent

performance tolerances dictated that shock-timing surrogate targets mimic ignition targets with high fidelity. For the NIC tuning experiments, spherical targets will be fitted with a re-entrant cone that extends through the hohlraum wall and is capped by a $20\text{-}\mu\text{m}$ -thick quartz window that confines the DD fuel. This target configuration is shown in Fig. 117.2. Integrated 3-D simulations of this target show that perturbations to the radiation temperature and hohlraum symmetry are minimal.¹⁵ By design, the change in the albedo caused by the portion of the cone traversing the hohlraum–capsule space is offset by that of the sections of ablator surface and hohlraum wall displaced by that cone. It is expected that on the hohlraum wall, where shock timing is measured, the radiation flux will mimic a full ignition target to $\sim 4\%$ (1% in T_{rad}) (Ref. 5).

It has been shown that for direct-drive targets at high intensities the normally transparent material ahead of the shock wave can absorb the VISAR probe laser.¹⁶ This is caused by high-energy x rays produced in the laser-plasma corona.¹⁷ The x rays photoionize the unshocked material, creating free electrons that interact with and absorb the probe light, causing a “blinking” of the probe beam in the material. This could compromise the VISAR data. This is not expected to be a problem in the deuterium (which has a low x-ray-absorption cross section), but the diagnostic window that retains the DD

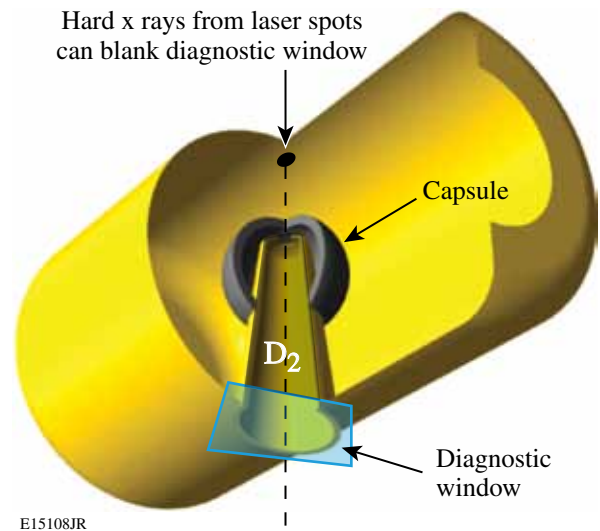


Figure 117.2

NIC shock-timing tuning experiments will use ignition-style targets that have a re-entrant cone in the capsule. The capsule and cone are filled with liquid deuterium. Optical diagnostics probe the inside of the capsule through the window and aperture in the cone.

in the NIF shock-timing targets (Fig. 117.2) can experience this ionization blanking.

Single-sided [one laser entry hole (LEH)] hohlraum experiments with cryogenic and warm targets were used to study this effect and to select a window material. Windows made of silicon nitride, diamond, sapphire, and quartz were tested. Quartz ($20\ \mu\text{m}$ thick) was chosen because of its resistance to blanking (band gap of $\sim 15\ \text{eV}$), optical quality, and ease of fabrication. Though quite resilient, quartz, nevertheless, blanks if exposed to sufficient x-ray flux.

In NIF shock-timing targets, the VISAR window has a line of sight through the ablator material to the hohlraum wall that is directly irradiated by laser beams (Fig. 117.2). Since the ablator absorbs most of the radiation below $\sim 1.5\ \text{keV}$, ionization blanking in these targets results primarily from the Au M-band ($2\ \text{to}\ 4\ \text{keV}$) emission produced by the laser spots. The VISAR cone has a $260\text{-}\mu\text{m}$ hole at the end through which shock timing is measured. The aperture size has been chosen to limit the extent of the hohlraum wall with a “view” of the VISAR window without limiting the area over which a VISAR signal can be collected for NIC-scale capsules. Figure 117.3(a) is a map of beam placement on the interior of a NIF ignition hohlraum. While the capsule is driven by *thermal* radiation from many beams, the VISAR window is irradiated by M-band emission ($h\nu > 2\ \text{keV}$) that originates only from beam spots in the line of sight through the cone aperture. The region on the hohlraum wall that can irradiate the VISAR window is shown as the black dot in Fig. 117.3(a). Two NIF quad beam spots overlap at that point.

A series of experiments were performed on the OMEGA laser using planar targets to investigate the effect of x-ray emission from laser spots on the optical transmission of quartz windows. The configuration is shown in Fig. 117.3(b). A gold foil was placed $1.5\ \text{mm}$ from a Be–Cu–Be sandwich ($75, 0.5,$ and $75\ \mu\text{m}$ thick, respectively) that mimics the opacity of a typical NIC ablator design. An aperture was placed directly behind the ablator and a window was placed $3.5\ \text{mm}$ from the Au foil. VISAR probed the rear surface of the aperture and ablator (through the aperture). Nine OMEGA beams without beam smoothing were focused onto the gold foil to replicate the wall intensity of a NIF target at the relevant incidence angle (60°). The window transmission was observed, and the intensity at which x rays from the laser spots would blank the window was determined. The energy and pulse widths available on OMEGA dictate that the test be done in two steps,

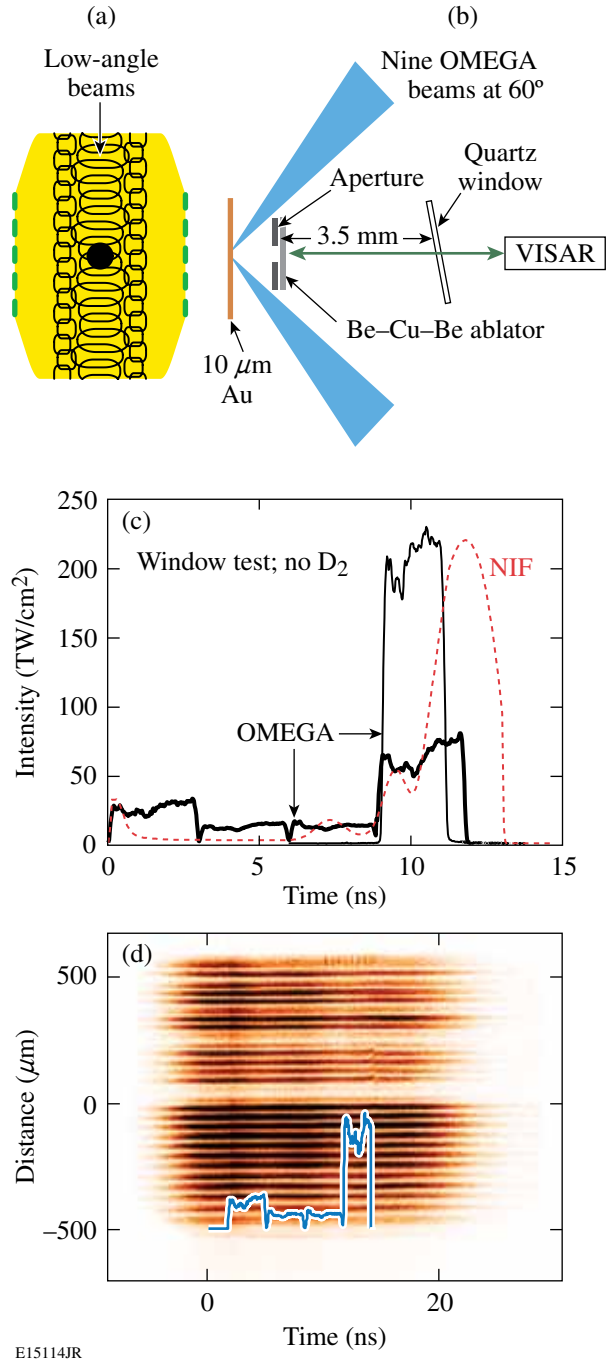


Figure 117.3

(a) The pattern of beam spots in an ignition hohlraum. (b) Target configuration to study effects of M-band emission on windows. (c) NIF laser intensity at the hohlraum equator wall (dashed curve); laser intensity for OMEGA experiments with stacked pulses (solid curves). (d) VISAR data from a stacked-pulse OMEGA experiment showing continuous fringes. The quartz window remains transparent throughout irradiation history, indicating that M-band emission from the laser spot does not “blank” (photoionize) the quartz.

separately measuring peak and integrated fluences associated with ignition-target conditions up to the breakout time of the third shock. Figure 117.3(c) (dashed curve) shows the incident intensity at the NIF hohlraum wall at the VISAR window line of sight [Fig. 117.3(a)]. The intensity profile for the OMEGA experiment with nine beams having temporally square pulses staggered to approximate the NIF wall intensity up to 12 ns is also shown (thick curve). Figure 117.3(d) shows a VISAR record with fringes that have continuous intensity throughout that experiment, indicating that the window remains transparent. Similar results were obtained for nine beams overlapped [thin solid curve in Fig. 117.3(c)] to replicate the intensity at the fourth rise. To investigate the limiting flux for this configuration, a third experiment was performed with a 1-ns pulse at 500 TW cm^2 . At this fluence the quartz window blanked, but this is $2.5\times$ higher than required for the NIF.

These results indicate that the quartz windows remained transparent when exposed to both the instantaneous flux and the integrated flux (up to the third shock) required for shock timing. These tests are conservative in that the NIF beams have high angles of incidence and will traverse considerable plasma en route to the hohlraum wall, reducing the actual intensity at the wall. Also, the Au foil was 1.5 mm from the aperture and 3.5 mm from the window; in the NIF targets those distances will be $\approx 2 \text{ mm}$ and $\approx 8 \text{ mm}$, respectively.

2. Hohlraum Experiments

The radiation environment in a laser-driven hohlraum is different than that of an open-geometry planar-target laser plasma: the laser beams overlap and are tightly focused at the LEH and the plasma scale lengths are changed by the closed geometry. VISAR measurements were performed with hohlraum targets to investigate if they could cause window blanking or other deleterious effects.

For these tests, NIF-sized Au re-entrant cones were inserted into OMEGA-scale hohlraums (2.55 mm long, 1.6 mm in diameter with 1.2-mm laser entrance holes). The cones were 5 mm long and had an 11° opening angle (to accommodate the $f/3$ VISAR focal cone). The NIF tip has a $10\text{-}\mu\text{m}$ wall formed into a spherical shape that will be ultimately placed within $\sim 200 \mu\text{m}$ of the spherical-ablator inside surface. That tip has a $260\text{-}\mu\text{m}$ -diam aperture through which shocks are viewed. Inside the shell the cone wall is $50 \mu\text{m}$ thick and the rest of the cone is $100\text{-}\mu\text{m}$ -thick Au. The hohlraums were empty: no gas fill, no LEH windows. Figure 117.4(a) shows three views of these targets.

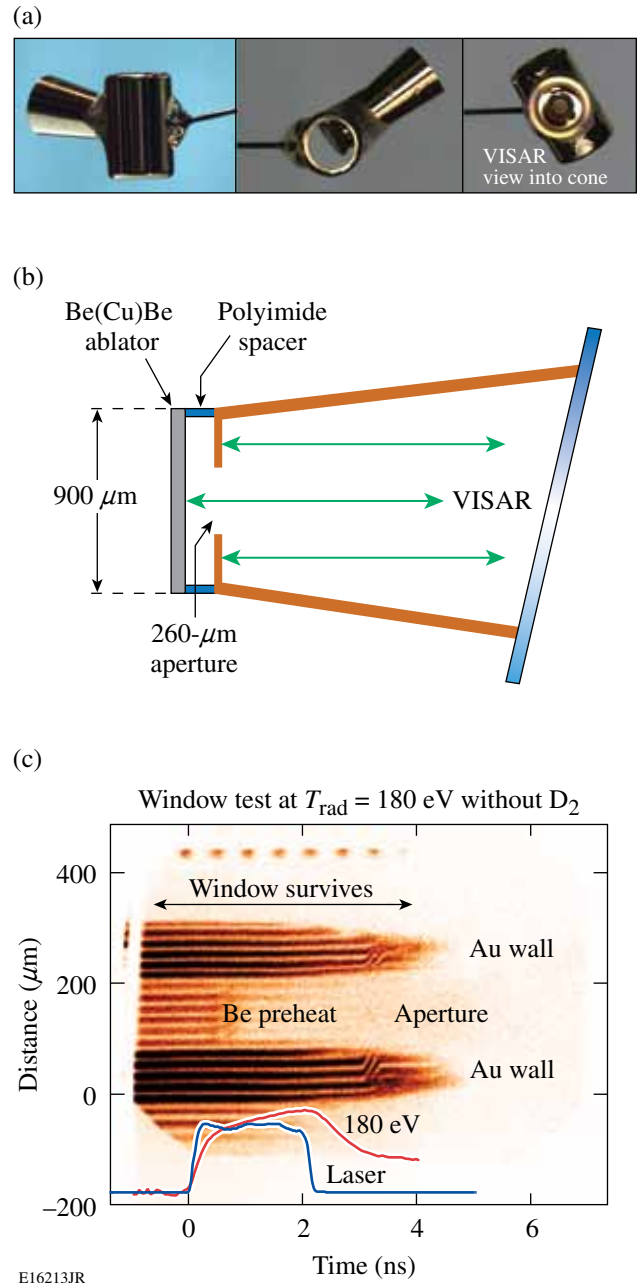


Figure 117.4

(a) The OMEGA targets have NIF-sized diagnostic cones inserted into the OMEGA scale-1 hohlraums. (b) The ablator and cone tip assembly for the OMEGA shock-timing tests in hohlraum targets. The Be–Cu sandwich replicates the opacity of a NIF ablator. (c) VISAR data for a warm, empty hohlraum heated to 180 eV. The probe beam reflects off the cone face and the ablator (through cone aperture). These data show the Be ablator unloading because of preheat and window transparency persisting throughout the experiment, thereby proving viability of this technique.

The OMEGA experiments used planar ablaters, so those cones had a 10- μm -thick, 260- μm -aperture planar tip. The rest of the cone was identical to the NIF cone design. The ablaters were sandwiches of Be and Cu to simulate the x-ray opacity of the Cu-doped Be ablaters² for the NIF. They were comprised of two 75- μm Be foils with a 0.5- μm Cu foil in between and were “brazed” to form a glueless bond. The ablaters were mounted 190 μm from the cone tip to replicate the shell-to-cone-tip distance in the NIF targets.

One concern was that M-band x rays entering the aperture at high angles could heat the inner cone wall sufficiently to create a secondary hohlraum that would re-radiate and blank the window. To mimic the spherical-capsule geometry, which allows these high-angle rays to enter the aperture, the ring that held the planar ablator away from the cone tip was made of 60- μm polyimide. This ring has similar opacity to the Be–Cu ablator. The ablator and cone geometry are shown in Fig. 117.4(b).

The VISAR diagnostic is not perpendicular to any convenient and symmetric hohlraum axes in the OMEGA chamber. Rather than perturb the irradiation pattern and line of sight for radiation-temperature measurements (Dante), the VISAR cones were inserted 79.2° from the hohlraum axis to accommodate this offset [Fig. 117.5(a)]. This deviation from the NIF geometry is considered conservative since, at this angle, the cone views the region irradiated by beams with lower angles of incidence and are, therefore, of higher intensity than those at the equator. The cones were inserted so the ablaters were on the central axis of the hohlraum. The ablaters were ~ 0.8 mm from the hohlraum wall, less than half the distance of the NIF targets to the hohlraum wall.

The hohlraums were irradiated by 38 OMEGA beams with no beam smoothing and having 2-ns-long, temporally square pulses to produce radiation temperatures of >180 eV. VISAR measurements of the rear side of the ablator (i.e., made through the window and cone aperture) are shown in Fig. 117.4(c). The VISAR data comprise a series of interferometer fringes^{13,16} whose vertical position is proportional to the velocity of the reflecting surface (shock wave or ablator surface). Figure 117.4(c) shows two regions of the target probed by the VISAR: the inner surface of the aperture, and the rear surface of the ablator, viewed through the aperture. Prior to the drive pulse and subsequent thermal radiation (graphs shown in plot), the fringes are horizontal and of constant intensity. As the drive temperature rises, the ablator is heated and, at ~ 1 ns, the expanded rear-surface material absorbs the VISAR probe beam, causing the signal to diminish. It is important to

note that the signal from the Au aperture surface (above and below the ablator signal) that is well shielded and, therefore, not preheated and does not expand, persists throughout the drive pulse. This indicates that the window remains transparent and survives the radiation from the hohlraum.

Experiments with hohlraums driven to $T_{\text{rad}} > 200$ eV produced blanking in the quartz window. This is consistent with the open experiments described in **VISAR Windows** (p. 3) and

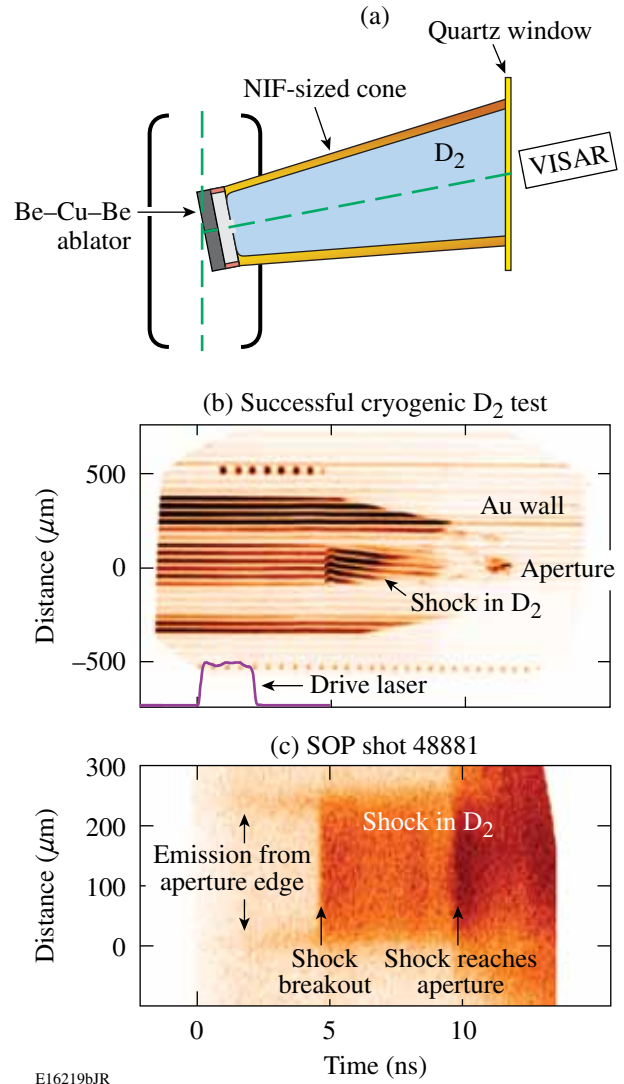


Figure 117.5

(a) The cryogenic target is identical to that in Fig. 117.4(a), except that the cone is filled with liquid deuterium and the assembly is mounted on a cryostat. (b) VISAR data show again that the window remains transparent and that the shock in deuterium is observed. (c) Streaked optical pyrometer (SOP) data showing temporal features (in self-emitted light) that confirm the behavior in the VISAR data (b).

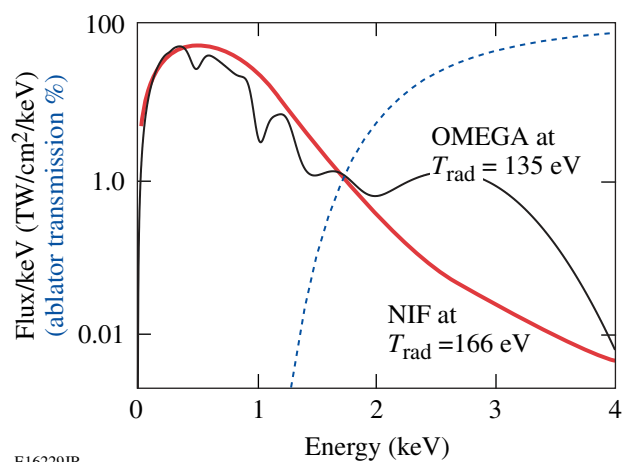
ultimately limit the conditions under which windows can be used. In the **Fourth Shock Timing** section below a windowless target is proposed for timing the fourth “shock.”

During these experiments it was found that scattered light from the incident drive beams could blank the VISAR window from the outside. To prevent this, the diagnostic cones were fitted with shields to block all scattered light from irradiating the window. This is an important aspect of the NIF target design because a significant amount of unconverted light passes within a 3- to 10-mm annulus around NIF targets. As a further precaution, some cones were coated on the inside with CH to minimize any secondary-hohlraum effect by reabsorbing any low-energy photons re-emitted by the cone wall upon irradiation by M-band emission. As expected, these experiments also showed no window blanking and CH overcoats are not expected to be required at the NIF.

3. Cryogenic Experiments

Experiments were performed using cryogenic targets filled with liquid deuterium. The hohlraums were empty while the cones were filled with liquid deuterium between the ablator and the VISAR window [Fig. 117.5(a)]. Figure 117.5(b) shows the VISAR data from such an experiment driven at 135 eV. These data clearly show that the window survives throughout the drive pulse and the shock in the deuterium is observed. The self-emission data [Fig. 117.5(c)] from the streaked optical pyrometer (SOP)¹⁸ exhibit identical temporal features that confirm the timing of the shock breakout (arrival at rear surface) and arrival time at the aperture after transiting the ablator–cone gap. Additionally, the heating of the aperture edge, as evidenced by its self-emission, is seen early in time. While this heating is unavoidable, it is not expected to present a problem with the measurements or their precision.

These data at 135 eV confirm that the proposed shock-timing technique is viable for the NIF targets driven by higher radiation temperatures because the OMEGA experiments produce more M band than is expected on the NIF. Figure 117.6 shows the predicted M-band flux from the NIF experiments at 165 eV, compared to the OMEGA emission from the 135-eV hohlraums. Note that the OMEGA hohlraums produce significantly more x-ray flux above 2 keV than expected from the NIF targets. This is because the OMEGA hohlraums have a smaller fraction of wall irradiated by beams and have lower time-dependent albedo and, therefore, require a higher beam intensity to reach a given radiation temperature. This higher intensity leads to more M band, which is produced primarily in the laser-spot regions.



E16229JR

Figure 117.6

Radiation spectrum expected on the NIF (thick solid curve) for conditions of the third shock (165 eV) and that for the OMEGA experiments at 135 eV (thin solid curve). Note that above 2 keV, the OMEGA experiments have higher fluxes. The ablator transmits (dashed curve) this region of the spectrum.

4. Fourth Shock Timing

The tuning experiments for NIF shock timing must also time the compression wave (or fourth shock) that is driven by radiation temperatures above 250 eV. The fluxes from these drives are expected to blank the VISAR window; therefore, a windowless target was designed. These targets have a re-entrant cone with no aperture, confining the deuterium only to the capsule. The compression wave will be detected by the arrival of the shock at the inner surface of the cone tip. This will be detected as either movement or cessation of the fringes. If the released material remains solid when the shock arrives at a solid/vacuum interface, this material can continue to reflect the VISAR probe beam and the free surface velocity can be detected. If, however, the material is sufficiently heated to melt and then expand, it typically produces a density gradient that absorbs the probe beam at the rear surface and the signal then vanishes.

This concept was tested on OMEGA with the hohlraum driven to much higher temperatures. Figure 117.7(a) shows the target design that comprised a standard NIF cone and [in Fig. 117.7(b)] the Be–Cu–Be ablator sandwich. The cone tip had an Au step assembly (16 μm and 36 μm thick) facing the ablator. VISAR and SOP probed the rear surface of that assembly. In these experiments, for simplicity, there was no deuterium in the gap between the ablator and the Au step. The gap was filled with 1 atm of air during fabrication and well sealed. There was no need for a VISAR window, so none was used at the end of the cone. The VISAR data [Fig. 117.7(c)] show continuous

fringes until the arrival (at 3.5 and 4 ns) of shocks at the rear of the two steps.

The radiation temperature in this experiment was 220 eV, and as was the case seen in Fig. 117.6, the M-band emission was significantly (12 \times) higher than that expected for a 250-eV NIF hohlraum. As a result, the shock that first breaks out of the two steps was driven by the M-band emission incident on the cone face. The subsequent arrival of the shock driven by the thermal spectra is seen as a brief increase of intensity that occurs at the thin step [upper portion in Fig. 117.7(c)] at \sim 5.7 ns. These features are confirmed by 1-D simulations using the experimental drive including the M-band emission. Simulations

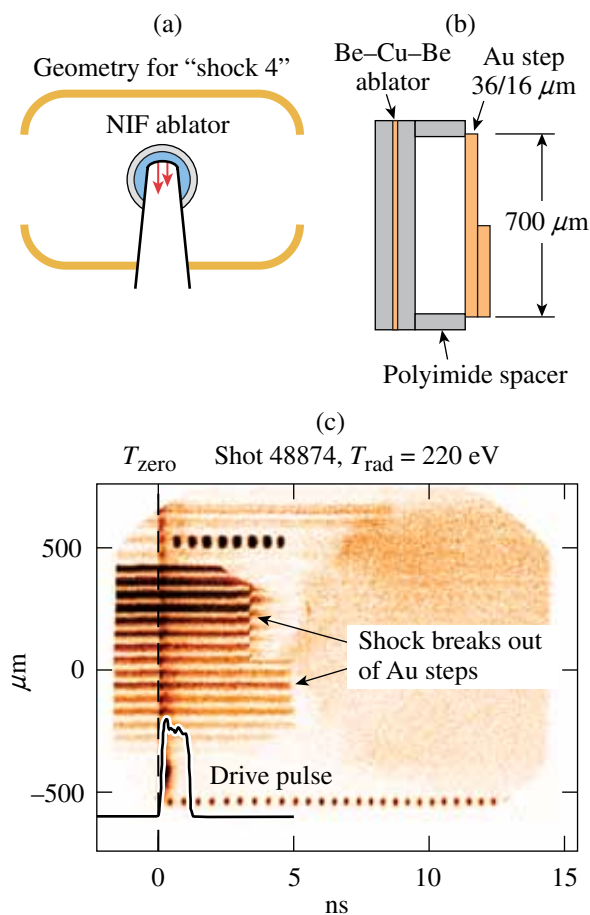


Figure 117.7

(a) The NIF target configuration used to measure the timing of the compression wave. It is similar to the design in Fig. 117.2, except there is no aperture in the cone and no diagnostic window. (b) The OMEGA cone-tip design used to test the compression-wave timing technique. (c) VISAR results for a target driven to 220 eV, showing persistence of VISAR fringes until shock breakout. This breakout provides an unambiguous arrival time for the shock at the rear surface of the steps.

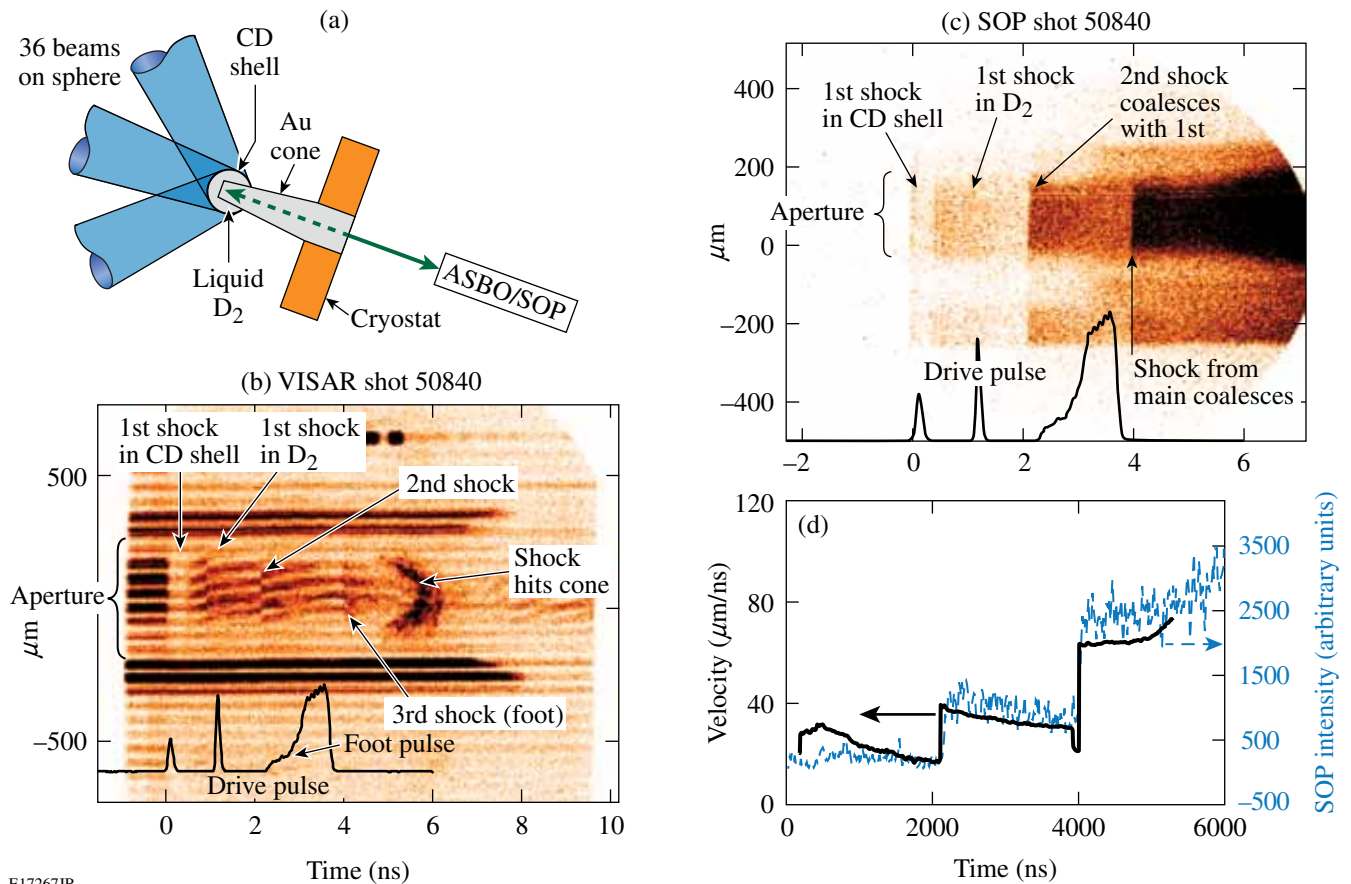
of NIF targets predict that the thermal shock breaks out well before any M-band-driven shocks.

The unambiguous breakout feature is the cessation of the fringes caused by the release of material absorbing the VISAR laser. This is a common observation in shock experiments using opaque samples. This technique is applicable to shock experiments over a wide range of shock pressures. At lower pressures, the breakout may not cause a cessation of fringes but, instead, the onset of motion. At very high drive intensities, the sample could be preheated, causing the rear-surface release. In this latter case, the VISAR signal could be lost, but experiments show that the arrival of the shock can still be observed [as in Fig. 117.7(c)] because it steepens the density gradient, producing a brief reflected VISAR signal and an unambiguous SOP signal. [The steepening occurs in times less than the resolution time of the VISAR (30 ps) and lasts a few hundred picoseconds, depending on the time it takes for that material to relax and once again form an absorbing profile.] This provides confidence that this technique can be used for a wide range of conditions on the NIF. It is expected that the shock-propagation time across the cone tip can be accounted for with precision sufficient to achieve the necessary shock timing on the NIF.

5. Spherically Convergent Shock Experiments

Previous experiments used planar ablaters and single drive pulses for expediency. The NIF experiments will involve multiple, spherically converging shocks—conditions not attainable in OMEGA hohlraum experiments without resorting to quarter-scale spherical targets with insufficient reflecting surface area. To study these effects, larger-scale, direct-drive experiments were performed on cryogenic spherical targets. These targets were 900- μm -diam, 10- μm -thick CD shells fitted with the NIF-scale VISAR cones. The assemblies were filled with liquid deuterium and irradiated by 36 OMEGA beams in the hemisphere centered on the VISAR line of sight [Fig. 117.8(a)]. This produces spherical shocks that converge toward the cone aperture. Figure 117.8(b) shows the VISAR record for an experiment driven by the multiple laser pulses shown at the base of this figure.

These targets have a 1000- \AA Al coating on their outer surface. Before time zero, the VISAR probe beam reflects off the inner surface of this layer. At time zero, the laser ablates the layer and the x rays from the laser plasma cause the CD shell to blank (absorb) the VISAR probe beam, causing the VISAR fringes to disappear. At about 0.5 ns, the shock emerges from the CD shell and enters the deuterium. The VISAR fringes return because the shocked deuterium is reflective (>50%) and



E17267JR

Figure 117.8

(a) Direct-drive cryogenic spherical targets used to study the timing of multiple convergent shocks on OMEGA. (b) VISAR record for three shocks in deuterium produced by the multiple pulses shown at the base of the figure. Evidence of shock coalescence (stronger shocks overtaking weaker ones) are evident at 2 and 4 ns; these indicate that multiple convergent shocks can be timed with this target and diagnostic configuration. (c) The SOP data show that the coalescence features observed in VISAR data are replicated in the self-emission intensity. (d) Shock velocities inferred from VISAR data and self-emission intensity histories for the data shown in (b) and (c).

the unshocked deuterium in front of it remains transparent. The curvature in the fringes from 0.5 to 2 ns results from deceleration of this first shock, which decays because it is unsupported: the first drive pulse has turned off. Just after 2 ns the shock produced by the second drive pulse (at 1.2 ns) overtakes the first shock. This is observed as a jump in fringe position produced by the jump to the new shock velocity. Since the first shock produces conduction electrons in the deuterium, the shocked material is reflective and opaque to the VISAR probe. As a result, VISAR cannot detect the second shock “through” the first shock, until the second overtakes the first shock.

At about 2.25 ns the “main” drive pulse begins at low intensity and ramps to higher intensity. At 4 ns, the shock from this pulse overtakes the combined first and second shocks, producing another jump in fringe position. About 1 ns later the

shock hits the front surface of the Au cone. The bright feature that begins at ~ 5 ns is either reflection off of or self-emission from the hot material from the aperture that was heated by the shock. This material flows into the aperture, producing the converging feature from 5 to 6 ns. Ultimately the material cools, the shock passes it, and the decaying shock can again be observed at late times. It should be noted that in the NIF tuning campaign the pertinent shock-timing events are over before the shock reaches the cone face.

The self-emission from the shock was acquired simultaneously with VISAR data. Figure 117.8(c) depicts the intensity of light (590 to 850 nm) emitted by the shock and detected by the SOP. The features of the three shocks described above are plainly visible in Fig. 117.8(c). The material closing into the aperture is not observed (as in the VISAR data), but the arrival

of the shock at the aperture can be seen as a spatial broadening of the emission region. The slope of this growing edge can be traced back to the original diameter, intersecting at ~ 5 ns, which is the arrival time observed by VISAR. Figure 117.8(d) shows the shock velocity (deduced from VISAR) and the self-emission intensity histories measured for this shot. Note that these measured velocities span the range of shock velocities (20 to 57 km/s) that are prescribed for the first three shocks in a NIF ignition target, demonstrating this technique at applicable shock conditions.

These data confirm that VISAR and SOP can readily detect the velocities and the timing of spherically converging shocks that have traveled (and converged) by the ~ 200 - μm distance from the shell to the cone tip. The lateral extent of the VISAR data is governed by the amount of probe light that is returned into the collection lens of the diagnostic and is proportional to the curvature of the spherical shell. The NIF capsules will be about twice the size of those used for the OMEGA experiments, so the detected region will be twice that of the OMEGA experiments while the radial distance traveled is the same. The OMEGA conditions are therefore more stringent (i.e., smaller curvatures) than the NIF experiments.

Conclusions

The National Ignition Campaign requires that multiple spherically convergent shock waves be timed to high precision. Targets with re-entrant cones will make it possible for optical diagnostics to probe the interior of the capsules *in situ*, with minimal interference to the x-ray-flux environment driving the probed capsule region. These targets also make possible the precise optical measurements of the velocity profiles (and therefore timing) of multiple shocks in the harsh radiation environment of an ignition hohlraum; this presents formidable challenges.

Experiments were performed on the OMEGA laser to assess the viability of the proposed techniques. These experiments used open and hohlraum geometries to select quartz as the material for the diagnostic window in the NIF targets. Hohlraum experiments showed that quartz remains transparent throughout experiments that were driven to radiation temperatures greater than 180 eV, and that produced M-band emission greater than that expected on ignition targets, up to the timing of the third shock. Cryogenic experiments confirmed that the column of liquid deuterium is not adversely affected by thermal and M-band x rays from the hohlraum. Direct-drive experiments on cryogenic spherical targets demonstrated that shock timing can be performed on multiple, spherically

convergent shocks, and that shocks up to ~ 70 km/s can be detected optically.

Each of the OMEGA experiments had more adverse conditions than those expected on the NIF, i.e., higher M-band emission, less standoff distance to the window, and smaller radius of curvature. These experiments, therefore, provide high confidence that the NIC plan for shock timing is viable and will successfully time shocks to adequate precision for ignition targets.

ACKNOWLEDGMENT

This work was supported by the U.S. Department of Energy Office of Inertial Confinement Fusion under Cooperative Agreement No. DE-FC52-08NA28302 (LLE), DE-AC52-07NA27344 (Lawrence Livermore National Laboratory), the University of Rochester, and the New York State Energy Research and Development Authority. Sandia is a multiprogram laboratory operated by Sandia Corporation, a Lockheed Martin Company, for the United States Department of Energy's National Nuclear Security Administration under contract DE-AC04-94AL85000. The support of DOE does not constitute an endorsement by DOE of the views expressed in this article.

REFERENCES

1. J. D. Lindl, *Inertial Confinement Fusion: The Quest for Ignition and Energy Gain Using Indirect Drive* (Springer-Verlag, New York, 1998), Chap. 6, pp. 61–82.
2. T. R. Dittrich *et al.*, *Phys. Plasmas* **6**, 2164 (1999).
3. B. A. Hammel *et al.*, *Plasma Phys. Control. Fusion* **48**, B497 (2006).
4. D. H. Munro *et al.*, *Phys. Plasmas* **8**, 2245 (2001).
5. D. H. Munro, H. F. Robey, B. K. Spears, and T. R. Boehly, *Bull. Am. Phys. Soc.* **51**, 105 (2006).
6. T. R. Boehly, D. L. Brown, R. S. Craxton, R. L. Keck, J. P. Knauer, J. H. Kelly, T. J. Kessler, S. A. Kumpan, S. J. Loucks, S. A. Letzring, F. J. Marshall, R. L. McCrory, S. F. B. Morse, W. Seka, J. M. Soures, and C. P. Verdon, *Opt. Commun.* **133**, 495 (1997).
7. S. W. Haan *et al.*, *Eur. Phys. J. D* **44**, 249 (2007).
8. S. W. Haan *et al.*, *Phys. Plasmas* **12**, 056316 (2005).
9. D. G. Hicks, T. R. Boehly, P. M. Celliers, J. H. Eggert, S. J. Moon, D. D. Meyerhofer, and G. W. Collins, *Phys. Rev. B* **79**, 014112 (2009).
10. P. M. Celliers *et al.*, *Phys. Rev. Lett.* **84**, 5564 (2000).
11. L. M. Barker and R. E. Hollenbach, *J. Appl. Phys.* **43**, 4669 (1972).
12. P. M. Celliers *et al.*, *Appl. Phys. Lett.* **73**, 1320 (1998).
13. P. M. Celliers, D. K. Bradley, G. W. Collins, D. G. Hicks, T. R. Boehly, and W. J. Armstrong, *Rev. Sci. Instrum.* **75**, 4916 (2004).

14. T. R. Boehly, T. J. B. Collins, O. Gotchev, T. J. Kessler, J. P. Knauer, T. C. Sangster, and D. D. Meyerhofer, *J. Appl. Phys.* **92**, 1212 (2002).
15. H. F. Robey, D. H. Munro, B. K. Spears, M. M. Marinak, O. S. Jones, M. V. Patel, S. W. Haan, J. D. Salmonson, O. L. Landen, T. R. Boehly, and A. Nikroo, *J. Phys., Conf. Ser.* **112**, 022078 (2008).
16. T. R. Boehly, E. Vianello, J. E. Miller, R. S. Craxton, T. J. B. Collins, V. N. Goncharov, I. V. Igumenshchev, D. D. Meyerhofer, D. G. Hicks, P. M. Celliers, and G. W. Collins, *Phys. Plasmas* **13**, 056303 (2006).
17. W. Theobald, J. E. Miller, T. R. Boehly, E. Vianello, D. D. Meyerhofer, T. C. Sangster, J. Eggert, and P. M. Celliers, *Phys. Plasmas* **13**, 122702 (2006).
18. J. E. Miller, T. R. Boehly, A. Melchior, D. D. Meyerhofer, P. M. Celliers, J. H. Eggert, D. G. Hicks, C. M. Sorce, J. A. Oertel, and P. M. Emmel, *Rev. Sci. Instrum.* **78**, 034903 (2007).

Cryogenic Target Performance and Implosion Physics Studies on OMEGA

Introduction

The goal of inertial confinement fusion (ICF)^{1,2} is to implode a spherical target to achieve high compression of the fuel and high temperature of the hot spot to trigger ignition and maximize the thermonuclear energy gain. Both direct- and indirect-drive concepts of ICF rely on targets with thick, cryogenic deuterium–tritium (DT) shells for ignition.^{1–3} While target designs vary in their details, these concepts have common basic physics such as ablator and fuel compressibility, energy coupling and transport, hydrodynamic instabilities, shock tuning, and preheating. Recent OMEGA cryogenic D₂ experiments demonstrated ignition-relevant fuel compression with a neutron-averaged areal density of ~ 200 mg/cm² (Refs. 4 and 5). This corresponds to an estimated peak fuel density of ~ 100 g/cm³, $\sim 500\times$ higher than initial cryogenic ice density. These experiments were conducted at peak drive intensities of $\sim 5 \times 10^{14}$ W/cm² using 10- μ m-thick plastic ablators with an implosion velocity of $\sim 2.4 \times 10^7$ cm/s (Refs. 4 and 5). To achieve an ignition-relevant implosion velocity of $\sim 4 \times 10^7$ cm/s, the peak drive intensity must be increased to $\sim 10^{15}$ W/cm² (Refs. 3 and 4). Recent direct-drive ICF research on OMEGA focused on understanding the physics of this high-intensity regime. Understanding the dynamics of target implosion is essential to all ignition target designs, whether directly or indirectly driven. This article reviews the results obtained over this past year in the physics of cryogenic target implosions, including energy coupling and transport, hydrodynamic instabilities, compressibility, shock timing, and preheating.

The following sections (1) show the importance of non-local electrons in modeling laser coupling and energy transport; (2) present recent results from experiments that show stabilization of hydrodynamic instabilities at peak intensities of $\sim 10^{15}$ W/cm²; and (3) describe compressibility experiments performed in plastic ablators, shock-timing experiments, compression results from cryogenic D₂ spherical implosions, and spherical experiments in Si-doped plastic ablators. The final section summarizes these results.

Energy Coupling and Transport

Acceleration experiments with planar plastic foils were conducted to study energy coupling and transport in plastic ablators.⁶ In these experiments, 2.5-mm-diam, 20- μ m-thick CH targets were driven with a 1-ns square pulse shape at a peak laser intensity of $\sim 10^{15}$ W/cm². The targets were driven with 12 overlapped beams using all standard OMEGA beam-smoothing techniques, including distributed phase plates (DPP's),⁷ polarization smoothing (PS),⁸ and smoothing by spectral dispersion (SSD).⁹ The target acceleration was measured using side-on radiography with a streak camera using ~ 2 -keV x rays from a dysprosium sidelighter and compared with two-dimensional (2-D) *DRACO* simulations.⁶ The simulations used a local model for electron transport¹⁰ with a time-dependent flux limiter derived from a one-dimensional (1-D) nonlocal thermal-electron-transport model.¹¹ The nonlocal model solves the Boltzman equation with the Krook's collision operator and an appropriate electron-deposition length. It gives an effective time-dependent flux limiter, defined as the ratio of nonlocal heat flux to the free-stream heat flux.¹¹

The measured target trajectory [Fig. 117.9(a)] is in good agreement with the simulated trajectory using the effective time-dependent flux limiter shown in Fig. 117.9(b). Reference 6 shows that the measured target trajectories are in good agreement with nonlocal model predictions over the broad range of intensities from $\sim 2 \times 10^{14}$ to 1×10^{15} W/cm². Predictions using a local model of thermal transport with a constant flux limiter of $f = 0.06$ (Ref. 10) (previous standard model for OMEGA experiments) are in good agreement with experiments at intensities below $\sim 5 \times 10^{14}$ W/cm², but break down at peak intensities $\sim 10^{15}$ W/cm², as shown in Fig. 117.9(a). These results indicate that nonlocal effects are critical for modeling energy coupling and transport in direct-drive-ignition designs using high-intensity UV lasers. Experiments using green and IR lasers have shown that nonlocal effects were important even at much lower intensities of $\sim 1 \times 10^{14}$ W/cm² (Refs. 12 and 13).

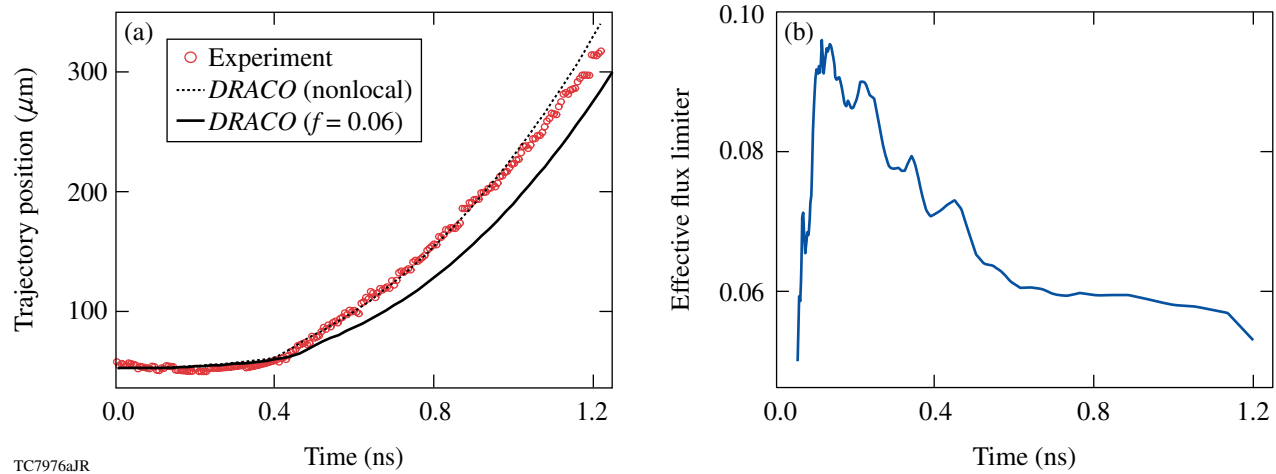


Figure 117.9

(a) Measured (circles) and simulated target trajectories using a flux limiter of $f = 0.06$ (solid line) and an effective flux limiter derived from the nonlocal model (dotted line), shown in (b).

Hydrodynamic Instability Experiments

The nonlocal model for electron thermal transport predicts target decompression at the ablation front¹¹ relative to prediction of the local model.¹⁰ The decompression at the ablation front is caused by heating from the high-energy tail of the electron distribution. The decompression at the ablation surface reduces the growth rate of Rayleigh–Taylor (RT) instability.^{12–15} In the linear stage of RT instability, the growth rate as a function of modulation wave number k in plastic targets is given by the dispersion relation¹⁶

$$\gamma(k) = 0.94 \left[kg / (1 + kL_n) \right]^{0.5} - 1.5 kV_a, \quad (1)$$

where g is the target acceleration, V_a is the ablation velocity, and L_n is the density scale length. The growth rate is proportional to the first acceleration term and is reduced by the second stabilizing term $-1.5 kV_a$, caused by material ablation. When the target is decompressed, the ablation velocity increases, resulting in a reduced RT growth rate. This reduction is stronger for modulations with high wave numbers (shorter wavelengths). This was experimentally observed in 20- μm -thick, planar CH targets driven with various square drive pulses.^{14,15}

In this work, 20- μm -thick CH targets were driven with 12 overlapped beams with full beam smoothing including DPP's,⁷ PS,⁸ and SSD.⁹ The RT growth of preimposed 2-D modulations was measured with through-foil, x-ray radiography^{14,15} using ~ 1.3 -keV x rays from a uranium backlighter.

In the RT experiments, the 2-D preimposed modulations had wavelengths of 20, 30, and 60 μm , with initial amplitudes of 0.05, 0.05, and 0.125 μm , respectively. Results of RT growth experiments are shown in Fig. 117.10 for a 1-ns drive at an intensity of $\sim 1 \times 10^{15}$ W/cm² [Figs. 117.10(a)–117.10(c)] and a 1.6-ns drive at an intensity of $\sim 5 \times 10^{14}$ W/cm² [Figs. 117.10(d)–117.10(f)]. The experimental data at a 60- μm wavelength are weakly affected by the stabilizing term $-1.5 kV_a$ [Figs. 117.10(a) and 117.10(d)]. This modulation grows more rapidly at a drive intensity of $\sim 10^{15}$ W/cm² than at $\sim 5 \times 10^{14}$ W/cm². This indicates that the acceleration is higher at high intensity, as expected. At an intensity of $\sim 5 \times 10^{14}$ W/cm² the short-wavelength modulations (at wavelengths of 20 μm and 30 μm) grow faster than the long, 60- μm -wavelength modulation. At a high intensity of 1×10^{15} W/cm², this trend is reversed: the 60- μm -wavelength modulation grows faster than the 30- μm perturbation, with the 20- μm -wavelength perturbation completely stabilized.

This stabilization is consistent with the increased ablation velocity and density scale length at high intensity predicted by the nonlocal electron transport model.^{11,14} The stabilization is also correlated with the hot-electron signal from two-plasmon-decay (TPD) instability.^{14,17,18} This signal becomes detectable at intensities above $\sim 5 \times 10^{14}$ W/cm², similar to previous experiments.^{4,19} The relationship between the x-ray emission and the target preheat is still under investigation. The strong measured RT growth stabilization reduces the requirements for mitigation of the hydro-instability growth in direct-drive-ignition capsules

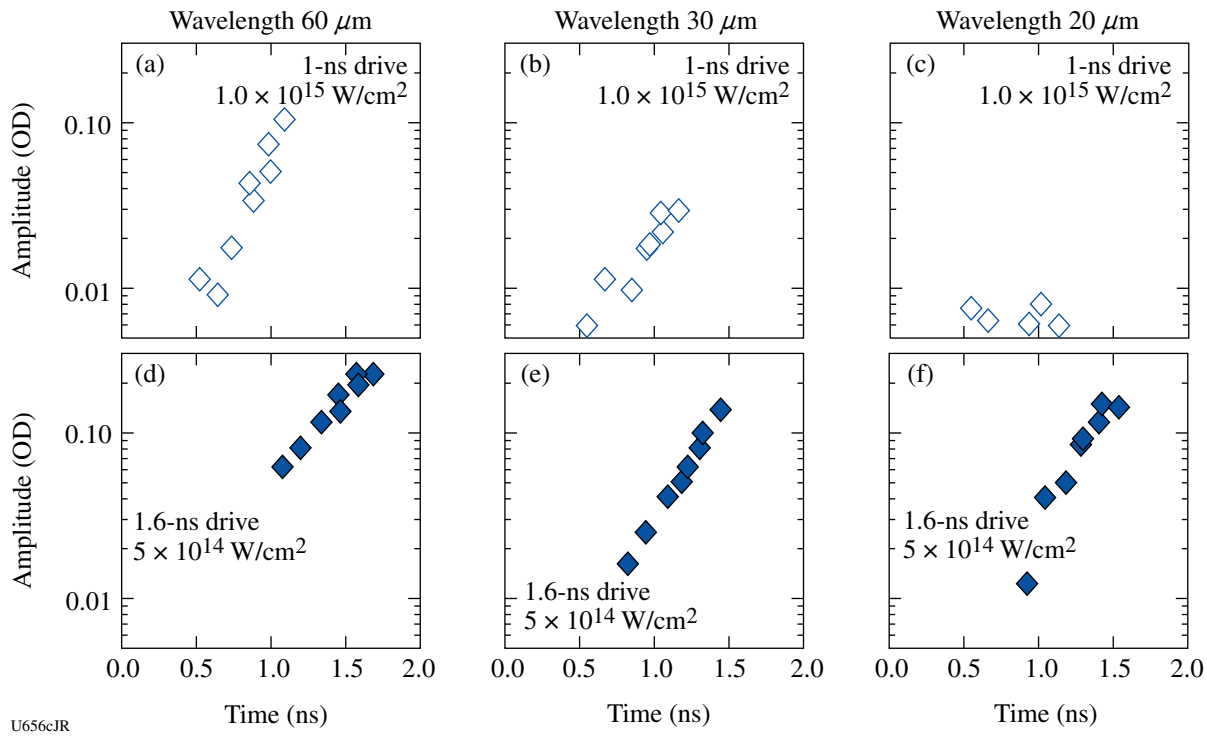


Figure 117.10

Optical-depth modulations versus time for a 1-ns square laser drive at an intensity of $\sim 1 \times 10^{15} \text{ W/cm}^2$ [(a), (b), and (c)], and with a 1.6-ns square laser drive at an intensity of $\sim 5 \times 10^{14} \text{ W/cm}^2$ [(d), (e), and (f)] with wavelengths of $60 \mu\text{m}$, $30 \mu\text{m}$, and $20 \mu\text{m}$, respectively.

at the National Ignition Facility (NIF).¹⁴ Future experiments will distinguish between nonlocal and hot-electron contributions to the ablation-surface preheating.

Plastic-Ablator Compressibility

Figure 117.11 shows a schematic of the plastic-ablator compressibility experiments²⁰ performed with $\sim 125\text{-}\mu\text{m}$ -thick, $\sim 280\text{-}\mu\text{m}$ -wide plastic planar targets driven with a high-compression, 3-ns-long shaped pulse at a peak drive intensity of $\sim 1 \times 10^{15} \text{ W/cm}^2$, as shown in Fig. 117.12(a). The targets were driven with 14 overlapped beams with full beam smoothing, including DPP's,⁷ PS,⁸ and SSD.⁹ The target compression was measured with x-ray, side-on radiography using an $\sim 6.4\text{-keV}$ iron sidelight. The 2-ns-long foot of the pulse sends a shock wave that compresses the ablator by $\sim 3\times$. The compression increases up to $\sim 9\times$ when the main shaped pulse sends a compression wave through the target. Figures 117.12(b) and 117.12(c) compare the measured and simulated optical-depth compression of the target. The shock and compression waves travel from right to left in these data. The predictions for (b) 2.3 ns and (c) 2.9 ns show good agreement with the experiment, confirming the compression of the plastic ablator by a shaped laser drive. These measurements validated

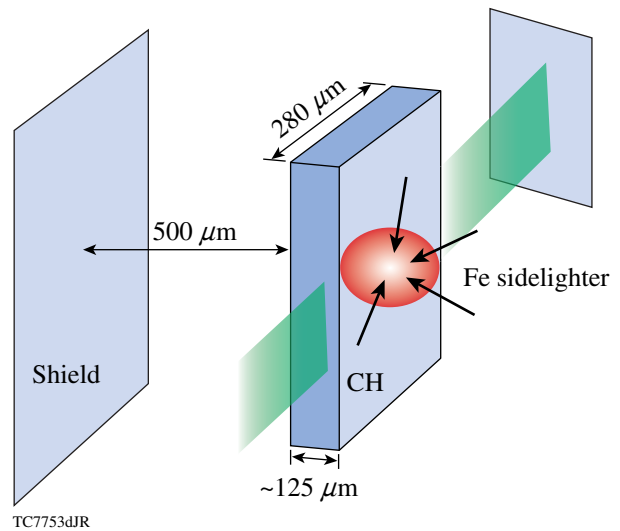


Figure 117.11

Experimental setup for plastic-ablator compressibility experiments performed with $\sim 125\text{-}\mu\text{m}$ -thick, $\sim 280\text{-}\mu\text{m}$ -wide plastic planar targets driven with 14 overlapped beams. The target compression was measured with x-ray, side-on radiography using an $\sim 6.4\text{-keV}$ iron sidelight.

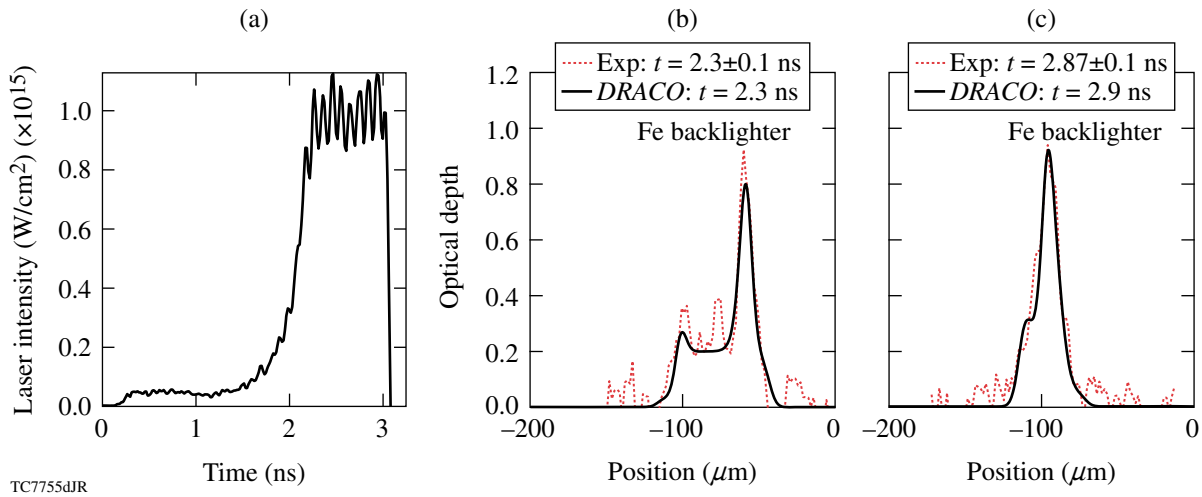


Figure 117.12

(a) High-compression, 3-ns-long laser pulse shape. The measured (dotted line) and simulated (solid line) optical-depth target compression at (b) 2.3 ns and (c) 2.9 ns. The shock and compression waves travel from right to left. The predictions show good agreement with measurements.

the hydrodynamics and equation of state (*SESAME*) of the shock and compression waves predicted by the 2-D hydrocode *DRACO*,²⁰ used to simulate the experiments. Similar experiments conducted at lower intensities of $\sim 5 \times 10^{14} \text{ W/cm}^2$ also showed agreement with hydro simulations, while experiments at an intensity of $\sim 1.5 \times 10^{15} \text{ W/cm}^2$ (higher than required for ignition on the NIF) showed target decompression that was correlated with the presence of hot electrons generated by TPD instability.²⁰

Shock Timing

Figure 117.13 shows a schematic of the shock-timing experiments performed with spherical $10\text{-}\mu\text{m}$ -thick CD shells filled with cryogenic D_2 liquid.²¹ The target cone makes it possible for the active shock breakout (*ASBO*)²² system to probe the shock waves in liquid deuterium. The experiments were performed with 36 overlapped OMEGA beams using all standard OMEGA beam-smoothing techniques, including DPP's,⁷ PS,⁸ and SSD.⁹ The diagnostics probed the central region of the target, which had the same illumination conditions as cryogenic spherical implosions. Figure 117.14(a) shows the pulse shape used during one of the experiments. The measured shock velocity as a function of time (solid curve) is shown in Fig. 117.14(b). The data are compared with the 1-D predictions, shown by the dotted curve. In the 1-D prediction, the picket pulse launches the first shock, which decays as it travels through the target. This is shown by the decreasing shock velocity as a function of time. As a compression wave is launched by the shaped laser pulse starting at ~ 1.2 ns, the shock velocity gradually decreases in the simulation. The measurements indicate that the

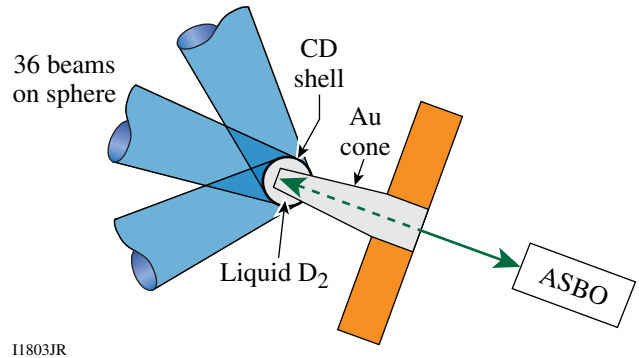


Figure 117.13

Schematic of shock-timing experiments consisting of spherical $10\text{-}\mu\text{m}$ -thick CD shells filled with liquid deuterium driven with 36 overlapped OMEGA beams. The targets have openings for active shock breakout (*ASBO*) diagnostics to probe shocks in liquid deuterium.

compression wave turns into a shock wave inside the target. The measured shock velocity from the first shock is smaller than predicted. This measurement suggests that energy coupling from the picket and low-intensity part of the pulse is reduced, compared to the simulation. The adiabat (the ratio of the plasma pressure to the Fermi pressure of a fully degenerate electron gas) of the CD shell and D_2 fuel is likely higher than simulated, leading to compression degradation in spherical implosions.

Since 1-D simulations incorrectly predict the shock timing, experimental measurements can be used to tune multiple hydrodynamic waves. Experimentally, it is easier to tune shock waves than compression waves because the multiple shock

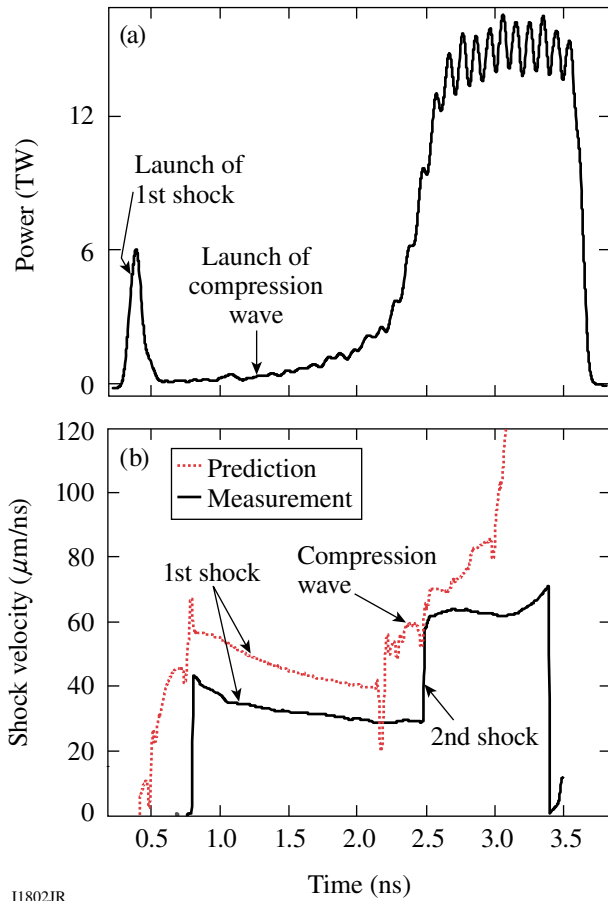


Figure 117.14

(a) The laser pulse shape for the continuous laser-pulse experiments. (b) The measured (solid line) and simulated (dotted line) shock velocities as a function of time.

waves are much easier to create and interpret. Figure 117.15(a) shows the double-picket pulse shape used for one such experiment and the measured shock velocity as a function of time [solid curve in Fig. 117.15(b)]. The data are compared with the 1-D prediction shown by the dotted curve. In the 1-D prediction, the first picket sends the first shock wave that decays as it travels through the target. The second picket sends a stronger second shock that travels faster and overtakes the first shock wave at ~ 2 ns. The main part of the pulse sends a third shock wave, which coalesces with the two earlier shocks at ~ 4 ns. The experiment shows that the shocks coalesce. The shock velocities are smaller, however, in the experiment, indicating that the shock coalescence events occur at different spatial locations than predicted. Future experiments will tune shock waves using triple-picket pulses with the square main pulse. This technique is similar to that used for shock tuning in indirect-drive-ignition designs.^{1,2,21}

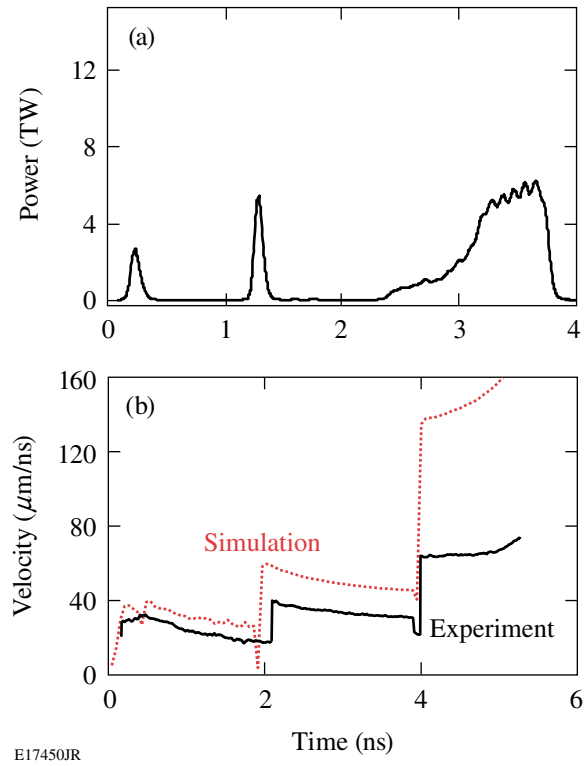


Figure 117.15

(a) The pulse shape for the double-picket, laser-pulse experiments. (b) The measured (solid line) and simulated (dotted line) shock velocities as a function of time.

Cryogenic-Target Compression

Figure 117.16 shows compression results obtained in spherical implosions with outer $10\text{-}\mu\text{m}$ -thick CD ablaters and inner $95\text{-}\mu\text{m}$ -thick cryogenic- D_2 -ice fuel shells. Figure 117.16(a) shows three examples of continuous laser pulses at a peak intensity range from $\sim 5 \times 10^{14}$ W/cm² to $\sim 8 \times 10^{14}$ W/cm². Figure 117.16(b) shows an example of a double-picket pulse at a peak intensity range of $\sim 9 \times 10^{14}$ W/cm². Figure 117.16(c) shows a comparison of the compression results obtained with these two types of laser pulses in which the neutron-averaged areal density was predicted to be ~ 250 mg/cm² if the shock pulses were properly timed. The highest compression with measured areal density in the range of 180 to 200 mg/cm² was obtained at the peak intensity of $\sim 5 \times 10^{14}$ W/cm². Two of the four data points at this intensity were presented in Ref. 5, while the other two were obtained recently, showing a good repeatability of these results. The neutron yield varied by a factor of ~ 5 because of variations of the inner ice roughness in these implosions. While the yield varied, the areal density did not, showing that the areal density is a robust measure of target compression, as previously shown in plastic implosions.²³

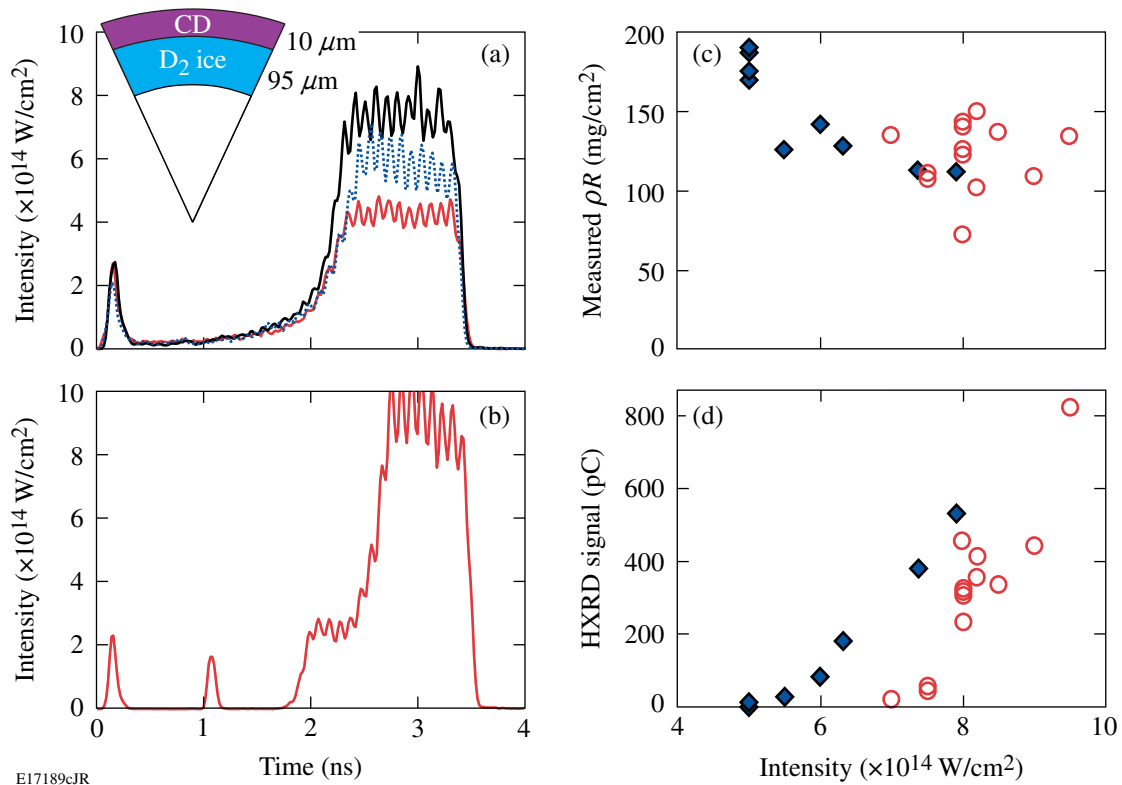


Figure 117.16

(a) Schematic of spherical targets used in implosions consisting of outer 10- μm -thick CD ablaters and 95- μm -thick inner cryogenic-D₂-ice shells driven with continuous laser pulses at peak intensities ranging from $\sim 5 \times 10^{14} \text{ W/cm}^2$ to $\sim 8 \times 10^{14} \text{ W/cm}^2$. (b) An example of a double-picket laser pulse with a peak intensity of $\sim 9 \times 10^{14} \text{ W/cm}^2$. (c) Measured neutron-averaged areal density as a function of peak drive intensity with continuous (diamonds) and double-picket (circles) pulses. (d) Hard x-ray signal as a function of peak drive intensity with continuous (diamonds) and double-picket (circles) pulses.

By increasing the peak intensity in the continuous-pulse implosions, the areal density did not increase, shown by the diamonds in Fig. 117.16(c). As discussed in the previous section, the shocks were not properly timed in these implosions, resulting in a decrease of the measured compression. The better-timed, double-picket implosions produced higher compression with areal densities up to $\sim 150 \text{ mg/cm}^2$ at high peak intensities, shown by the open circles [Fig. 117.16(c)]. Variations in these data are caused by variations in the picket energies and uncertainties for the shock-timing experiments. These multiple-picket designs are being optimized in current campaigns. Figure 117.16(d) presents the measured hard x-ray signal, produced by hot electrons from TPD instability, as a function of peak intensity for both types of drive pulses. The hard x-ray signal increases with peak intensity.²⁴ The preheat energy, which is estimated based on the measured hard x-ray signal, is of the order of $\sim 20 \text{ J}$ in the high-intensity implosions.⁴ This corresponds to $\sim 0.1\%$ of the total laser energy.⁴ With such levels of preheat, the areal density is expected to

be reduced from $\sim 250 \text{ mg/cm}^2$ to $\sim 210 \text{ mg/cm}^2$, if shock timing is optimized. These levels of preheat should not preclude obtaining an ignition-relevant areal density of $\sim 200 \text{ mg/cm}^2$ at peak intensities of $\sim 1 \times 10^{15} \text{ W/cm}^2$. The fact that the measured compression is below this level suggests that shock timing still must be improved and/or the hot-electron preheat is larger than previously estimated. Future experiments with both triple-picket pulse shapes and high-Z ablaters will address the most important issues in the direct-drive program.

Preheat

An important source of compression degradation is the shell preheat caused by hot electrons generated by TPD instability.^{4,18,19,24} This preheat was shown to be virulent in DT and D₂ ablaters^{4,24} and was reduced by using plastic ablaters.^{4,5} As a result, the highest, ignition-relevant areal densities with shell ρR of $\sim 200 \text{ mg/cm}^2$ were achieved in cryogenic D₂-fuel implosions with plastic ablaters when the hot-electron preheat was reduced to zero, at a moderate laser-drive peak intensity of

$\sim 5 \times 10^{14}$ W/cm² (Ref. 5). By increasing the peak intensity to $\sim 1 \times 10^{15}$ W/cm², the implosion velocity can be raised to levels required for ignition, but hard x-ray signals, associated with TPD hot electrons, also increase,²⁴ as shown in Fig. 117.16(d). While current hot-electron preheat estimates in plastic-ablator OMEGA implosions (with the estimated cold-shell preheat-energy fraction approaching $\sim 0.1\%$ of the total laser energy) do not preclude achieving ignition-relevant compression (with shell ρR of ~ 200 mg/cm²) at high peak intensities of $\sim 1 \times 10^{15}$ W/cm² and an initial shell adiabat of $\alpha \sim 2$ (Ref. 4), the longer plasma scale lengths in NIF targets make them potentially more vulnerable to hot-electron production than OMEGA targets.²⁴ While there are no reliable predictive capabilities for hot-electron preheat due to the very complex nature of nonlinear TPD instability, higher-Z ablaters are expected to mitigate the hot-electron preheat compared to the plastic ablaters. Plastic ablaters with 5% by atom of Si dopant were used recently²⁵ for this purpose.

Figure 117.17 shows a comparison of the hard x-ray signals measured in plastic and Si-doped plastic implosions. The implosions were performed with shaped pulses in which the peak intensity varied from ~ 0.8 to $\sim 1.1 \times 10^{15}$ W/cm² and a drive energy from ~ 18 to ~ 27 kJ. Two representative pulse shapes are shown in Fig. 117.17(a). The plastic and Si-doped plastic shells were $27 \mu\text{m}$ thick, and the concentration of Si dopant in plastic shells was 5% by atom. The comparison of the measured hard x-ray signals in the >40 -keV range [Fig. 117.17(b)] shows that the signals grow exponentially with the drive energy in CH implosions as drive energy increases. The signals were reduced in Si-doped CH shells at low drive energies; the reduction was $\sim 1.5\times$ at higher drive energies and peak intensities of $\sim 1.1 \times$

10^{15} W/cm². Future experiments will use higher-Z ablaters to further reduce hot-electron preheat.

Conclusions

This article has reviewed progress in cryogenic-implosion physics on OMEGA. After achieving ignition-relevant areal densities of ~ 200 mg/cm² in cryogenic-D₂ implosions at peak laser-drive intensities of $\sim 5 \times 10^{14}$ W/cm², the focus of the program has been on understanding the compression physics at peak laser-drive intensities of $\sim 1 \times 10^{15}$ W/cm² that are required to achieve ignition-relevant implosion velocities. Acceleration experiments showed the importance of the non-local electron-thermal-transport effects in modeling the laser drive. The nonlocal, hot-electron preheat was shown to stabilize Rayleigh–Taylor growth at a peak drive intensity of $\sim 1 \times 10^{15}$ W/cm². The measured compressibility of plastic targets driven with high-compression, shaped pulses agrees well with 1-D predictions. Shock mistiming has been shown to be an important mechanism in compression degradation of recent cryogenic implosions driven with continuous pulses. Cryogenic implosions driven with double-picket pulses, which are easier to tune than continuous pulses, demonstrate an improvement in compression performance at a peak drive intensity of $\sim 1 \times 10^{15}$ W/cm². The shell preheat caused by hot electrons generated by two-plasmon-decay instability was reduced by using Si-doped ablaters. Future experiments will investigate higher-Z ablaters (such as glass or Si) for further hot-electron preheat reduction. Significant progress in understanding ignition-relevant cryogenic target implosions has been made on OMEGA since the publication of Ref. 4.

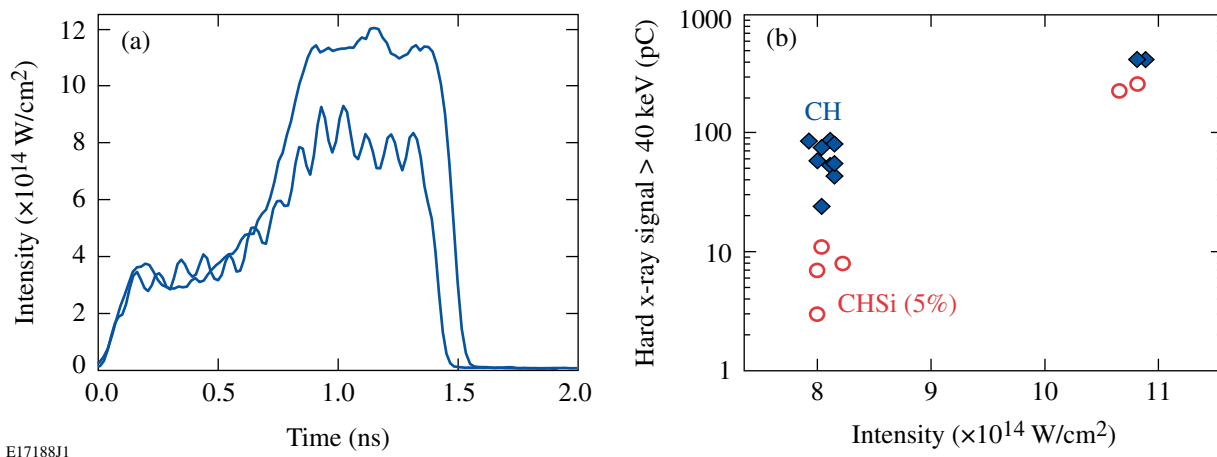


Figure 117.17

(a) Two representative pulse shapes used to implode $27\text{-}\mu\text{m}$ -thick plastic shells and Si-doped (5% by atom) plastic shells. (b) Hard x-ray signals measured in plastic (diamonds) and Si-doped (circles) implosions.

ACKNOWLEDGMENT

This work was supported by the U.S. Department of Energy Office of Inertial Confinement Fusion under Cooperative Agreement No. DE-FC52-08NA28302, the University of Rochester, and the New York State Energy Research and Development Authority. The support of DOE does not constitute an endorsement by DOE of the views expressed in this article.

REFERENCES

1. S. Atzeni and J. Meyer-ter-Vehn, *The Physics of Inertial Fusion: Beam Plasma Interaction, Hydrodynamics, Hot Dense Matter*, International Series of Monographs on Physics (Clarendon Press, Oxford, 2004).
2. J. D. Lindl, *Inertial Confinement Fusion: The Quest for Ignition and Energy Gain Using Indirect Drive* (Springer-Verlag, New York, 1998).
3. S. E. Bodner *et al.*, Phys. Plasmas **7**, 2298 (2000).
4. R. L. McCrory, D. D. Meyerhofer, R. Betti, R. S. Craxton, J. A. Delettrez, D. H. Edgell, V. Yu. Glebov, V. N. Goncharov, D. R. Harding, D. W. Jacobs-Perkins, J. P. Knauer, F. J. Marshall, P. W. McKenty, P. B. Radha, S. P. Regan, T. C. Sangster, W. Seka, R. W. Short, S. Skupsky, V. A. Smalyuk, J. M. Soures, C. Stoeckl, B. Yaakobi, D. Shvarts, J. A. Frenje, C. K. Li, R. D. Petrasso, and F. H. Séguin, Phys. Plasmas **15**, 055503 (2008).
5. T. C. Sangster, V. N. Goncharov, P. B. Radha, V. A. Smalyuk, R. Betti, R. S. Craxton, J. A. Delettrez, D. H. Edgell, V. Yu. Glebov, D. R. Harding, D. Jacobs-Perkins, J. P. Knauer, F. J. Marshall, R. L. McCrory, P. W. McKenty, D. D. Meyerhofer, S. P. Regan, W. Seka, R. W. Short, S. Skupsky, J. M. Soures, C. Stoeckl, B. Yaakobi, D. Shvarts, J. A. Frenje, C. K. Li, R. D. Petrasso, and F. H. Séguin, Phys. Rev. Lett. **100**, 185006 (2008).
6. S. X. Hu, V. A. Smalyuk, V. N. Goncharov, S. Skupsky, T. C. Sangster, D. D. Meyerhofer, and D. Shvarts, Phys. Rev. Lett. **101**, 055002 (2008).
7. Y. Lin, T. J. Kessler, and G. N. Lawrence, Opt. Lett. **20**, 764 (1995).
8. T. R. Boehly, V. A. Smalyuk, D. D. Meyerhofer, J. P. Knauer, D. K. Bradley, R. S. Craxton, M. J. Guardalben, S. Skupsky, and T. J. Kessler, J. Appl. Phys. **85**, 3444 (1999).
9. S. P. Regan, J. A. Marozas, J. H. Kelly, T. R. Boehly, W. R. Donaldson, P. A. Jaanimagi, R. L. Keck, T. J. Kessler, D. D. Meyerhofer, W. Seka, S. Skupsky, and V. A. Smalyuk, J. Opt. Soc. Am. B **17**, 1483 (2000).
10. R. C. Malone, R. L. McCrory, and R. L. Morse, Phys. Rev. Lett. **34**, 721 (1975).
11. V. N. Goncharov, O. V. Gotchev, E. Vianello, T. R. Boehly, J. P. Knauer, P. W. McKenty, P. B. Radha, S. P. Regan, T. C. Sangster, S. Skupsky, V. A. Smalyuk, R. Betti, R. L. McCrory, D. D. Meyerhofer, and C. Cherfils-Clérouin, Phys. Plasmas **13**, 012702 (2006).
12. S. G. Glendinning, S. N. Dixit, B. A. Hammel, D. H. Kalantar, M. H. Key, J. D. Kilkenny, J. P. Knauer, D. M. Pennington, B. A. Remington, R. J. Wallace, and S. V. Weber, Phys. Rev. Lett. **78**, 3318 (1997).
13. H. Azechi *et al.*, Phys. Plasmas **4**, 4079 (1997).
14. V. A. Smalyuk, S. X. Hu, V. N. Goncharov, D. D. Meyerhofer, T. C. Sangster, D. Shvarts, C. Stoeckl, B. Yaakobi, J. A. Frenje, and R. D. Petrasso, Phys. Rev. Lett. **101**, 025002 (2008).
15. V. A. Smalyuk, S. X. Hu, V. N. Goncharov, D. D. Meyerhofer, T. C. Sangster, C. Stoeckl, and B. Yaakobi, Phys. Plasmas **15**, 082703 (2008).
16. R. Betti, V. N. Goncharov, R. L. McCrory, and C. P. Verdon, Phys. Plasmas **5**, 1446 (1998).
17. Y. C. Lee and P. K. Kaw, Phys. Rev. Lett. **32**, 135 (1974).
18. C. S. Liu and M. N. Rosenbluth, Phys. Fluids **19**, 967 (1976).
19. C. Stoeckl, R. E. Bahr, B. Yaakobi, W. Seka, S. P. Regan, R. S. Craxton, J. A. Delettrez, R. W. Short, J. Myatt, A. V. Maximov, and H. Baldis, Phys. Rev. Lett. **90**, 235002 (2003).
20. S. X. Hu, V. A. Smalyuk, V. N. Goncharov, J. P. Knauer, P. B. Radha, I. V. Igumenshchev, J. A. Marozas, C. Stoeckl, B. Yaakobi, D. Shvarts, T. C. Sangster, P. W. McKenty, D. D. Meyerhofer, S. Skupsky, and R. L. McCrory, Phys. Rev. Lett. **100**, 185003 (2008).
21. T. R. Boehly, D. H. Munro, P. M. Celliers, R. E. Olson, D. G. Hicks, V. N. Goncharov, G. W. Collins, H. F. Robey, S. X. Hu, J. A. Marozas, T. C. Sangster, O. L. Landen, and D. D. Meyerhofer, Phys. Plasmas **16**, 056302 (2008).
22. P. M. Celliers, D. K. Bradley, G. W. Collins, D. G. Hicks, T. R. Boehly, and W. J. Armstrong, Rev. Sci. Instrum. **75**, 4916 (2004).
23. V. A. Smalyuk, R. Betti, J. A. Delettrez, V. Yu. Glebov, V. N. Goncharov, D. Y. Li, D. D. Meyerhofer, S. P. Regan, S. Roberts, T. C. Sangster, C. Stoeckl, W. Seka, J. A. Frenje, C. K. Li, R. D. Petrasso, and F. H. Séguin, Phys. Plasmas **14**, 022702 (2007).
24. V. A. Smalyuk, D. Shvarts, R. Betti, J. A. Delettrez, D. H. Edgell, V. Yu. Glebov, V. N. Goncharov, R. L. McCrory, D. D. Meyerhofer, P. B. Radha, S. P. Regan, T. C. Sangster, W. Seka, S. Skupsky, C. Stoeckl, B. Yaakobi, J. A. Frenje, C. K. Li, R. D. Petrasso, and F. H. Séguin, Phys. Rev. Lett. **100**, 185005 (2008).
25. J. P. Knauer, P. B. Radha, V. N. Goncharov, I. V. Igumenshchev, R. Betti, R. Epstein, F. J. Marshall, S. P. Regan, V. A. Smalyuk, D. D. Meyerhofer, and S. Skupsky, Bull. Am. Phys. Soc. **52**, 233 (2007).

Diagnosing Fuel ρR and ρR Asymmetries in Cryogenic DT Implosions Using Charged-Particle Spectrometry on OMEGA

Introduction

Cryogenic deuterium–tritium (DT) capsules are routinely imploded on LLE’s OMEGA Laser System.¹ These implosions are hydrodynamically equivalent to the baseline direct-drive-ignition design for the National Ignition Facility (NIF)² to allow for experimental validation of the design prior to the first ignition experiments at the NIF. The design consists of a cryogenic-DT-fuel layer inside a thin spherical ablator,³ which is compressed quasi-isentropically to minimize the laser energy required to achieve ignition conditions. If the capsule is sufficiently compressed, the high areal density (ρR) of the cryogenic DT fuel can support a propagating thermonuclear burn wave due to local bootstrap heating by the DT-alpha particles. Maximizing ρR for a given on-capsule laser energy is therefore very important. Determining ρR is also important for assessing implosion performance during all stages of development from energy-scaled cryogenic DT implosions on OMEGA to cryogenic fizzes to ignited implosions on the NIF. Determining fuel ρR in moderate- ρR (100 to 200 mg/cm²) cryogenic DT implosions has been challenging since it requires the development of new spectrometry techniques and analysis methods. A new type of neutron spectrometer, the magnetic recoil spectrometer (MRS),^{4–6} has been built, installed, and calibrated on OMEGA to measure primarily the down-scattered DT neutron spectrum, from which ρR of the fuel can be directly inferred. Another MRS is currently being developed to diagnose high- ρR cryogenic DT-capsule implosions on the NIF.

This article describes a complementary method for analyzing the spectral shape of knock-on deuterons (KOD’s), elastically scattered by primary DT neutrons, from which ρR can be inferred for values up to ~ 200 mg/cm². This new analysis method, which uses Monte Carlo modeling⁷ of a cryogenic DT implosion, significantly improves, in two fundamental ways, the existing analysis method, which uses a relatively simple implosion model to relate the fuel ρR to the KOD yield in the high-energy peak.^{8–10} First, it is not affected by significant spatial-yield variations, which degrade the diagnosis of fuel ρR (spatial-yield variations of about $\pm 20\%$ are typically observed).

Secondly, it does not break down when the fuel ρR exceeds ~ 70 mg/cm². Modeling the actual shape of the KOD spectrum is therefore a more powerful method than the yield method for diagnosing the fuel ρR in cryogenic DT implosions.

The following sections describe the analysis method used to model the KOD spectrum, from which a ρR of the fuel can be inferred for a cryogenic DT implosion; present the experiments, data analysis, and results; and summarize the article.

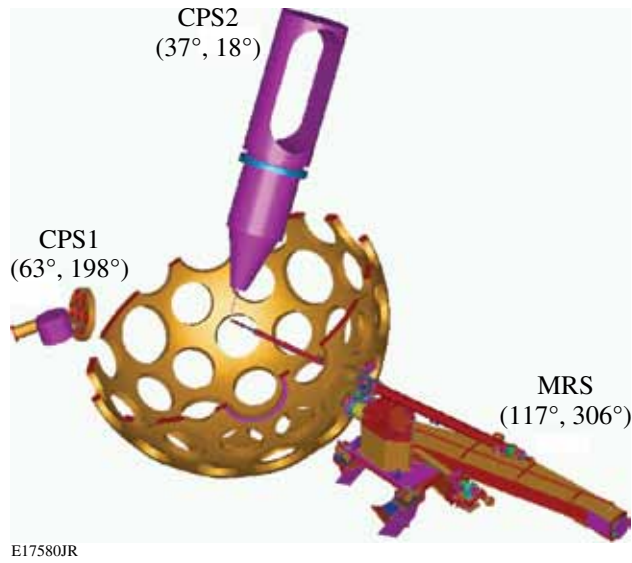
Diagnosing Fuel ρR in Moderate- ρR Cryogenic DT Implosions Using Knock-On Deuterons

Fuel ρR in DT-filled CH-capsule implosions has been diagnosed routinely at the Omega Laser Facility for more than a decade.^{8–10} In those experiments, two magnet-based charged-particle spectrometers (CPS’s)¹¹ have been used to measure the KOD spectrum in two different directions. With the recent implementation of the MRS, a third measurement of the KOD spectrum is now possible (the MRS can be operated in a charged-particle mode, which involves removing the conversion foil near the implosion⁵ and operating the system like a normal charged-particle spectrometer). Since both ρR and ρR symmetry are important measures of the performance of a cryogenic DT implosion, the MRS adds significantly to the existing ρR -diagnostic suite on OMEGA (Fig. 117.18).

For a fuel ρR around 100 mg/cm², about 1% of the primary DT neutrons elastically scatter off the deuterium, producing KOD’s with energies up to 12.5 MeV as expressed by the reaction



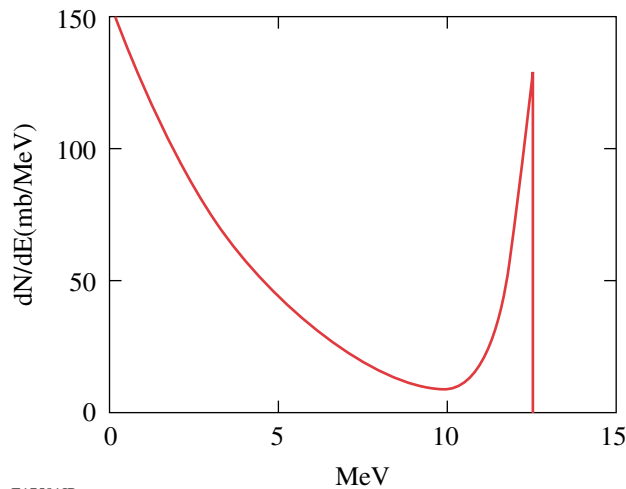
At this neutron energy, the differential cross section for the nD-elastic scattering in the central-mass system is well known and represents the birth spectrum of the KOD’s (see Fig. 117.19). As the KOD’s pass through the high-density DT fuel, they lose energy in proportion to the amount of material through which they pass (ρR). A ρR value for the portion of the implosion



E17580JR

Figure 117.18

The magnetic recoil spectrometer (MRS) and the charged-particle spectrometers CPS1 and CPS2 on the OMEGA chamber. These spectrometers are used to simultaneously measure spectra of elastically scattered deuterons, so-called knock-on deuterons (KOD's), from which fuel ρR and ρR asymmetries in cryogenic DT implosions can be directly inferred. The MRS can operate in either charged-particle or down-scattered neutron mode; the latter mode allows one to measure the down-scattered neutron spectrum, from which the ρR of the fuel can be inferred as well.



E17581JR

Figure 117.19

The birth spectrum of knock-on deuterons (KOD's), elastically scattered by primary 14.1-MeV neutrons. Due to kinematics, the KOD high-energy end point is at 12.5 MeV.

facing a given spectrometer can therefore be determined from the shape of the measured KOD spectrum by using theoretical formulation of the slowing down of deuteron energy in a plasma.¹² Previous work used a relatively simple model to relate the fuel ρR to the yield under the high-energy peak of the KOD spectrum.^{8–10} That model, however, is subject to significant spatial-yield variations that degrade the diagnosis of the fuel ρR (spatial yield variations of about $\pm 20\%$ are typically observed). It also breaks down when the fuel ρR exceeds ~ 70 mg/cm² because the KOD spectrum becomes sufficiently distorted by the effects of energy slowing down that the measurement of the high-energy peak becomes ambiguous; an accurate determination of ρR must therefore rely on more-sophisticated modeling. Monte Carlo modeling of an implosion, similar to the modeling described in Ref. 7, was instead used to simulate the KOD spectrum from which a fuel ρR can be inferred. This made it possible to use more-realistic temperature and density profiles than those in the hot-spot and uniform models described in Refs. 8–10. From the Monte Carlo modeling, it was established that the shape of the KOD spectrum depends mainly on fuel ρR and that density and electron-temperature profile variations typically predicted in the high-density region play minor roles. This was concluded by studying how the spectral shape varied with varying temperature and density profiles for a fixed ρR . The variations were made to still meet a measured burn-averaged ion temperature of 2.0 ± 0.5 keV, a radius of the high-density region of 30 ± 10 μ m, and a peak density of 10 to 160 g/cc (peak density varied less for a fixed ρR). The envelopes (represented by the standard deviation) in which the density and temperature profiles were varied are illustrated in Fig. 117.20 for a fuel ρR of 105 mg/cm². The resulting simulated birth profiles of the primary neutrons and KOD's are also shown in Fig. 117.20. Figure 117.21 shows how the simulated KOD spectrum varies with varying ρR . The error bars (standard deviation) shown in each spectrum represent the effect of varying density and temperature profiles, and as indicated by the error bars, the shape of the KOD spectrum depends weakly on any profile variations. In contrast, the spectral shape depends strongly on ρR . In addition, the modeling was constrained strictly by isobaric conditions at bang time, burn duration, DT-fuel composition, and a steady state during burn. As discussed in Ref. 13, the latter constraint is an adequate approximation for these types of measurements since the time evolution of the fuel ρR does not affect significantly the shape of the burn-averaged spectrum, which simplifies the ρR interpretation of the measured KOD spectrum. Multidimensional features could, on the other hand, affect the analysis and interpretation of the KOD spectrum since these effects would manifest themselves

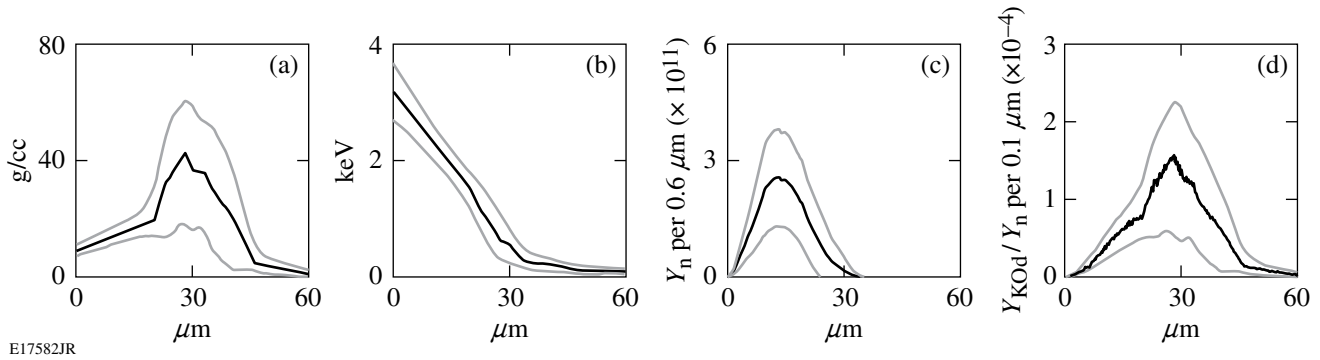


Figure 117.20

(a) Density and (b) temperature profiles used to model a cryogenic DT implosion with a ρR of 105 mg/cm^2 . The black line represents the average, while the gray lines indicate the envelopes (represented by the standard deviation) in which the density and temperature profiles were varied. The variations were made to still meet the measured burn-averaged ion temperature of $2.0 \pm 0.5 \text{ keV}$ and the position of the high-density region of $30 \pm 10 \text{ } \mu\text{m}$. Resulting birth profiles of the primary neutrons and KOD's are shown in (c) and (d). In addition, the modeling was constrained by isobaric conditions at bang time, burn duration, DT-fuel composition, and steady state during burn.

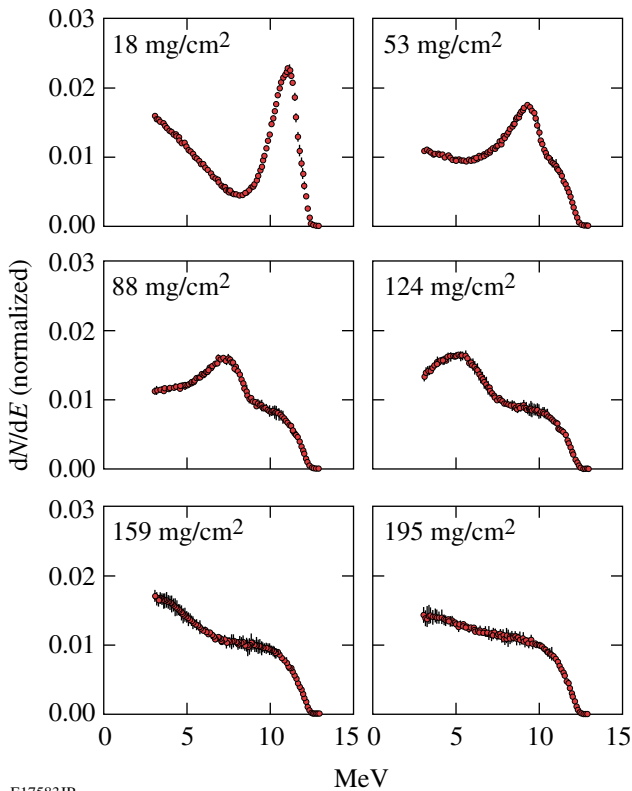


Figure 117.21

KOD spectra for different fuel ρR 's. The error bars (standard deviation) shown in each spectrum represent the effect of varying density and temperature profiles. As illustrated, the shape of the KOD spectrum depends strongly on ρR , while density and temperature profile effects play minor roles as indicated by the error bars. The KOD spectra are normalized to unity.

by slightly smearing out the high-energy peak for low fuel ρR 's ($< 100 \text{ mg/cm}^2$). For higher ρR 's ($> 150 \text{ mg/cm}^2$), these effects should be less prominent since high-mode nonuniformities would not significantly alter the shape of the KOD spectrum.

Experiments, Data Analysis, and Results

The cryogenic DT-capsule implosions discussed in this article were driven with a laser pulse designed to keep the fuel on an adiabat α of approximately 1 to 3, where α is the ratio of the internal pressure to the Fermi-degenerate pressure.¹⁴ The on-capsule laser energy varied from 12 to 25 kJ, and the laser intensity varied from 3×10^{14} to 10^{15} W/cm^2 . Full single-beam smoothing was applied during all pulses by using distributed phase plates (DPP's),¹⁵ polarization smoothing (PS) with birefringent wedges,¹⁶ and 2-D, single-color-cycle, 1-THz smoothing by spectral dispersion (SSD).¹⁷ The ablator was typically made of 5 to 10 μm of deuterated polyethylene (CD), which was permeation filled with an equimolar mixture of DT gas to 1000 atm. At this pressure, the shell and gas were slowly cooled to a few degrees below the DT triple point (19.8 K), typically producing a DT-ice layer of 90- to 100- μm thickness,¹⁴ which is thicker than the OMEGA design energy scaled from the baseline direct-drive-ignition design for the NIF. The thicker DT ice was chosen to increase the shell stability during the acceleration phase of the implosion. In addition, by tailoring the adiabat in the shell and fuel, the expected imprint perturbation growth for such a thick shell is substantially reduced, further improving the implosion performance. Based on 1-D hydrocode simulations,¹⁸ the burn-averaged fuel ρR is in excess of 200 mg/cm^2 for these types of implosions.

Figure 117.22 shows examples of measured and fitted simulated KOD spectra for four different low-adiabat cryogenic DT implosions. From the simulated fits to the measured spectra, ρR values ranging from 25 to 205 mg/cm² were inferred. The relatively low ρR 's for shots 43070 and 43945 are primarily attributed to a nonoptimal-designed laser pulse shape that generated mistimed shocks. The performance of these implosions was also further degraded by the relatively large capsule offset of ~ 30 to $40 \mu\text{m}$ from target chamber center. Although the offset was about the same for shot 49035, the inferred ρR is significantly higher than for shots 43070 and 43945—a consequence of a better-designed laser pulse shape. The high ρR value for shot 48734 was achieved using the shock-ignition concept described in Refs. 19 and 20. The fact that the capsule was perfectly centered ($11 \pm 15 \mu\text{m}$) resulted in a determined ρR value close to the 1-D simulated value of about 200 mg/cm². In addition, it is notable that the high-energy endpoints are at the theoretical maximum of 12.5 MeV, demonstrating that KOD's are produced in the outermost parts of the implosion and the plastic ablator has been burnt away entirely.

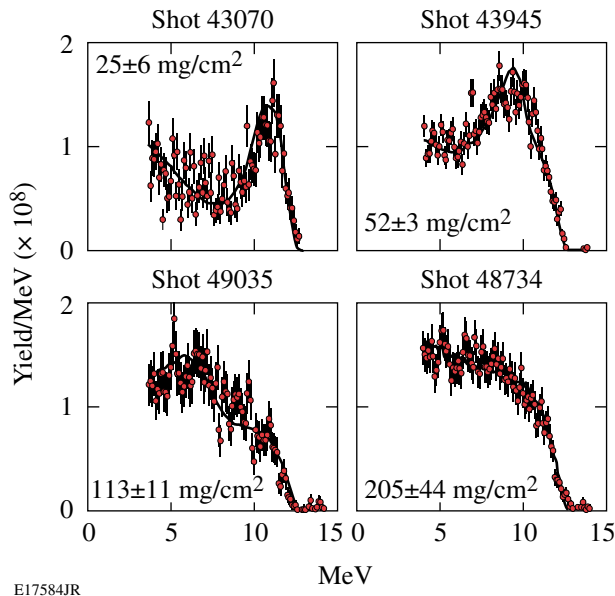


Figure 117.22 Examples of measured KOD spectra for four different low-adiabat, cryogenic DT implosions. Simulated fits (solid lines) to the measured spectra are also shown. From the fits, a fuel ρR of 25 ± 6 , 52 ± 3 , 113 ± 11 , and 205 ± 44 mg/cm² was determined for shots 43070, 43945, 49035, and 48734, respectively. The errors of the inferred ρR values are due mainly to modeling uncertainties as discussed in this article and statistical uncertainties in the experimental data. See text for more detailed information about these implosions.

The ρR data obtained for hydrodynamically equivalent cryogenic D₂ implosions¹⁴ were used to validate the ρR analysis of the KOD spectrum. Since a well-established ρR diagnostic technique exists for cryogenic D₂ implosions,²¹ this comparison provides a good check of the analysis method described herein. The comparison is made in Fig. 117.23, which illustrates the experimental ρR as a function of 1-D predicted ρR [Fig. 117.23(a)] and the observed ρR_{asym} as a function of capsule offset [Fig. 117.23(b)] for low-adiabat DT and D₂ implosions driven at various intensities. Both sets of data show similar behavior, demonstrating that the ρR analysis of the KOD spectrum is accurate.

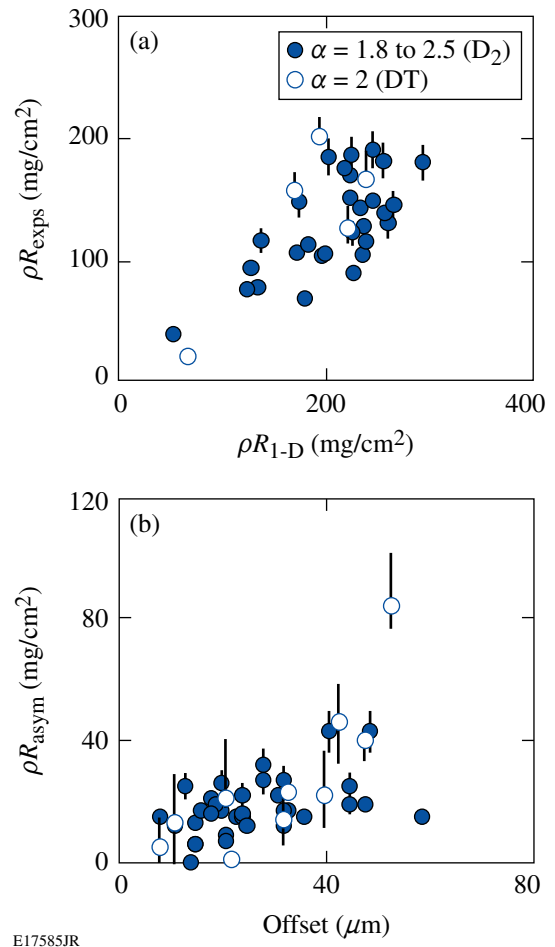


Figure 117.23 (a) Observed average ρR as a function of 1-D predicted ρR for implosions with a capsule offset of less than $40 \mu\text{m}$ to the target chamber center. (b) Observed ρR_{asym} as a function of capsule offset. These data sets are for low-adiabat DT (open data points) and D₂ (solid data points) implosions driven at various intensities. Similar performance relative to 1-D and similar ρR_{asym} as a function of capsule offset are observed for both the DT and D₂ implosions, indicating that the ρR analysis of the KOD spectrum is accurate.

Summary and Conclusions

Through Monte Carlo modeling of a cryogenic DT implosion it has been demonstrated that ρR 's for moderate- ρR ($<200 \text{ mg/cm}^2$) cryogenic DT implosions on OMEGA can be determined accurately from the shape of the measured KOD spectrum. Results from the Monte Carlo modeling of an implosion have provided a deeper understanding of the relationship between ρR , implosion structure, and KOD production. In particular, it was established that the shape of the KOD spectrum depends mainly on ρR , and that effects of spatially varying density and temperature profiles play minor roles. It should be pointed out that multidimensional features could have an effect on the analysis and interpretation of the KOD spectrum since these effects would manifest themselves by slightly smearing out the high-energy peak for low fuel ρR 's ($<100 \text{ mg/cm}^2$). For higher ρR 's ($>150 \text{ mg/cm}^2$), these effects should be less prominent since high-mode nonuniformities would not significantly alter the shape of the KOD spectrum. The ρR analysis of the KOD spectrum was also validated by comparing these results to ρR data obtained for hydrodynamically equivalent cryogenic D_2 implosions using a well-established ρR diagnostic technique. The good agreement observed between the two analysis methods indicates that the KOD analysis method described herein is accurate.

ACKNOWLEDGMENT

The work described here was supported in part by the U.S. Department of Energy (Grant No. DE-FG03-03SF22691), LLE (No. 412160-001G), LLNL (No. B504974), and GA under DOE (DE-AC52-06NA27279). This work was also supported by the U.S. Department of Energy Office of Inertial Confinement Fusion under Cooperative Agreement No. DE-FC52-08NA28302, the University of Rochester, and the New York State Energy Research and Development Authority. The support of DOE does not constitute an endorsement by DOE of the views expressed in this article.

REFERENCES

1. T. R. Boehly, D. L. Brown, R. S. Craxton, R. L. Keck, J. P. Knauer, J. H. Kelly, T. J. Kessler, S. A. Kumpan, S. J. Loucks, S. A. Letzring, F. J. Marshall, R. L. McCrory, S. F. B. Morse, W. Seka, J. M. Soures, and C. P. Verdon, *Opt. Commun.* **133**, 495 (1997).
2. G. H. Miller, E. I. Moses, and C. R. Wuest, *Nucl. Fusion* **44**, S228 (2004).
3. P. W. McKenty, V. N. Goncharov, R. P. J. Town, S. Skupsky, R. Betti, and R. L. McCrory, *Phys. Plasmas* **8**, 2315 (2001).
4. J. A. Frenje, K. M. Green, D. G. Hicks, C. K. Li, F. H. Séguin, R. D. Petrasso, T. C. Sangster, T. W. Phillips, V. Yu. Glebov, D. D. Meyerhofer, S. Roberts, J. M. Soures, C. Stoeckl, K. Fletcher, S. Padalino, and R. J. Leeper, *Rev. Sci. Instrum.* **72**, 854 (2001).
5. J. A. Frenje, D. T. Casey, C. K. Li, J. R. Rygg, F. H. Séguin, R. D. Petrasso, V. Yu. Glebov, D. D. Meyerhofer, T. C. Sangster, S. Hatchett, S. Haan, C. Cerjan, O. Landen, M. Moran, P. Song, D. C. Wilson, and R. J. Leeper, *Rev. Sci. Instrum.* **79**, 10E502 (2008).
6. V. Yu. Glebov, D. D. Meyerhofer, T. C. Sangster, C. Stoeckl, S. Roberts, C. A. Barrera, J. R. Celeste, C. J. Cerjan, L. S. Dauffy, D. C. Eder, R. L. Griffith, S. W. Haan, B. A. Hammel, S. P. Hatchett, N. Izumi, J. R. Kimbrough, J. A. Koch, O. L. Landen, R. A. Lerche, B. J. MacGowan, M. J. Moran, E. W. Ng, T. W. Phillips, P. M. Song, R. Tommasini, B. K. Young, S. E. Caldwell, G. P. Grim, S. C. Evans, J. M. Mack, T. Sedillo, M. D. Wilke, D. C. Wilson, C. S. Young, D. Casey, J. A. Frenje, C. K. Li, R. D. Petrasso, F. H. Séguin, J. L. Bourgade, L. Disdier, M. Houry, I. Lantuejoul, O. Landoas, G. A. Chandler, G. W. Cooper, R. J. Leeper, R. E. Olson, C. L. Ruiz, M. A. Sweeney, S. P. Padalino, C. Horsfield, and B. A. Davis, *Rev. Sci. Instrum.* **77**, 10E715 (2006).
7. S. Kurebayashi, J. A. Frenje, F. H. Séguin, J. R. Rygg, C. K. Li, R. D. Petrasso, V. Yu. Glebov, J. A. Delettrez, T. C. Sangster, D. D. Meyerhofer, C. Stoeckl, J. M. Soures, P. A. Amendt, S. P. Hatchett, and R. E. Turner, *Phys. Plasmas* **12**, 032703 (2005).
8. S. Skupsky and S. Kacendar, *J. Appl. Phys.* **52**, 2608 (1981).
9. S. Kacendar, S. Skupsky, A. Entenberg, L. Goldman, and M. Richardson, *Phys. Rev. Lett.* **49**, 463 (1982).
10. C. K. Li, F. H. Séguin, D. G. Hicks, J. A. Frenje, K. M. Green, S. Kurebayashi, R. D. Petrasso, D. D. Meyerhofer, J. M. Soures, V. Yu. Glebov, R. L. Keck, P. B. Radha, S. Roberts, W. Seka, S. Skupsky, C. Stoeckl, and T. C. Sangster, *Phys. Plasmas* **8**, 4902 (2001).
11. F. H. Séguin, J. A. Frenje, C. K. Li, D. G. Hicks, S. Kurebayashi, J. R. Rygg, B.-E. Schwartz, R. D. Petrasso, S. Roberts, J. M. Soures, D. D. Meyerhofer, T. C. Sangster, J. P. Knauer, C. Sorce, V. Yu. Glebov, C. Stoeckl, T. W. Phillips, R. J. Leeper, K. Fletcher, and S. Padalino, *Rev. Sci. Instrum.* **74**, 975 (2003).
12. C. K. Li and R. D. Petrasso, *Phys. Rev. Lett.* **70**, 3059 (1993).
13. J. A. Frenje, C. K. Li, J. R. Rygg, F. H. Séguin, D. T. Casey, R. D. Petrasso, J. Delettrez, V. Yu. Glebov, T. C. Sangster, O. Landen, and S. Hatchett, *Phys. Plasmas* **16**, 022702 (2009).
14. T. C. Sangster, R. Betti, R. S. Craxton, J. A. Delettrez, D. H. Edgell, L. M. Elasky, V. Yu. Glebov, V. N. Goncharov, D. R. Harding, D. Jacobs-Perkins, R. Janezic, R. L. Keck, J. P. Knauer, S. J. Loucks, L. D. Lund, F. J. Marshall, R. L. McCrory, P. W. McKenty, D. D. Meyerhofer, P. B. Radha, S. P. Regan, W. Seka, W. T. Shmayda, S. Skupsky, V. A. Smalyuk, J. M. Soures, C. Stoeckl, B. Yaakobi, J. A. Frenje, C. K. Li, R. D. Petrasso, F. H. Séguin, J. D. Moody, J. A. Atherton, B. D. MacGowan, J. D. Kilkenny, T. P. Bernat, and D. S. Montgomery, *Phys. Plasmas* **14**, 058101 (2007).
15. Y. Lin, T. J. Kessler, and G. N. Lawrence, *Opt. Lett.* **20**, 764 (1995).
16. T. R. Boehly, V. A. Smalyuk, D. D. Meyerhofer, J. P. Knauer, D. K. Bradley, R. S. Craxton, M. J. Guardalben, S. Skupsky, and T. J. Kessler, *J. Appl. Phys.* **85**, 3444 (1999).

17. S. Skupsky, R. W. Short, T. Kessler, R. S. Craxton, S. Letzring, and J. M. Soures, *J. Appl. Phys.* **66**, 3456 (1989).
18. J. Delettrez, *Can. J. Phys.* **64**, 932 (1986).
19. R. Betti, C. D. Zhou, K. S. Anderson, L. J. Perkins, W. Theobald, and A. A. Solodov, *Phys. Rev. Lett.* **98**, 155001 (2007).
20. W. Theobald, R. Betti, C. Stoeckl, K. S. Anderson, J. A. Delettrez, V. Yu. Glebov, V. N. Goncharov, F. J. Marshall, D. N. Maywar, R. L. McCrory, D. D. Meyerhofer, P. B. Radha, T. C. Sangster, W. Seka, D. Shvarts, V. A. Smalyuk, A. A. Solodov, B. Yaakobi, C. D. Zhou, J. A. Frenje, C. K. Li, F. H. Séguin, R. D. Petrasso, and L. J. Perkins, *Phys. Plasmas* **15**, 056306 (2008).
21. F. H. Séguin, C. K. Li, J. A. Frenje, S. Kurebayashi, R. D. Petrasso, F. J. Marshall, D. D. Meyerhofer, J. M. Soures, T. C. Sangster, C. Stoeckl, J. A. Delettrez, P. B. Radha, V. A. Smalyuk, and S. Roberts, *Phys. Plasmas* **9**, 3558 (2002).

Plasma Density Determination from X-Ray Radiography of Laser-Driven Spherical Implosions

The fuel layer density of an imploding spherical shell is inferred from x-ray radiographs. The density distribution is determined by using Abel inversion to compute the radial distribution of the opacity κ from the observed optical depth τ . With the additional assumption of the mass of the remaining cold fuel, the absolute density distribution can be determined. This is demonstrated on the OMEGA Laser System with two x-ray backlighters of different mean energies that lead to the same inferred density distribution independent of backlighter energy.

Recent experiments on the OMEGA laser have successfully inferred the areal density of the imploding capsule at the time of fusion particle production¹⁻³ (hot-spot formation). At this time, the hot-spot temperature is at maximum, whereas the cold main fuel layer is still evolving. The integral areal density of the capsule is determined from the slowing down of protons resulting from D-³He fusion reactions within the fuel. These can be either primary fusion reactions from a D³He gas fill or secondary reactions from a D₂ gas fill. This method determines the total areal density ρR by associating proton energy loss with the amount of plasma traversal. This method is fairly insensitive to the assumptions about the conditions of the plasma but is restricted to sampling the areal density at the time of fusion particle production.

In non-igniting capsules, the cold main fuel layer produces negligible fusion yield; therefore it is difficult to diagnose. The problem is solved by the introduction of an outside source of radiation (backlighter) acting as a probe. Both x-ray⁴ and proton backlighters⁵ have been employed as plasma probes in laser-driven fusion experiments. X-ray backlighters have been extensively used for both planar experiments and spherical implosions on OMEGA.⁶ X-ray backlighting of spherical implosions on OMEGA has been restricted to experiments using fewer than 60 beams to drive the target implosion, freeing up some of the beams to generate the x-ray backlighter emission. The recent completion of the Omega EP Facility⁷ will make it possible to generate a backlighter while using all 60 OMEGA beams to drive the implosion.

In this work it is shown that the density distribution of the plasma can be inferred from framed x-ray radiographs. With x-ray backlighter emission available during and after core formation, the time history of the main fuel layer's density, and therefore the areal density, can be determined. The use of two-dimensional (2-D) imaging techniques such as pinhole imaging, Kirkpatrick-Baez microscopes, and Bragg crystal diffraction are preferred since there may be significant azimuthal variation of the plasma density.

In contrast to a previous treatment of this problem where only the relative density distribution was determined,⁸ it is shown that with the application of Abel inversion and the further constraint of constant mass, the absolute plasma density distribution can be inferred from the framed x-ray radiographs. This is demonstrated using x-ray radiographs of polar-driven implosions⁹ on the OMEGA Laser System⁶ with simultaneous backlighters at a mean energy of ~ 2.3 keV (from broadband Au emission) and from ~ 4.7 -keV x rays (from a Ti backlighter). Despite a significant difference in the magnitude of the plasma opacity resulting from these two backlighters, the method yields the same density distribution when simultaneous framed images are compared.

Absorption of backlighter x rays along a path L follows the relation

$$I = I_0 \times \exp\left[-\int \mu(E, r)\rho(r)dr\right], \quad (1)$$

where I is the observed intensity, I_0 is the backlighter intensity, μ is the mass absorption coefficient at energy E in cm^2/g , and ρ is the density in g/cm^3 . If the density distribution is spherically symmetric, the integral can be re-expressed as

$$\kappa_A(E, y) = 2 \int_y^\infty \frac{\mu(E, r)\rho(r)rdr}{\sqrt{r^2 - y^2}}, \quad (2)$$

where $\kappa_A(E,y)$ is the Abel transform¹⁰ of the opacity $\kappa(E,r) = \mu(E,r) \rho(r)$ at the projected radial position y . The inverse Abel transform¹⁰ gives the radially dependent opacity

$$\kappa(E,r) = -\frac{1}{\pi} \int_r^\infty \frac{d\kappa_A}{dy} \frac{dy}{\sqrt{y^2 - r^2}}. \quad (3)$$

Normally applied to optically thin emission, Eq. (3), when combined with Eq. (1), determines the radial distribution of the opacity

$$\kappa(E,r) = \frac{1}{\pi} \int_r^\infty \frac{d}{dy} \left\{ \ln \left[\frac{I(y)}{I_0} \right] \right\} \frac{dy}{\sqrt{y^2 - r^2}}. \quad (4)$$

If the mass absorption coefficient is approximately constant through the plasma, as is the case for bound-free absorption¹¹ by inner-shell electrons, then

$$\rho(r) = \kappa(E,r) / \mu_{\text{eff}}(E), \quad (5)$$

where $\mu_{\text{eff}}(E)$ is the mass absorption coefficient averaged over the effective energy band of the radiograph. Because of uncertainties in the instrumental response or an incomplete knowledge of the spectral shape, it is difficult to determine the exact value of $\mu_{\text{eff}}(E)$. If, however, the mass of the plasma shell M_{shell} is assumed or obtained from simulations, then $\mu_{\text{eff}}(E)$ can be determined as follows:

$$M_{\text{shell}} = \int \rho(r) dV = 4\pi \int \frac{\kappa(E,r)}{\mu_{\text{eff}}(E)} r^2 dr, \quad (6)$$

$$\therefore \mu_{\text{eff}}(E) = \frac{4\pi}{M_{\text{shell}}} \int \kappa(E,r) \times r^2 dr. \quad (7)$$

By choosing M_{shell} to be the unablated mass, the absolute density is then determined. The applicability of this approximation has been previously explored¹² for deuterated polystyrene (CD) and shown to apply for absorption by the carbon atoms in the polystyrene when the temperature of the absorber is below ~ 100 eV and the density is below ~ 10 g/cm³. If the plasma is isothermal, the temperature restriction is further relaxed. Fujioka *et al.*¹³ have shown that absorption of x rays from a Ti backlighter (one of two used in this work) by polystyrene (CH) can indeed be characterized by an effective energy-band-dependent absorption coefficient.

If the absorber is fully stripped, as is the case for a pure-hydrogen fuel layer, and is at a sufficiently high temperature, as would be expected for a D or DT main fuel layer near stagnation, the opacity is $\propto \rho^2/T^{1/2}$, and, therefore, the optical depth is $\propto \rho^2 R/T^{1/2}$ (Refs. 14 and 15), where T is the temperature and R is the radius. If the temperature variation of the absorber is small, the radial variation of the opacity can be determined by Abel inversion from which a functional form of the density distribution can be determined. The assumption of constant mass allows one to calculate the absolute density distribution as a function of radius.

Experiments were performed using 40 beams of the OMEGA laser in the polar-drive illumination configuration,⁹ emulating the conditions on the NIF (the National Ignition Facility)¹⁶ when direct-drive implosions are performed with the beams in the indirect-drive configuration. The beam pointing used was described in Marshall *et al.*⁹ (case 3, with offsets of rings 1, 2, and 3 of 90, 150, and 150 μm , respectively) on a target with an outer radius of 433 μm . The target consisted of a 24- μm -thick glow-discharge-polymer (GDP) (i.e., CH) shell filled with 15 atm of D₂ at room temperature. The main drive pulse consisted of a 1.5-ns pulse with a 1-to-3 (foot-to-main) intensity ratio, with the foot and main part of the pulse having approximately equal durations (~ 0.75 ns). A total of 13.2 kJ was incident on the target with 1-THz-bandwidth smoothing by spectral dispersion (SSD)¹⁷ with polarization smoothing¹⁸ used to minimize small-scale illumination nonuniformities. This pulse shape was used to keep the main fuel layer on a low adiabat ($E/E_{\text{Fermi}} \sim 3$) (Ref. 19).

Two backlighter targets were employed opposite two x-ray framing cameras. One backlighter was a 25- μm -thick Au foil and the other a 25- μm -thick Ti foil, each with four OMEGA beams of ~ 350 J/beam, focused to diameters of 750 μm and 600 μm , respectively. Each framing camera was positioned behind a 4×4 array of 10- μm -diam pinholes producing four strips of framed images with a time-gated resolution of ~ 30 ps, 56 ps between images, and strip times independently set to the nearest 100 ps. Absolute frame times were determined by observing the backlighter onset on the first strip and from the measured delay from strip to strip determined from an electronically recorded monitor signal.

The images are recorded on film with an imposed step wedge, so that absolute intensity variations can be determined. The exposed images and step wedge are developed simultaneously to make possible the subsequent conversion to intensity

variation from scanned and digitized film. Variations of the backlighter intensity are removed by fitting the shape of the backlighter to a supergaussian-plus background outside the region of the target radiograph and then extending this fit to the region of the radiograph.²⁰

Figure 117.24 shows a set of these corrected radiographs up to shell stagnation, which occurs at ~ 2.3 ns. The values are presented as $-\ln(I/I_0)$ [i.e., the optical depth τ]; all values are >0 with the exception of the frames from 2.32 ns and on, where self-emission from the core exceeds emission from the backlighter in the central region of the images. Figure 117.25(a) shows the azimuthally averaged optical-depth variation for one nearly simultaneous pair (at the mean time of $t = 2.14$ ns) of Au- and Ti-backlit images. The magnitude of the optical depth is greater for the lower-energy backlighter, as expected. The dotted line in Fig. 117.25(a) is the Au-backlit profile divided by 1.7, showing that the optical depths differ by only a multiplicative constant. Applying Abel inversion and assuming the unablated shell mass (3.34×10^{-5} g) given by the one-dimensional (1-D) hydrodynamic code *LILAC*²¹ determines the density distributions from the observed optical depths [Fig. 117.25(b)]. The inferred density distributions from the Au and Ti backlighters are nearly identical, with only small differences due to noise in the images.

Figure 117.26 shows the density distributions determined for a sample of these images. The densities inferred from one

additional simultaneous pair of Au- and Ti-backlit images are included. The *LILAC*-simulated shell density is shown for comparison for the 2.20-ns case. Figure 117.27 shows the resulting calculated shell areal densities ρR_{shell} determined from all Au- and Ti-backlit images plotted as a function of frame time from the beginning of the main laser pulse ($t = 0$). For the two frames where the Au- and Ti-backlit images occurred at the same time, the areal density values are the same within errors. All times have an uncertainty of ± 50 ps. The absolute densities, and therefore areal densities, are assumed to be uncertain by $\pm 10\%$ because of an uncertainty in the unablated mass. The time from ~ 2.3 to 2.6 ns corresponds to the time during which intense x-ray emission from the core as well as fusion production occurs. During peak emission, heat from the core moves out through the shell and absorption by the backlighter is momentarily obscured. Since an independent measurement of this emission is not available (image with no backlighter), it cannot be corrected for and no density profiles are determined during this time interval. Later in time, the shell cools and absorption of the backlighter reappears. Frames during this later time were recorded by the Ti-backlit framing camera (2.70 ns and later).

The mean neutron production time (bang time), as recorded by the neutron temporal diagnostic,²² occurred at 2.43 ns during the time interval when x-ray emission from the core is evident. The areal density averaged over the time of fusion particle production was independently determined by a set of three filtered

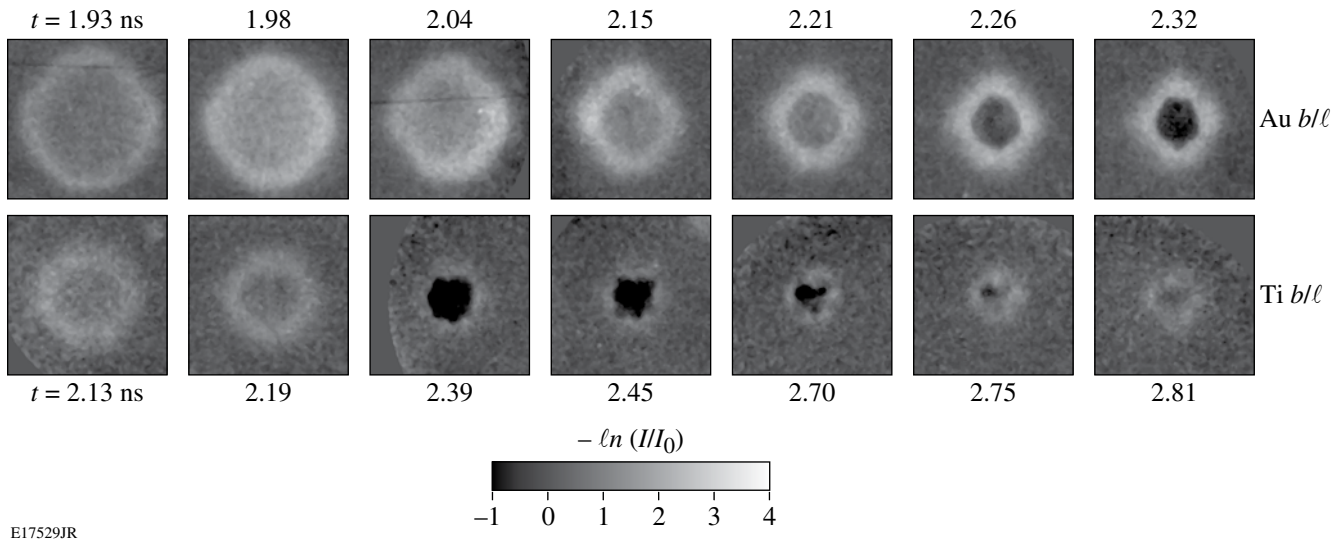


Figure 117.24
Intensity-corrected x-ray radiographs from OMEGA shot 49331 taken with two x-ray framing cameras, one backlit by an Au target and the other by a Ti target. Each image is a $400 \times 400\text{-}\mu\text{m}$ region corrected for backlighter intensity variation as explained in the text.

CR39 packs measuring the slowing down of the $D-^3He$ protons¹ and yields a value of $\langle \rho R \rangle_p = 58 \pm 5 \text{ mg/cm}^2$ (the error is one standard deviation of the three values). The value determined in this case is the sum of the areal densities of the fuel (gas fill) and the shell. An estimate of the fuel areal density ρR_{fuel} is determined from the size of the observed core emission at stagnation ($\sim 50 \text{ }\mu\text{m}$) and mass conservation, yielding $\rho R_{\text{fuel}} = 6 \pm 1 \text{ mg/cm}^2$. The proton inferred shell areal density is therefore $\langle \rho R_{\text{shell}} \rangle_p = 52 \pm 5 \text{ mg/cm}^2$ and is plotted as a single point in Fig. 117.27 at bang time. The value determined from the proton spectra falls closely on the trend of the x-ray measurements, giving additional credence to the results of this method. The *LILAC* simulation of this implosion was performed assuming flux-limited diffusion²³

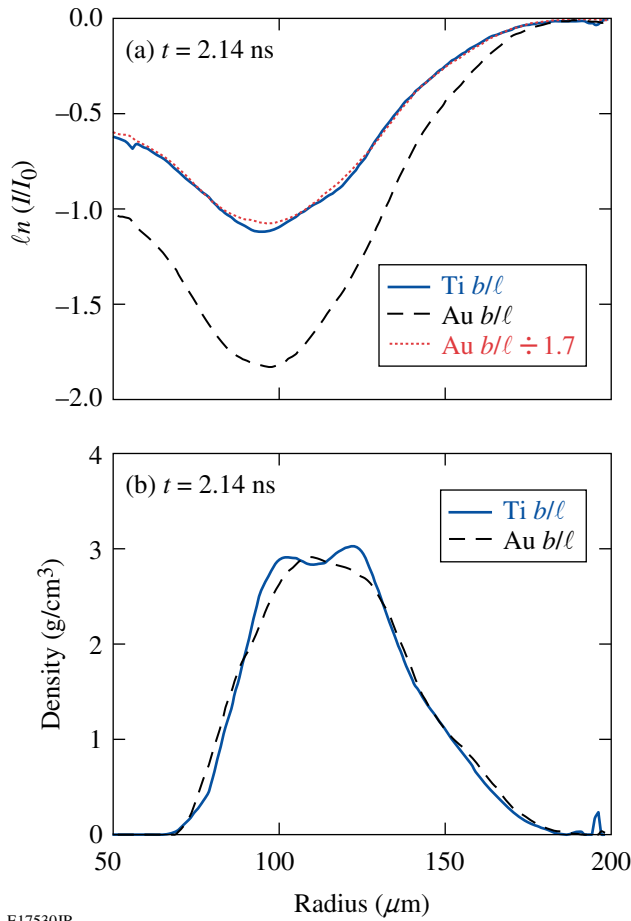


Figure 117.25 (a) The natural logarithm of the intensity variation as a function of projected radial distance in the image plane for a simultaneous pair of Au- and Ti-backlit images. The profiles are azimuthally averaged about the image centers. The dotted line is the Au profile normalized to the Ti profile, demonstrating that they differ only by a multiplicative constant (1.7). (b) The absolute density distributions were computed from the intensity profiles of (a) by Abel inversion with the additional constraint of constant mass as described in the text.

with a flux limiter $f = 0.06$. The predicted areal density is shown as a solid line in Fig. 117.27. The areal density measurements are seen to closely follow this prediction until the time of stagnation, where significant departures from spherical symmetry can be seen in the framed images (Fig. 117.24).

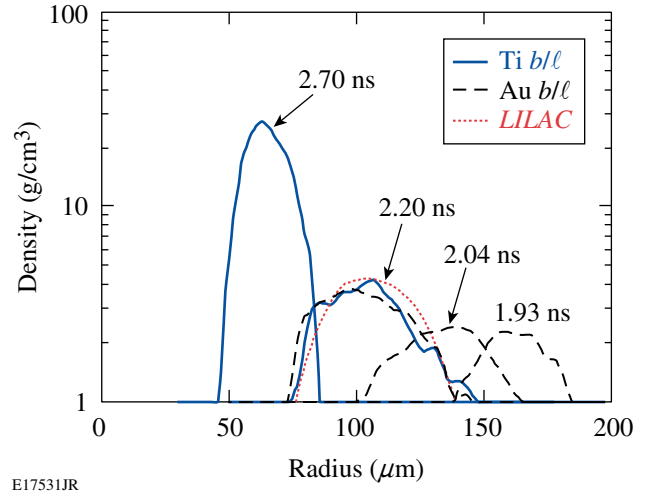


Figure 117.26 Density distributions computed from the x-ray radiographs showing the evolution of the shell density and position as a function of the indicated frame times.

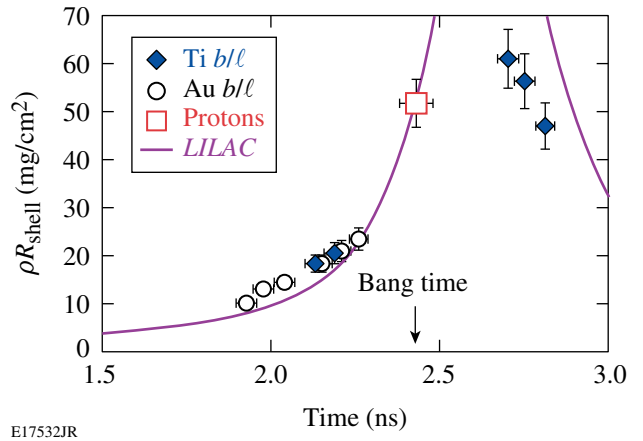


Figure 117.27 The shell areal densities computed from all available x-ray radiographs including those where the emission from the core is just starting (2.3 ns) to the tail end of the core emission (2.6 ns) and later. The value determined from the proton spectra is plotted at the time of peak neutron emission (2.43 ns). The *LILAC*-simulated shell areal density, shown as a solid curve, reached a peak of 110 mg/cm^2 at 2.64 ns (off scale).

This analysis demonstrates that with the application of an area x-ray backlighter, the time history of the shell areal density can be measured on a single implosion experiment from early in the implosion, up to stagnation, and again later in time after core emission has subsided. Such a determination is limited by the temporal extent of the backlighter and the requisite exclusion of target self-emission. A similar measurement of the areal-density time history using proton radiography⁵ requires that the implosion be repeated, acquiring a single time measurement from each of a series of identical implosions. The x-ray radiography technique therefore offers a much less intensive use of the experimental facility, not requiring that the implosion be repeated multiple times to acquire the areal-density time history. The results of this technique support the conclusion that the direct-drive implosion exhibits near 1-D performance, in this case up to the time of core self-emission, with evolving nonuniformities affecting the performance thereafter.

ACKNOWLEDGMENT

This work was supported by the U.S. Department of Energy Office of Inertial Confinement Fusion under Cooperative Agreement No. DE-FC52-08NA28302, the University of Rochester, and the New York State Energy Research and Development Authority. The support of DOE does not constitute an endorsement by DOE of the views expressed in this article.

REFERENCES

1. F. H. Séguin, J. A. Frenje, C. K. Li, D. G. Hicks, S. Kurebayashi, J. R. Rygg, B.-E. Schwartz, R. D. Petrasso, S. Roberts, J. M. Soures, D. D. Meyerhofer, T. C. Sangster, J. P. Knauer, C. Sorce, V. Yu. Glebov, C. Stoeckl, T. W. Phillips, R. J. Leeper, K. Fletcher, and S. Padalino, *Rev. Sci. Instrum.* **74**, 975 (2003).
2. V. A. Smalyuk, P. B. Radha, J. A. Delettrez, V. Yu. Glebov, V. N. Goncharov, D. D. Meyerhofer, S. P. Regan, S. Roberts, T. C. Sangster, J. M. Soures, C. Stoeckl, J. A. Frenje, C. K. Li, R. D. Petrasso, and F. H. Séguin, *Phys. Rev. Lett.* **90**, 135002 (2003).
3. J. A. Frenje, C. K. Li, F. H. Séguin, J. Deciantis, S. Kurebayashi, J. R. Rygg, R. D. Petrasso, J. Delettrez, V. Yu. Glebov, C. Stoeckl, F. J. Marshall, D. D. Meyerhofer, T. C. Sangster, V. A. Smalyuk, and J. M. Soures, *Phys. Plasmas* **11**, 2798 (2003).
4. O. L. Landen *et al.*, *Rev. Sci. Instrum.* **72**, 627 (2001).
5. C. K. Li, F. H. Séguin, J. A. Frenje, M. Manuel, R. D. Petrasso, V. A. Smalyuk, R. Betti, J. Delettrez, J. P. Knauer, F. Marshall, D. D. Meyerhofer, D. Shvarts, C. Stoeckl, W. Theobald, J. R. Rygg, O. L. Landen, R. P. J. Town, P. A. Amendt, C. A. Back, and J. D. Kilkenny, *Plasma Phys. Control. Fusion* **51**, 014003 (2009).
6. T. R. Boehly, D. L. Brown, R. S. Craxton, R. L. Keck, J. P. Knauer, J. H. Kelly, T. J. Kessler, S. A. Kumpan, S. J. Loucks, S. A. Letzring, F. J. Marshall, R. L. McCrory, S. F. B. Morse, W. Seka, J. M. Soures, and C. P. Verdon, *Opt. Commun.* **133**, 495 (1997).
7. C. Stoeckl, J. A. Delettrez, J. H. Kelly, T. J. Kessler, B. E. Kruschwitz, S. J. Loucks, R. L. McCrory, D. D. Meyerhofer, D. N. Maywar, S. F. B. Morse, J. Myatt, A. L. Rigatti, L. J. Waxer, J. D. Zuegel, and R. B. Stephens, *Fusion Sci. Technol.* **49**, 367 (2006).
8. D. H. Kalantar *et al.*, *Rev. Sci. Instrum.* **68**, 814 (1997).
9. F. J. Marshall, R. S. Craxton, M. J. Bonino, R. Epstein, V. Yu. Glebov, D. Jacobs-Perkins, J. P. Knauer, J. A. Marozas, P. W. McKenty, S. G. Noyes, P. B. Radha, W. Seka, S. Skupsky, and V. A. Smalyuk, *J. Phys. IV France* **133**, 153 (2006).
10. R. N. Bracewell, *The Fourier Transform and Its Applications*, 3rd ed. (McGraw-Hill, Boston, 2000), pp. 351–356.
11. H. A. Bethe and E. E. Salpeter, *Quantum Mechanics of One- and Two-Electron Atoms* (Academic Press, New York, 1957), pp. 295–305.
12. F. J. Marshall, J. A. Delettrez, R. Epstein, and B. Yaakobi, *Phys. Rev. E* **49**, 4381 (1994).
13. S. Fujioka *et al.*, *Phys. Plasmas* **10**, 4784 (2003).
14. Ya. B. Zel'dovich and Yu. P. Raizer, in *Physics of Shock Waves and High-Temperature Hydrodynamic Phenomena*, edited by W. D. Hayes and R. F. Probstein (Academic Press, New York, 1966), Chap. V, Vol. I, pp. 269–272.
15. B. Yaakobi, R. Epstein, and F. J. Marshall, *Phys. Rev. A* **44**, 8429 (1991).
16. W. J. Hogan, E. I. Moses, B. E. Warner, M. S. Sorem, and J. M. Soures, *Nucl. Fusion* **41**, 567 (2001).
17. S. Skupsky, R. W. Short, T. Kessler, R. S. Craxton, S. Letzring, and J. M. Soures, *J. Appl. Phys.* **66**, 3456 (1989).
18. T. R. Boehly, V. A. Smalyuk, D. D. Meyerhofer, J. P. Knauer, D. K. Bradley, R. S. Craxton, M. J. Guardalben, S. Skupsky, and T. J. Kessler, *J. Appl. Phys.* **85**, 3444 (1999).
19. J. D. Lindl, *Phys. Plasmas* **2**, 3933 (1995).
20. J. P. Knauer, R. Betti, D. K. Bradley, T. R. Boehly, T. J. B. Collins, V. N. Goncharov, P. W. McKenty, D. D. Meyerhofer, V. A. Smalyuk, C. P. Verdon, S. G. Glendinning, D. H. Kalantar, and R. G. Watt, *Phys. Plasmas* **7**, 338 (2000).
21. J. Delettrez, R. Epstein, M. C. Richardson, P. A. Jaanimagi, and B. L. Henke, *Phys. Rev. A* **36**, 3926 (1987).
22. R. A. Lerche, D. W. Phillion, and G. L. Tietbohl, *Rev. Sci. Instrum.* **66**, 933 (1995).
23. R. C. Malone, R. L. McCrory, and R. L. Morse, *Phys. Rev. Lett.* **34**, 721 (1975).

Integrated Simulations of Implosion, Electron Transport, and Heating for Direct-Drive Fast-Ignition Targets

Introduction

In fast-ignition¹ inertial confinement fusion (ICF), a cryogenic shell of deuterium and tritium (DT) is first imploded by a high-energy driver to produce an assembly of thermonuclear fuel with high densities and areal densities. Such a dense core is then ignited by the fast electrons (or protons) accelerated through the interaction of a high-power, ultra-intense laser pulse with either a coronal plasma or a solid cone-shaped target.^{2,3} The separation of the target compression and ignition stages in fast ignition relaxes the requirements on the symmetry of the implosion and compression energy. By using massive cryogenic targets,⁴ fast ignition has the potential for gains higher than the conventional ICF central hot-spot ignition scheme.

Fast ignition has shown significant promise in successful small-scale integrated experiments² that combine implosions of plastic cone-in-shell targets and heating by subpetawatt laser pulses. The next generation of integrated fast-ignition experiments will use more-massive plastic or cryogenic-DT cone-in-shell targets heated by more-powerful petawatt laser pulses. Such experiments have started at LLE and are planned at other facilities, such as ILE (Osaka University), NIF (LLNL), and the HiPER project. The success of those experiments depends crucially on the understanding of fast-ignition physics and its careful modeling using the best-available numerical codes. The rich physics of fast ignition includes processes having very different temporal and spatial scales, which must be studied using different types of codes. Target implosions are simulated using hydrocodes. Generation of hot electrons by a petawatt laser pulse is simulated using particle-in-cell (PIC) codes. Transport of hot electrons to the dense core is simulated using hybrid-PIC, Monte Carlo, or Fokker–Plank codes. Ignition and burn require simulations of fusion reactions, α -particle transport, and target hydrodynamics, which are done using hydrocodes.

At LLE a comprehensive theory and simulation program is being pursued to explore the physics of fast ignition. High-gain fast-ignition targets have been developed based on hydrody-

amic simulations of implosion,⁴ and performance of those targets has been investigated using hydrodynamic and hybrid simulations.^{5,6} The capabilities of the radiation-hydrodynamic code *DRACO*,⁷ developed at LLE to study the implosion physics, have been recently extended to simulate cone-in-shell targets.⁸ *DRACO* has also been recently integrated with the hybrid-PIC code *LSP*⁹ to simulate the hot-electron transport, target heating, and ignition.⁶

This article reports the latest results from integrated simulations of implosion, hot-electron transport, and heating, for direct-drive, cone-in-shell surrogate plastic targets used in the integrated fast-ignition experiments at LLE, performed using *DRACO* and *LSP*. *LSP* simulations of planar plastic targets are also presented. An important effect found in the simulations is the collimation of hot electrons by the self-generated resistive magnetic field. This effect appears to be highly beneficial for fast ignition because hot electrons are generated in the petawatt laser interaction with a solid-density plasma of the cone tip with an inevitable angular spread.^{10,11} In the absence of collimation there is little hope to deliver the energy by hot electrons into a small volume of the target core with a radius of about 20 μm , located tens or even hundreds of μm away from the cone tip.^{5,12,13} Magnetic collimation of hot electrons increases their coupling with the core and thus decreases the minimum energy required for ignition.

The following sections describe (1) *DRACO* and *LSP*, the two codes used in the simulations; (2) *LSP* simulations of hot-electron transport in solid-density and compressed plastic targets, providing a connection between the recent solid-target experiments and near-future integrated fast-ignition experiments using imploded plastic shells; and (3) the results from integrated simulations of realistic cone-in-shell plastic (CD) targets used in the integrated fast-ignition experiments at LLE, predicting target heating by hot electrons and neutron yields from deuterium–deuterium (D–D) nuclear reactions. The last section summarizes conclusions.

DRACO, LSP, and Integrated DRACO–LSP Simulation Toolkit

*DRACO*⁷ is a two-dimensional (2-D) axisymmetric radiation-hydrodynamic code developed at LLE. It includes the physics required to simulate implosion, ignition, and burn of direct-drive ICF targets. It includes radiation transport and uses realistic equations of state. *LSP*⁹ (large-scale plasma) is a 2-D/3-D (three-dimensional) implicit hybrid-PIC code. It uses an implicit solution for the electromagnetic fields and an implicit particle push, hybrid fluid-kinetic description for plasma electrons with dynamic reallocation, intra- and interspecies collisions based on Spitzer rates, and an ideal-gas equation of state. The hybrid fluid-kinetic description for plasma electrons is especially suited for modeling the hot-electron transport in the fast-ignition scheme. Fluid species can be used for background plasma electrons (and ions) while kinetic species are required to describe energetic electrons. The temperature equation solved for fluid species provides good energy conservation in the modeling of plasma heating by hot electrons. An implicit algorithm in *LSP* provides numerical stability even for very dense plasmas, when the numerical time step greatly exceeds the period of plasma oscillations (high-frequency phenomena, however, are not resolved).

The collisional model in *LSP* was modified to include relativistic and high-density plasma effects and extensively tested to reproduce the correct ranges, blooming, and straggling of hot electrons, as predicted by Refs. 14 and 15. The collisional model uses new recalculated transport scattering coefficients for hot electrons, obtained using the relativistic Rutherford-scattering cross section.¹⁶ The transport coefficients for hot electrons are also modified to account for the electron energy loss caused by incoherent excitation of plasma waves.¹⁴ The fluid electron–ion Spitzer collisional rate is modified to saturate at low electron temperatures to reproduce the appropriate maximum electrical resistivities.¹⁷ For compressed materials, the fluid electron-ion Spitzer collisional rate is saturated below the Fermi-degenerate temperature $[\hbar^2(\pi^2 n_e)^{2/3}/3^{1/3}m_e]$, which can be hundreds of eV for compressed DT or plastic fast-ignition targets. The Coulomb logarithms in the Spitzer rates are modified to include ion strong-coupling and electron-degeneracy corrections as suggested in Ref. 18. Since, in the collisional model in *LSP*, each species is approximated by a single drifting (relativistic) Maxwellian distribution, simulations in this article use separate species for hot electrons in different energy ranges. This ensures that correct scattering and slowing-down rates are used for hot electrons at different energy levels.

The *DRACO* and *LSP* codes have been recently integrated and used to simulate electron transport and ignition for spherically symmetric cryogenic-DT, high-gain, fast-ignition targets.⁶ In the integrated simulations, *LSP* generates the hot-electron source term in the temperature equation for background plasma electrons, solved in *DRACO*. In the simulations of Ref. 6, a self-generated resistive magnetic field was found to collimate the hot electrons and reduce the minimum energy required for ignition, in agreement with Ref. 19. The minimum hot-electron-beam energy of 43 kJ was found to be necessary for ignition using Gaussian electron beams with a mean electron energy of 2 MeV and a divergence half-angle of 20°. Collimation is less effective for electron beams with a larger divergence half-angle.

Simulations of Hot-Electron Transport in Solid-Density and Compressed Plastic Targets

In cone-guided fast ignition, hot electrons are generated by the petawatt laser pulse interacting with the tip of a gold cone about a hundred or more microns away from the dense target core. The transport of hot electrons to the dense core is possible if the beam current of about 1 GA, greatly exceeding the Alfvén limit, is compensated by the return current of plasma electrons. Most present experiments that study the transport of hot electrons in such conditions use solid-density metallic, plastic, or glass targets. The transport properties of hot electrons in those materials can be significantly different than in the compressed hydrogenic plasmas of fast-ignition targets, for instance, due to very different values of the electrical resistivities.

For a 300-g/cm³ plasma, the hot-electron beam energy required for ignition is minimized when the beam radius on target is about 20 μm (Refs. 5, 12, and 13), approximately the minimum size of the laser spot on target. Since hot electrons are generated with an intrinsic angular spread, some collimation mechanism is necessary for the electron-beam radius to remain constant when it reaches the dense core. Collimation of hot electrons was observed in the plastic- and glass-target experiments using relatively low energy laser pulses of a few tens of joules.^{20–22} More recent experiments (see Ref. 10 and references therein) using more-energetic laser pulses up to a few hundred joules and metallic (usually aluminum or copper) or plastic targets did not show collimation, with the divergence angle of hot electrons found to increase with the laser pulse intensity (see, for instance, Fig. 2 of Ref. 10). Hot-electron collimation in the experiments of Refs. 20–22 was explained by the presence of self-generated resistive magnetic fields.^{23,24}

We have performed *LSP* simulations of hot-electron transport in solid-density plastic plasmas ($\rho \approx 1 \text{ g/cm}^3$) containing hydrogen ions H^+ and four-times-ionized carbon ions C^{4+} . The Spitzer plasma resistivity²⁵ was saturated at low temperatures according to $\eta = 1/\sqrt{\eta_{\text{max}}^{-2} + \eta_{\text{Sp}}^{-2}}$, where¹⁷ $\eta_{\text{max}} = 3 \times 10^{-6} \Omega\text{m}$. Figures 117.28–117.30 show the results of 2-D planar geometry simulations performed for three different laser-pulse intensities. The laser pulses are Gaussian in space and in time with a focal-spot diameter of $10 \mu\text{m}$, full width at half maximum (FWHM), and duration of 1 ps. The maximum intensities in the simulations of Figs. 117.28–117.30 are $5 \times 10^{18} \text{ W/cm}^2$, $2 \times 10^{19} \text{ W/cm}^2$, and $6 \times 10^{19} \text{ W/cm}^2$, respectively. The laser wavelength is $\lambda_0 = 1.054 \mu\text{m}$. Hot electrons are promoted from the background of plasma electrons at the left-hand-side plasma boundary, having an exponential energy distribution $[\exp(-E/\langle E \rangle)]$. The mean energy is given by the maximum of the ponderomotive²⁶ and Beg's²⁷ scaling

$$\langle E \rangle [\text{MeV}] = \max \left\{ 0.511 \left[\left(1 + I \lambda_0^2 / 2.8 \times 10^{18} \right)^{1/2} - 1 \right], \right. \\ \left. 0.1 \left(I \lambda_0^2 / 10^{17} \right)^{1/3} \right\},$$

where I is the local instantaneous value of the laser intensity in W/cm^2 and λ_0 is in μm . The energy-conversion efficiency to hot electrons is given by²⁸

$$\eta_h = 1.75 \times 10^{-6} I^{0.2661}.$$

Hot electrons are injected in the plane of simulation at a random angle toward the beam axis, having a Gaussian distribution and a mean half-angle of 30° , half width at half maximum (HWHM). (Such a divergence half-angle is consistent with recent particle-in-cell simulations of hot-electron generation by a petawatt laser pulse.^{10,11})

Snapshots of the hot-electron-beam density and magnetic field 700 fs after the peak of the laser pulse are shown in Figs. 117.28–117.30. It is seen that the hot-electron beam is sufficiently well collimated by the self-generated resistive magnetic field in the simulation of Fig. 117.28, while it is only partially collimated in the simulations of Figs. 117.29 and 117.30. The resistive filamentation²⁹ of electron beams is also observed in the simulations. Figures 117.31(a)–117.31(c) show the results of similar simulations in which the laser-spot diameter was increased to $20 \mu\text{m}$. Figure 117.31 shows a similar trend as

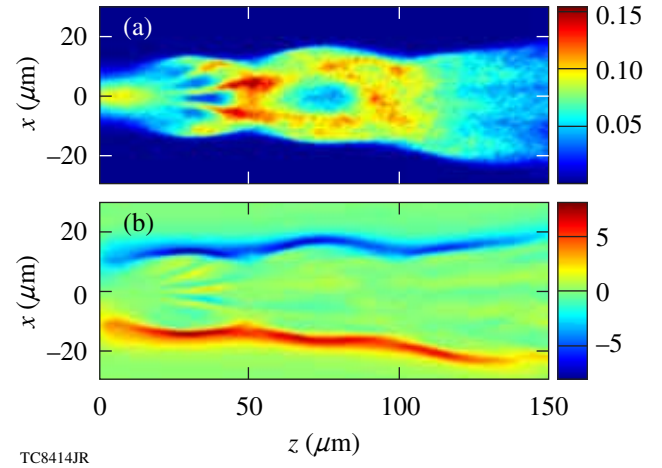


Figure 117.28

(a) Hot-electron density (in $\text{cm}^{-3} \times 10^{21}$) and (b) B_y component of magnetic field (in MG) 700 fs after the peak of the laser pulse in the simulation for a solid-density plastic target, and a laser pulse with a focal-spot diameter of $10 \mu\text{m}$ and a maximum intensity of $5 \times 10^{18} \text{ W/cm}^2$.

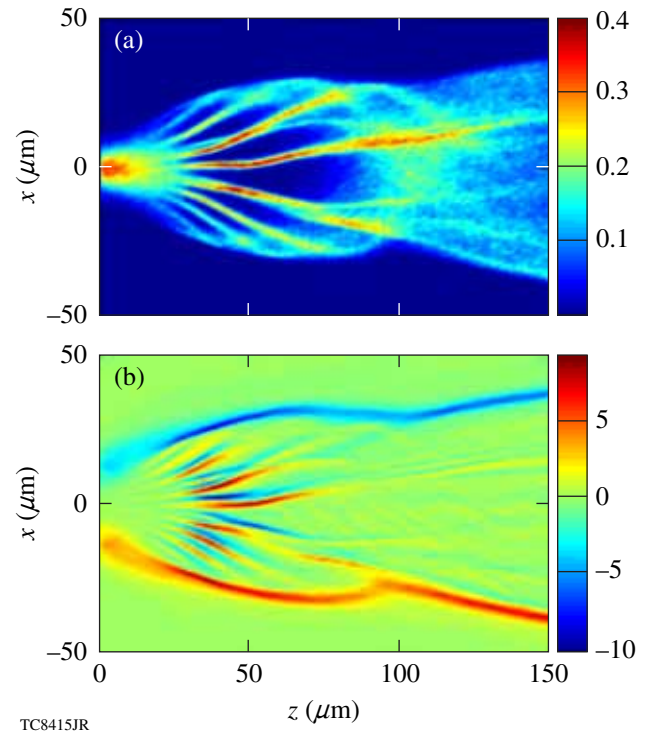


Figure 117.29

(a) Hot-electron density (in $\text{cm}^{-3} \times 10^{21}$) and (b) B_y component of magnetic field (in MG) 700 fs after the peak of the laser pulse in the simulation for a solid-density plastic target, and a laser pulse with a focal-spot diameter of $10 \mu\text{m}$ and a maximum intensity of $2 \times 10^{19} \text{ W/cm}^2$.

Figs. 117.28–117.30—the electron collimation decreases when the laser intensity is increased. The same trend was observed in the solid-target electron-transport experiments. Electron collimation seems to be slightly weaker in the simulations with a larger spot size (Fig. 117.31), but the main dependence is on the laser intensity, in agreement with Ref. 10. Notice that more-sophisticated three-dimensional simulations are required for a better quantitative agreement of the electron-divergence half-angle in the experiments and simulations. The intensity dependence of the initial electron-divergence half-angle in the target, details of the resistivities for different target materials, and the ionization energy loss should also be accounted for. Such 3-D simulations are in progress.

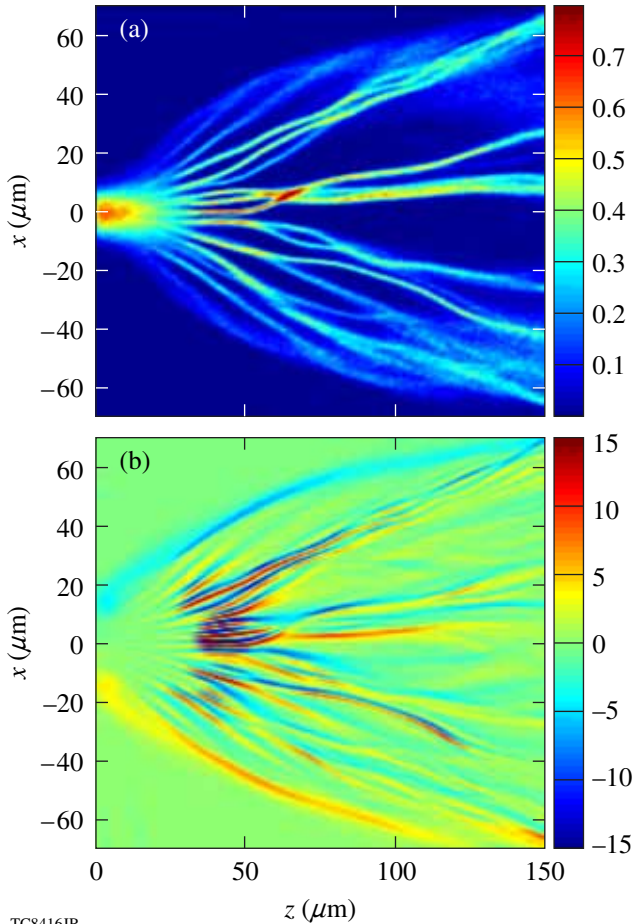


Figure 117.30
(a) Hot-electron density (in $\text{cm}^{-3} \times 10^{21}$) and (b) B_y component of magnetic field (in MG) 700 fs after the peak of the laser pulse in the simulation for a solid-density plastic target, and a laser pulse with a focal-spot diameter of $10 \mu\text{m}$ and a maximum intensity of $6 \times 10^{19} \text{ W/cm}^2$

The first integrated fast-ignition experiments on OMEGA will be performed on imploding plastic targets, leading to plasmas with densities exceeding the solid-state value. The simulation of Fig. 117.32 uses a C^{4+}H^+ uniform plasma with a density of $10\times$ the solid density value ρ_{solid} , while in the simulation of Fig. 117.33, a Gaussian density distribution,

$$\rho = 100 \rho_{\text{solid}} \times \exp\left(-\left\{\left[z(\mu\text{m}) - 90\right]^2 + x(\mu\text{m})^2\right\}/42^2\right),$$

is used to mimic the profile of a compressed fast-ignition target. In the simulation of Fig. 117.33 the density grows from ρ_{solid} at

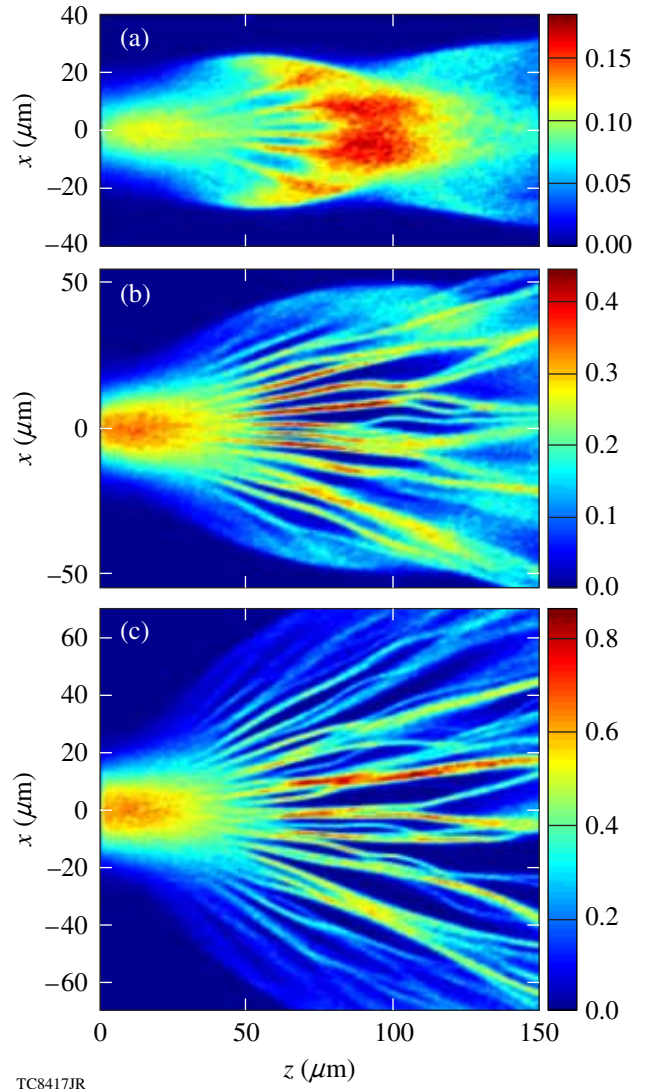


Figure 117.31
Hot-electron density (in $\text{cm}^{-3} \times 10^{21}$) 700 fs after the peak of the laser pulse in the simulations for a solid-density plastic target, and a laser pulse with a focal-spot diameter of $20 \mu\text{m}$ and maximum intensities of (a) $5 \times 10^{18} \text{ W/cm}^2$, (b) $2 \times 10^{19} \text{ W/cm}^2$, and (c) $6 \times 10^{19} \text{ W/cm}^2$.

the left-hand-side plasma boundary where the electron beam enters the plasma to $100 \times \rho_{\text{solid}}$ in the center of the target. The parameters of the laser pulse in both simulations are the same as in the simulation of Fig. 117.31(c): the spot diameter is $20 \mu\text{m}$ and the maximum intensity is $6 \times 10^{19} \text{ W/cm}^2$.

In the simulation of Fig. 117.32 the hot-electron beam is well collimated over a length of $150 \mu\text{m}$. The beam is also collimated in the simulation of Fig. 117.33, where it reaches the dense core and deposits its energy through collisions with plasma electrons and ions. The collimation is due to the generation of a large magnetic field on the electron-beam surface. These simulations show that magnetic collimation is effective at high laser intensities when the plasma is compressed above solid density as expected in fast-ignition targets.

Theoretical models of resistive collimation and filamentation were developed by Davies *et al.*²³ and Bell *et al.*²⁴ (collimation) and Gremillet *et al.*²⁹ (filamentation). The first estimate of the magnetic-field generation in fast-ignition plasmas was reported by Glinsky.³⁰ As the electron beam enters the plasma, it sets up an electrostatic and inductive ohmic electric field that opposes the hot-electron motion and drives a return current of background cold electrons,

$$\mathbf{E} = \eta \mathbf{j}_p \approx -\eta \mathbf{j}_h, \quad (1)$$

where \mathbf{j}_p and \mathbf{j}_h are the cold- and hot-electron current densities, respectively. Initially the two oppositely directed currents cancel each other and the magnetic field is absent. The resistive magnetic field grows in time according to Faraday's law,

$$\frac{\partial \mathbf{B}}{\partial t} = -c \nabla \times \mathbf{E}. \quad (2)$$

The net current density also grows according to Ampere's law $\mathbf{j} \approx (c/4\pi) \nabla \times \mathbf{B}$. The magnetic field of the beam pinches and collimates the hot electrons. A similar process occurs on local peaks of the current density leading to resistive filamentation. Since the plasma resistivity is a function of the electron temperature, the resistivity decreases as the plasma is heated by hot electrons. At sufficiently high temperatures, the electrical resistivity follows Spitzer's formula²⁵

$$\eta = 10^{-2} Z f(Z) \ln \Lambda T_e^{-3/2} \Omega \times \text{cm}, \quad (3)$$

where Z is the ion charge state, $\ln \Lambda$ is the Coulomb logarithm, T_e is the electron temperature in eV, and $f(Z)$ changes from 0.52 to 0.3 when Z increases from 1 to infinity. The main heating mechanism for the background plasma is joule heating,

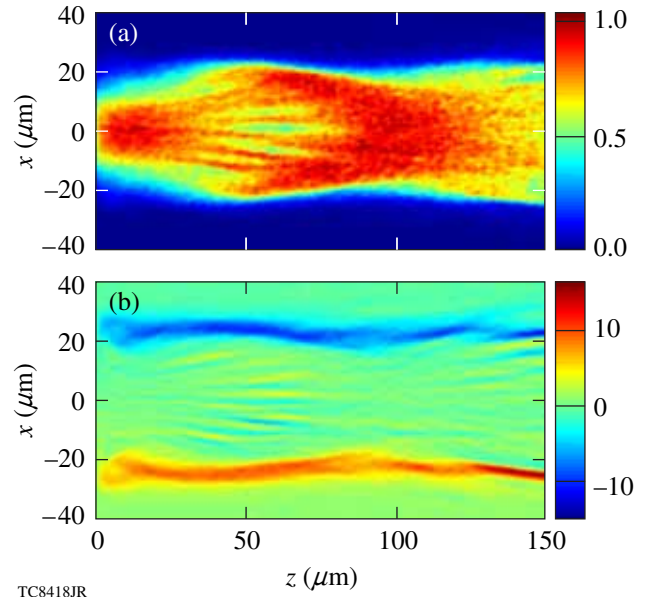


Figure 117.32 (a) Hot-electron density (in $\text{cm}^{-3} \times 10^{21}$) and (b) magnetic field (in MG) 700 fs after the peak of the laser pulse in the simulation for a compressed uniform plastic target and a laser pulse with a focal-spot diameter of $20 \mu\text{m}$ and a maximum intensity of $6 \times 10^{19} \text{ W/cm}^2$.

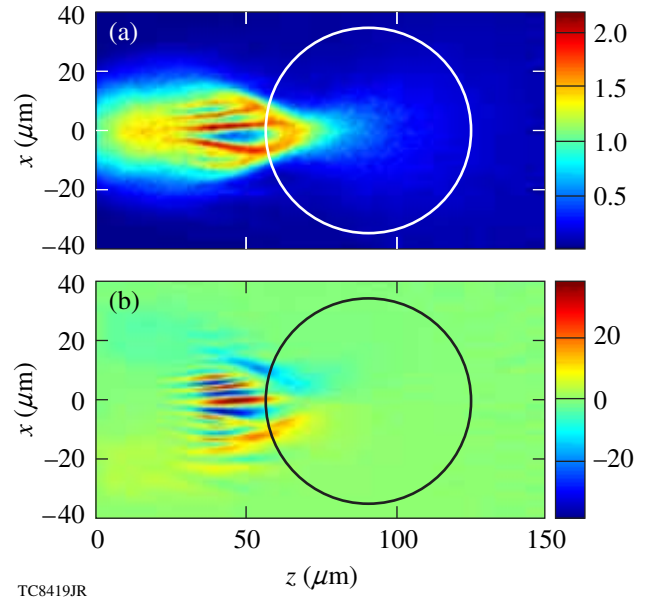


Figure 117.33 (a) Hot-electron density (in $\text{cm}^{-3} \times 10^{21}$) and (b) magnetic field (in MG) 700 fs after the peak of the laser pulse in the simulation for a compressed plastic target with a Gaussian spatial density distribution, and a laser pulse with a focal-spot diameter of $20 \mu\text{m}$ and a maximum intensity of $6 \times 10^{19} \text{ W/cm}^2$.

$$\frac{\partial T_e}{\partial t} = \frac{\eta j_p^2}{C}, \quad (4)$$

where $C = (3/2)n_e$ is the specific-heat capacity of an ideal electron gas and n_e is the electron density. Hot-electron collisions with cold plasma electrons become a dominant heating mechanism close to the dense core of the fast-ignition target (also suggested in Refs. 31 and 32). Plasma heating slows down the growth of the magnetic field and reduces the filamentation instability growth rate.

Magnetic collimation is not effective in the simulations of Figs. 117.29, 117.30, and 117.31(b)–117.31(c) because the plasma is heated too fast and the collimating magnetic field does not have enough time to grow before the resistivity decreases because of the high plasma temperature. On the other hand, in the simulations of Figs. 117.28 and 117.31(a), a strong magnetic field is generated as the plasma is heated slowly by the lower-intensity electron beam, thus keeping the resistivity low enough and allowing the field to grow. The mean energy of hot electrons in the simulations with a lower intensity is also smaller, according to the ponderomotive scaling²⁶—a fact that facilitates the beam collimation. In the simulations of Figs. 117.32 and 117.33, the electron density is higher and the heating time is longer [see Eq. (4)]. Thus the collimating magnetic field has enough time to grow to a large enough strength to collimate high-energy electron beams. The resistive collimation of hot electrons can be induced more effectively if the laser pulse and the corresponding electron beam have a long rising front. In this case, a stronger collimating magnetic field can be generated during the rising pulse front, thus improving the collimation of the main beam.

In the next sections, the results of integrated *DRACO*–*LSP* simulations of cone-in-shell fast-ignition targets are presented. It is important to notice that many features of the electron-beam transport are similar to those obtained in the simplified simulations described in this section.

Integrated Simulations of Cone-in-Shell Plastic Targets for the Fast-Ignition Experiments at LLE

Integrated experiments on OMEGA using low-adiabat implosions of cone-in-shell plastic targets and petawatt heating pulses have begun at LLE. The targets are 40- μm -thick empty CD shells of ~ 870 - μm outer diameter [Fig. 117.34(a)]. A hollow gold cone with an opening angle of 35° or 70° is inserted through a hole in the shell. The cone has a thickness of $10\ \mu\text{m}$ inside the shell and ends in a 15 - μm -thick flat tip, as shown in Fig. 117.34(b). The shell is compressed using a

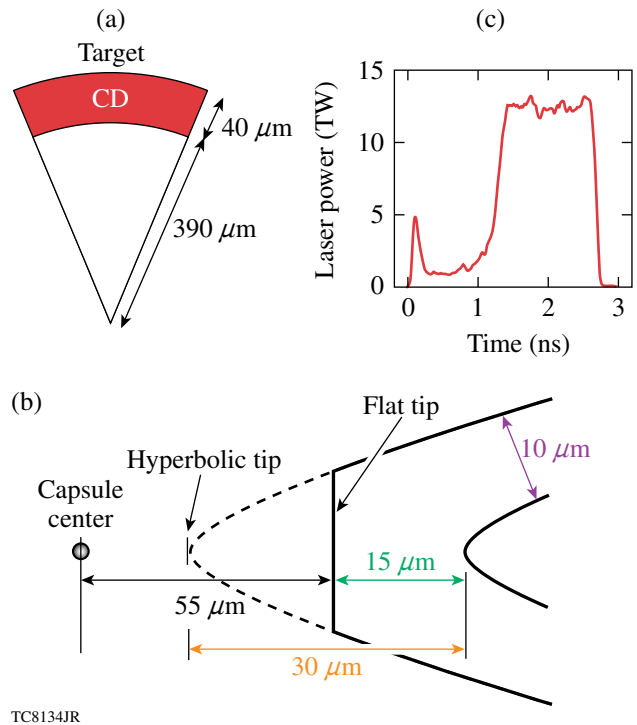
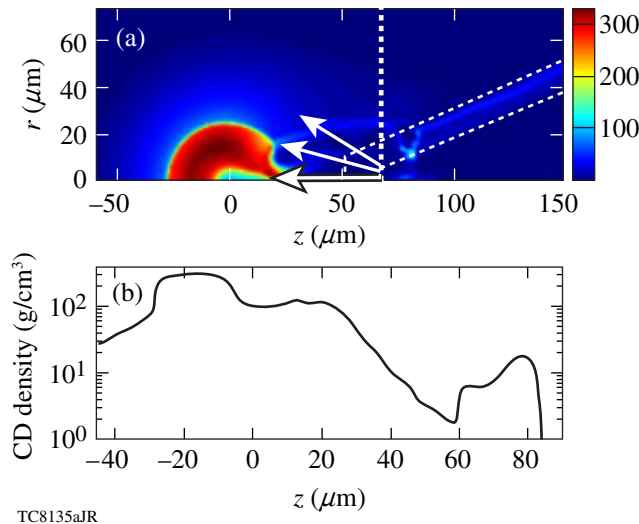


Figure 117.34

Fuel assembly in the integrated simulations for a cone-in-shell plastic target used in the fast-ignition experiments at LLE. Schematics of (a) a plastic shell and (b) a cone tip; (c) temporal profile of the laser pulse used for the target implosion.

351-nm-wavelength, highly shaped pulse of ~ 3 -ns duration and ~ 20 -kJ energy [Fig. 117.34(c)] designed to achieve high areal densities.³³ Previous implosion experiments using similar targets but without the OMEGA EP heating beam,³⁴ measured a neutron yield from D–D nuclear reactions of $(2\text{ to }3) \times 10^7$. The OMEGA EP petawatt laser delivers laser pulses with a 1.054 - μm wavelength, energy up to 2.6 kJ, and a duration of about 10 ps.

We have carried out a set of integrated *DRACO*–*LSP* simulations of target heating for the OMEGA fast-ignition experiments. The simulations were performed for a 50° cone target. In the integrated simulations, *DRACO* was used to simulate the implosion of the plastic cone-in-shell target. *DRACO* and *LSP* were then integrated to simulate the target heating. Because of numerical difficulties related to the cone's gold opacities, the radiation transport was turned off in the *DRACO* simulations. Figure 117.35(a) shows the target density obtained in a *DRACO* simulation at $t = 3.54$ ns, close to the time of maximum areal density $\rho R \sim 0.8\ \text{g/cm}^2$ (in the direction opposite to the cone). Figure 117.35(b) shows the density lineout through the z axis. The density in the compressed shell at this time was around $300\ \text{g/cm}^3$. The initial position of the cone is shown by the white



TC8135aJR

Figure 117.35

(a) Target-density profile at the time of maximum ρR in the integrated simulations for the fast-ignition experiments at LLE. The dashed lines show the initial position of the cone. Hot electrons are injected in the simulations $70 \mu\text{m}$ from target center. (b) Lineout of CD density through the z axis. The density increase at $z > 60 \mu\text{m}$ is due to compression by a shock reflected from the cone tip.

dashed lines. At $t = 3.54 \text{ ns}$ the cone tip was displaced away from the target center by a jet of high-pressure CD gas escaping through the hole in the compressed shell. Despite the fact that the plastic shell was initially empty, plastic was ablated from the inner shell surface and formed a hot, low-density plasma inside the shell. The cone tip not only shifted at this time but was also crushed, and a plastic/gold plasma filled the interior of the cone. We are currently working on optimizing the cone-in-shell implosions,⁸ by varying the cone-tip thickness and distance from the target center, to preserve the integrity of the cone tip at the time of maximum ρR . Here we focus solely on the hot-electron transport in the plastic plasma outside the cone tip. We assume that it is possible to optimize the cone-in-shell implosion and that the hot electrons penetrating through the cone tip reach the plastic plasma. These assumptions will be verified in future integrated simulations.

In the present simulations hot electrons were injected at the time of maximum ρR in the plastic plasma located past the cone tip, $70 \mu\text{m}$ away from the target center. The plastic plasma was assumed to be fully ionized in the simulations described in this section. The hot-electron beam had a square profile in time with a duration of 10 ps and a Gaussian radial profile with FWHM of $20 \mu\text{m}$. We assume that the beam was generated by an OMEGA EP laser pulse with a similar profile, an energy of 2.6 kJ , on-axis intensity of $5.4 \times 10^{19} \text{ W/cm}^2$, and energy conversion efficiency to hot electrons of 30% . For a given

energy, the pulse intensity in the experiment can be varied by changing the pulse duration. According to the ponderomotive scaling,²⁶ the mean energy of hot electrons also changes. In the simulations hot electrons were generated with a relativistic Maxwellian energy-distribution function, and the mean energy was varied from 1.2 to 2.4 MeV to account for the intensity changes. The angular spread of hot electrons from the cone tip was estimated based on previous experimental results. Hot-electron divergence of about 20° (half-angle) has been reported in earlier cone-target experiments.^{2,35} Hot-electron divergence could increase with an increasing thickness of the cone tip because of a strong electron scattering in the gold. The initial divergence was taken as a free parameter in the simulations and varied from 20° to 60° (HWHM, half-angle).

Figure 117.36 shows snapshots of the (a) plasma density, (b) electron-beam density, and (c) azimuthal magnetic field 6 ps after the beginning of the hot-electron beam in the simulation with a mean electron energy of 2 MeV and angular divergence of 20° (half-angle). Figure 117.36(d) shows the temperature of the plasma before the electron beam arrives and Fig. 117.36(e) shows the plasma temperature increase caused by the heating by hot electrons. Figure 117.36(b) shows that the electron beam is well collimated by the self-generated resistive magnetic field. Interestingly, the hot electrons at the axis are somewhat deflected in the $+r$ direction when they approach the core. This is due to the magnetic field (having a negative sign) generated in the hot gas escaping from the center of the target through the hole in the compressed shell. Indeed, the Spitzer plasma resistivity [Eq. (3)] is a decreasing function of temperature. According to Eqs. (1) and (2), in the region of a nonuniform resistivity, a magnetic field of such a sign is generated, deflecting the hot electrons to the region of a higher resistivity. The hot electrons are deflected from the low-density hot-gas region to the dense core, increasing the coupling of hot electrons with the core in the experiment.

Figure 117.36(e) shows that the maximum temperature increase due to hot electrons is about 2.5 keV . It is achieved, however, in the low-density part of the plasma [see the plasma density contours in Fig. 117.36(e)]. The maximum temperature increase in the dense core is about 1 keV in the right-hand side of the core.

Figure 117.37 shows the (a) electron-beam density and (b) azimuthal magnetic field 6 ps after the beginning of the hot-electron beam propagation. In this simulation the electron-beam divergence was increased to 60° (half-angle). The plasma temperature increase due to hot electrons is shown in

Fig. 117.37(c). Even for such a large angular divergence, a large fraction of hot electrons were still collimated by the resistive magnetic field and reached the dense core. (See also Fig. 117.39 showing the hot-electron-density lineouts near the dense core in the simulations of Figs. 117.36–117.38.) Some electrons, however, escape in the radial direction. The temperature increase in the dense core is about 500 eV maximum.

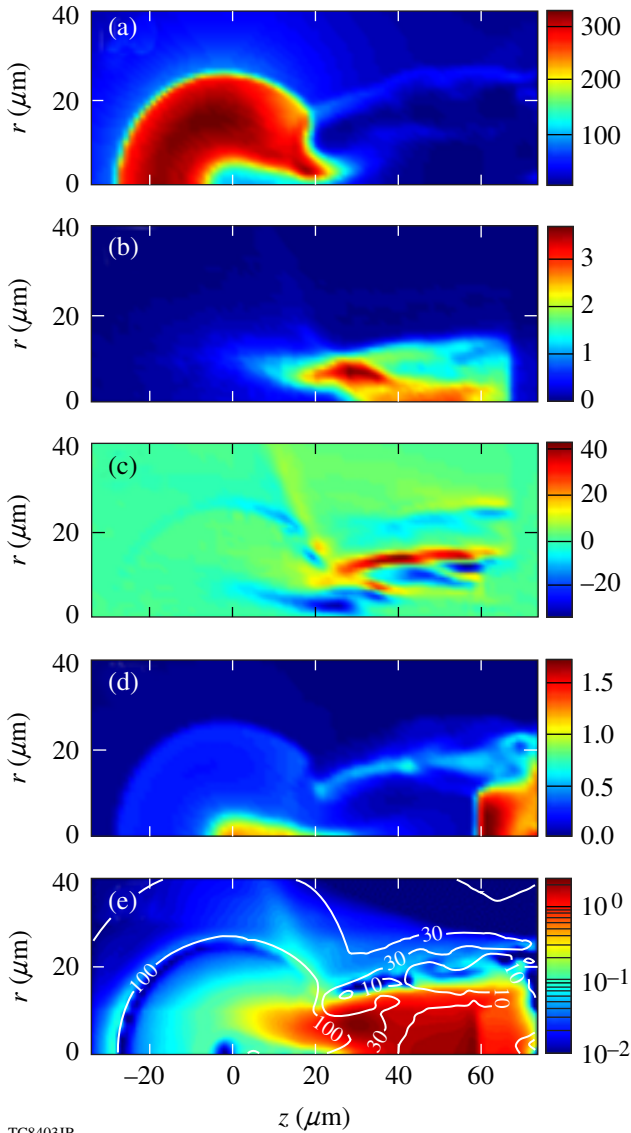


Figure 117.36
 (a) Plasma density (in g/cm^3), (b) hot-electron density (in $\text{cm}^{-3} \times 10^{21}$), and (c) azimuthal magnetic field (in MG) 6 ps after the beginning of the hot-electron beam with an initial divergence of 20° (half-angle). (d) Plasma temperature (in keV) before the electron-beam injection. (e) Ion-temperature increase (in keV) in the end of the hot-electron pulse; plasma density in g/cm^3 contours (white curves) are also shown.

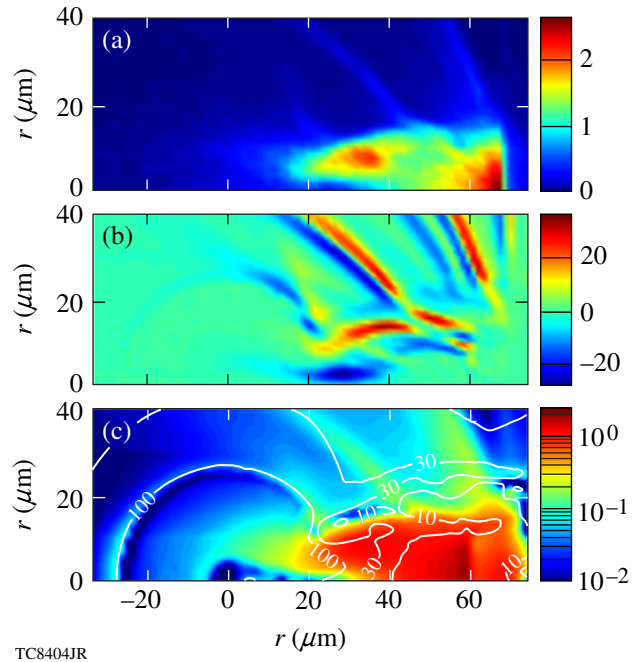
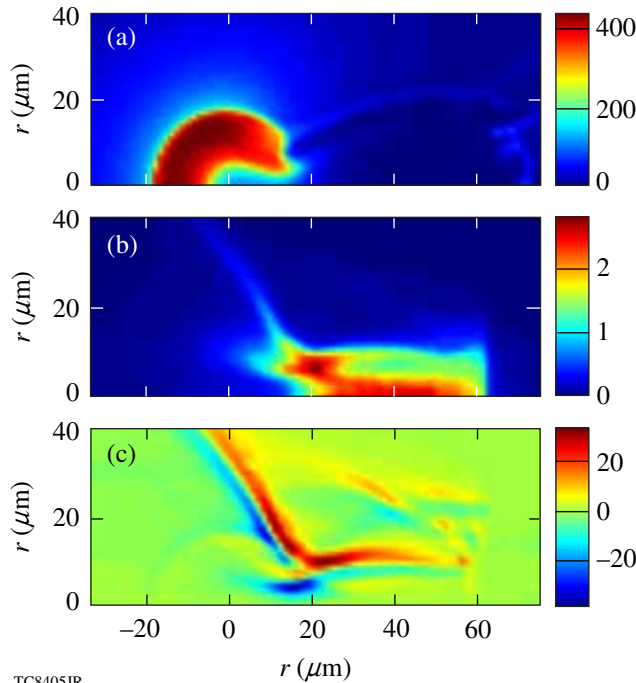


Figure 117.37
 (a) Hot-electron density (in $\text{cm}^{-3} \times 10^{21}$) and (b) azimuthal magnetic field (in MG) 6 ps after the beginning of the hot-electron beam with an initial divergence of 60° (half-angle). (c) Ion-temperature increase (in keV) in the end of the hot-electron pulse; plasma density in g/cm^3 contours (white curves) are also shown.

Figure 117.38 shows the results of a simulation in which the electron-beam parameters were kept the same as in the simulation of Fig. 117.36, but the electron beam was injected 60 ps earlier. At this time the core radius is smaller and the maximum density is higher [compare Figs. 117.36(a) and 117.38(a)] because the maximum ρR is reached when the target begins to expand. Figures 117.38(b) and 117.38(c) show that the electron beam was highly deflected by the magnetic field in the escaping hot gas, and many electrons missed the dense core. This happened because a strong defocusing magnetic field was generated and shifted in the $+r$ direction due to a larger opening in the shell at this time. The dense core outer radius was also smaller, so more hot electrons missed the core. If not for this effect, earlier injection of hot electrons could be beneficial since the cone tip's integrity can be preserved before it is crushed by the hot-gas jet from the compressed shell.

Figure 117.40 summarizes the results of our simulations by plotting the fraction of hot-electron-beam energy deposited in the dense core (in the region with density $\rho > 80 \text{ g}/\text{cm}^3$) as a function of the mean electron energy and angular divergence. This fraction is a weak function of the mean electron energy and decreases from about 50% to 25% when the angular divergence is increased from 20° to 60° (half-angle).

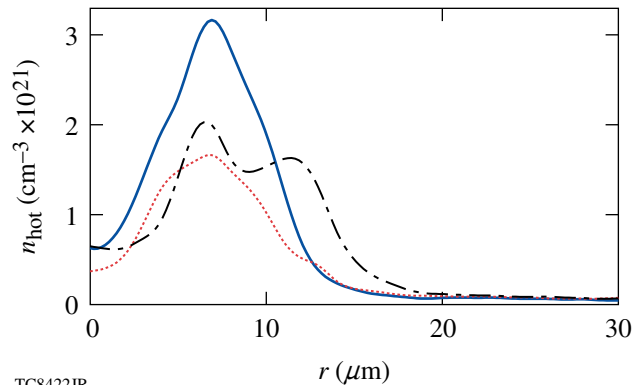
The calculated neutron yield from D–D nuclear reactions was maximum for lower angular divergences. The yield increase caused by the hot-electron-beam heating was about 3×10^9 neutrons for a divergence of 20° (half-angle).



TC8405JR

Figure 117.38

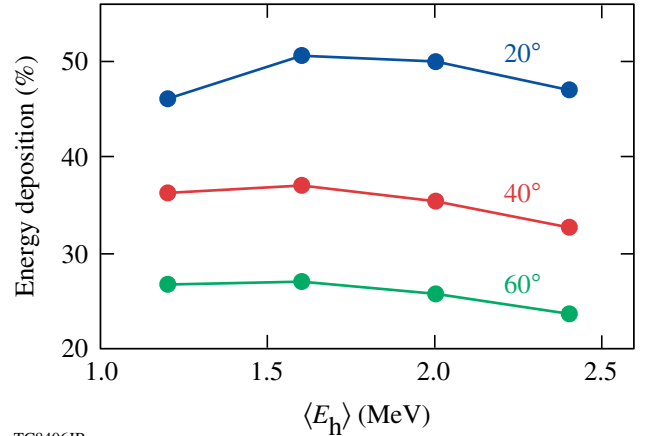
(a) Plasma density (in g/cm^3), (b) hot-electron density (in $\text{cm}^{-3} \times 10^{21}$), and (c) azimuthal magnetic field (in MG) 6 ps after the beginning of the hot-electron beam with an initial divergence of 20° (half-angle), injected 60 ps earlier than in the simulation in Fig. 117.36.



TC8422JR

Figure 117.39

Radial lineouts of the hot-electron density near the dense core: at $z = 25 \mu\text{m}$ in Figs. 117.36(b) (solid line) and 117.37(a) (dotted line), and at $z = 13 \mu\text{m}$ in Fig. 117.38(b) (dashed-dotted line).



TC8406JR

Figure 117.40

Fraction of the electron-beam energy deposited in the dense core (in the region with density $\rho > 80 \text{ g}/\text{cm}^3$).

It is important to mention that more work is necessary to optimize cone-in-shell implosions to preserve the integrity of the cone tip. The transport of hot electrons through the cone tip also must be addressed through dedicated hybrid-PIC simulations. For this purpose *LSP* must be modified to model the ionization of the high- Z cone material, using the quantum equations of state.³⁶ We expect that the angular divergence of the hot electrons will increase due to the enhanced electron scattering in the gold. Tens- to hundreds-of-megagauss resistive magnetic fields are expected in the cone because of the high collisionality of the return current. In such fields, the Alfvén limit can be reached for the filaments or for the entire beam. Magnetic fields can develop at plasma discontinuities (inner cone surface or cone-plasma interface) and cause a surface transport and/or trapping of hot electrons. Finally, an inevitable laser prepulse can create extended regions of pre-plasma inside the cone, increasing the thickness of the high- Z cone material through which the hot electrons propagate.

Conclusion

This article has described the latest results from a set of integrated simulations of the implosion, hot-electron transport, and ignition of direct-drive, fast-ignition cone-in-shell plastic targets, using the hydrodynamic code *DRACO* and the hybrid-PIC code *LSP*. *LSP* simulations of electron transport in solid-density plastic targets have also been presented. These simulations show the importance of self-generated resistive magnetic fields to the transport of hot electrons. *LSP* simulations of solid-density plastic targets show that the effectiveness of magnetic collimation of laser-generated hot electrons decreases with an increase in the laser intensity, in agreement

with solid-target electron-transport experiments. It has also been shown that hot-electron collimation for high-intensity petawatt laser pulses is possible in compressed plastic targets with densities relevant to integrated fast-ignition experiments on OMEGA.

Performance of the cone-in-shell plastic targets developed for integrated fast-ignition experiments at LLE has been investigated using integrated simulations of implosion, hot-electron transport, and target heating. In the present simulations, only the hot-electron transport through the plastic plasma has been investigated. The hot-electron transport through the cone was not simulated. Resistive collimation of hot electrons was found to effectively reduce the hot-electron angular spread and increase the coupling efficiency of hot electrons to the core. Resistive collimation is effective even for electron beams with a large angular spread, up to 60° (half-angle). The coupling efficiency of hot electrons with the target core is about 50% for initial electron divergence of 20° (half-angle), decreasing to 25% for initial divergence of 60° . The integrated simulations predict a neutron-yield enhancement from D–D nuclear reactions of about 10^9 neutrons, which can be easily measured in the experiments. This is significantly more than the implosion neutron yield measured for such targets without a petawatt laser beam.

ACKNOWLEDGMENT

This work was supported by the U.S. Department of Energy under Cooperative Agreement DE-FC02-04ER54789 (Fusion Science Center, Office of Fusion Energy Science) and DE-FC52-08NA28302 (Office of Inertial Confinement Fusion), the University of Rochester, and the New York State Energy Research and Development Authority. The support of DOE does not constitute an endorsement by DOE of the views expressed in this article.

REFERENCES

1. M. Tabak *et al.*, Phys. Plasmas **1**, 1626 (1994).
2. R. Kodama *et al.*, Nature **412**, 798 (2001); R. Kodama *et al.*, Nature **418**, 933 (2002).
3. K. A. Tanaka *et al.*, Phys. Plasmas **10**, 1925 (2003); P. A. Norreys, K. L. Lancaster, C. D. Murphy, H. Habara, S. Karsch, R. J. Clarke, J. Collier, R. Heathcote, C. Hernandez-Gomez, S. Hawkes, D. Neely, M. H. R. Hutchinson, R. G. Evans, M. Borchesi, L. Romagnani, M. Zepf, K. Akli, J. A. King, B. Zhang, R. R. Freeman, A. J. MacKinnon, S. P. Hatchett, P. Patel, R. Snavely, M. H. Key, A. Nikroo, R. Stephens, C. Stoeckl, K. A. Tanaka, T. Norimatsu, Y. Toyama, and R. Kodama, Phys. Plasmas **11**, 2746 (2004).
4. R. Betti and C. Zhou, Phys. Plasmas **12**, 110702 (2005).
5. A. A. Solodov, R. Betti, J. A. Delettrez, and C. D. Zhou, Phys. Plasmas **14**, 062701 (2007).
6. A. A. Solodov, K. S. Anderson, R. Betti, V. Gotcheva, J. Myatt, J. A. Delettrez, S. Skupsky, W. Theobald, and C. Stoeckl, Phys. Plasmas **15**, 112702 (2008).
7. P. B. Radha, T. J. B. Collins, J. A. Delettrez, Y. Elbaz, R. Epstein, V. Yu. Glebov, V. N. Goncharov, R. L. Keck, J. P. Knauer, J. A. Marozas, F. J. Marshall, R. L. McCrory, P. W. McKenty, D. D. Meyerhofer, S. P. Regan, T. C. Sangster, W. Seka, D. Shvarts, S. Skupsky, Y. Srebro, and C. Stoeckl, Phys. Plasmas **12**, 056307 (2005).
8. K. S. Anderson, A. A. Solodov, R. Betti, and P. W. McKenty, Bull. Am. Phys. Soc. **53**, 53 (2008).
9. D. R. Welch *et al.*, Phys. Plasmas **13**, 063105 (2006).
10. J. S. Green, V. M. Ovchinnikov, R. G. Evans, K. U. Akli, H. Azechi, F. N. Beg, C. Bellei, R. R. Freeman, H. Habara, R. Heathcote, M. H. Key, J. A. King, K. L. Lancaster, N. C. Lopes, T. Ma, A. J. MacKinnon, K. Markey, A. McPhee, Z. Najmudin, P. Nilson, R. Onofrei, R. Stephens, K. Takeda, K. A. Tanaka, W. Theobald, T. Tanimoto, J. Waugh, L. Van Woerkom, N. C. Woolsey, M. Zepf, J. R. Davies, and P. A. Norreys, Phys. Rev. Lett. **100**, 015003 (2008).
11. J. C. Adam, A. Héron, and G. Laval, Phys. Rev. Lett. **97**, 205006 (2006).
12. S. Atzeni, Phys. Plasmas **6**, 3316 (1999).
13. S. Atzeni, A. Schiavi, and C. Bellei, Phys. Plasmas **14**, 052702 (2007).
14. A. A. Solodov and R. Betti, Phys. Plasmas **15**, 042707 (2008).
15. C. K. Li and R. D. Petrasso, Phys. Rev. E **70**, 067401 (2004); C. K. Li and R. D. Petrasso, Phys. Rev. E **73**, 016402 (2006).
16. E. M. Lifshitz and L. P. Pitaevskifi, *Physical Kinetics*, 1st ed., Course of Theoretical Physics, Vol. 10 (Pergamon Press, Oxford, 1981), Chap. 4.
17. R. R. Freeman *et al.*, Fusion Sci. Technol. **49**, 297 (2006); M. H. Key, Phys. Plasmas **14**, 055502 (2007).
18. Y. T. Lee and R. M. More, Phys. Fluids **27**, 1273 (1984).
19. J. J. Honrubia and J. Meyer-ter-Vehn, J. Phys., Conf. Ser. **112**, 022055 (2008); S. Atzeni *et al.*, Phys. Plasmas **15**, 056311 (2008).
20. M. Tatarakis *et al.*, Phys. Rev. Lett. **81**, 999 (1998).
21. M. Borghesi *et al.*, Phys. Rev. Lett. **83**, 4309 (1999).
22. L. Gremillet *et al.*, Phys. Rev. Lett. **83**, 5015 (1999).
23. J. R. Davies *et al.*, Phys. Rev. E **56**, 7193 (1997).
24. A. R. Bell and R. J. Kingham, Phys. Rev. Lett. **91**, 035003 (2003).
25. L. Spitzer Jr. and R. Härm, Phys. Rev. **89**, 977 (1953); L. Spitzer, *Physics of Fully Ionized Gases*, 2nd rev. ed., Interscience Tracts on Physics and Astronomy (Interscience, New York, 1962).
26. S. C. Wilks and W. L. Kruer, IEEE J. Quantum Electron. **33**, 1954 (1997).
27. F. N. Beg *et al.*, Phys. Plasmas **4**, 447 (1997).

28. R. P. J. Town *et al.*, Nucl. Instrum. Methods Phys. Res. A **544**, **61** (2005).
29. L. Gremillet, G. Bonnaud, and F. Amiranoff, Phys. Plasmas **9**, 941 (2002).
30. M. E. Glinsky, Phys. Plasmas **2**, 2796 (1995).
31. B. Chrisman, Y. Sentoku, and A. J. Kemp, Phys. Plasmas **15**, 056309 (2008).
32. J. J. Honrubia and J. Meyer-ter-Vehn, Nucl. Fusion **46**, L25 (2006).
33. C. D. Zhou, W. Theobald, R. Betti, P. B. Radha, V. A. Smalyuk, D. Shvarts, V. Yu. Glebov, C. Stoeckl, K. S. Anderson, D. D. Meyerhofer, T. C. Sangster, C. K. Li, R. D. Petrasso, J. A. Frenje, and F. H. Séguin, Phys. Rev. Lett. **98**, 025004 (2007).
34. C. Stoeckl, T. R. Boehly, J. A. Delettrez, S. P. Hatchett, J. A. Frenje, V. Yu. Glebov, C. K. Li, J. E. Miller, R. D. Petrasso, F. H. Séguin, V. A. Smalyuk, R. B. Stephens, W. Theobald, B. Yaakobi, and T. C. Sangster, Phys. Plasmas **14**, 112702 (2007).
35. R. B. Stephens *et al.*, Phys. Rev. Lett. **91**, 185001 (2003).
36. R. M. More *et al.*, Phys. Fluids **31**, 3059 (1988).

Shear Stress in Magnetorheological Finishing for Glasses

Introduction

Magnetorheological finishing (MRF) is a sub-aperture polishing tool for fabrication of precision optics. The removal function of MRF is based on a magnetorheological (MR) fluid that consists of magnetic carbonyl iron (CI), non-magnetic polishing abrasives, and water or other non-aqueous carrier fluids and stabilizers. The MR fluid ribbon stiffens in the presence of a magnetic field to form a localized polisher, and spindle-mounted parts are moved through the polishing zone to polish the surface and to correct the figure.^{1,2}

For conventional polishing processes, the material removal rate (MRR, $\Delta h/\Delta t$ where Δh is a representative height of removal averaged over the entire part area) is predicted by the traditional Preston relationship or Preston's equation:³

$$\text{MRR} = C_p P V = C_p \frac{F_n}{A_c} V, \quad (1)$$

where C_p is the Preston coefficient, which includes the effects of the process parameters affecting the interaction between the work piece and the tool (e.g., pH, slurry, type of abrasives, frictional forces, etc.), P is the normal pressure applied (i.e., normal force F_n divided by the contact area A_c between the polishing tool/pad and the substrate being polished), and V is the relative velocity between the part and the tool. The applicability of Preston's equation for material removal in MRF is a subject of study. Shorey⁴ used the spot-taking machine (STM, described in detail on p. 44) to measure drag force on a sapphire part, using a drag force measuring device and aqueous MR fluids consisting of different types and concentrations of CI particles and abrasives. Shorey⁴ found that there is a strong positive linear relationship between the material removal rate for sapphire and the drag force in MRF, predicting a similar result for fused silica (FS), although drag force values under the above conditions were not reported for FS. Shorey also calculated that the normal force acting on a single abrasive particle (within the MR fluid ribbon) and the part is approximately 1×10^{-7} N (Ref. 4). This is several orders of magnitude

smaller than that for conventional polishing, 5 to 200×10^{-3} N (Ref. 5). Shorey concluded that there must be drag force to have removal in MRF.

To address MRF, first Kordonski⁶ and later Shorey⁴ proposed a modified Preston's coefficient $C'_{p,\text{MRF}}(F_n)$ in terms of the normal force F_n by introducing a coefficient of friction (COF, μ), correlating material removal rate for MRF (MRR_{MRF} , identified as $\Delta h/\Delta t$, where Δh is a representative height of removal averaged over the MRF spot area) with drag force. Equation (2) shows this transition as described by Shorey:

$$\begin{aligned} \text{MRR}_{\text{MRF}} &= C'_{p,\text{MRF}}(F_n) \frac{\mu F_n}{A_s} V = C'_{p,\text{MRF}}(F_d) \frac{F_d}{A_s} V \\ &= C'_{p,\text{MRF}}(\tau) \times \tau \times V, \end{aligned} \quad (2)$$

where, for MRF, the normal force F_n is divided by the spot area A_s , instead of A_c [Eq. (1)]. A_s is the projected spot area over which polishing occurs (see **Characterization**, p. 46), i.e., the pressure applied by the hydrodynamic flow of MR fluid at the gap between the part surface and the STM wheel.⁷ $C'_{p,\text{MRF}}(F_d)$ is a modified Preston's coefficient for MRF in terms of drag force. The drag force F_d divided by the spot area A_s equals the shear stress τ . $C'_{p,\text{MRF}}(\tau)$ is a modified Preston's coefficient in terms of shear stress [note that $C'_{p,\text{MRF}}(\tau) = C'_{p,\text{MRF}}(F_d)$]. Equation (2) predicts that material removal in MRF is proportional to the hydrodynamic pressure and shear stress. Although they did not report on shear stress, Shorey⁴ and Shorey *et al.*⁸ indicated that the normal force in MRF is relatively small compared to conventional polishing techniques, and therefore, material removal in MRF is governed by shear stress rather than the hydrostatic pressure. It is also important to note that this is the first time where the modified Preston's coefficient, as suggested by Kordonski⁶ and Shorey,⁴ is associated with respect to either normal force or drag force/shear stress.

DeGroot⁹ incorporated Shorey's⁴ modified Preston equation, specifically the proportionality between material removal

rate and shear stress, in an empirical model for characterizing MRF of optical glasses with nanodiamonds. Using a drag force sensor other than Shorey's,⁴ DeGroot studied six optical glasses: three phosphates and three silicates. DeGroot⁹ and DeGroot *et al.*¹⁰ found that the peak removal rate (assuming a constant contact zone for all materials divided by the spotting time) increased (silicates) or decreased (phosphates) linearly with drag force. Drag force and peak removal rate did not show the same linear correlation across all six optical glasses since "chemistry and glass composition play a significant role in the MRF material removal process, and removal rate cannot be characterized by drag force alone."¹⁰ It is also important to note that because the spot area was assumed to be constant for all glasses, drag force and shear stress were considered to be equivalent (within a constant of proportionality) when discussing the relationship between these two properties and material removal.

Using the same drag force sensor as DeGroot,⁹ Miao *et al.*¹¹ calculated shear stress from MRF drag force measurements for a variety of materials including optical glasses, polycrystalline ceramics, and hard metals and found a positive linear dependence of peak removal rate with shear stress. They did not consider, however, how shear stress is correlated to material properties.

As reviewed above, previous work concentrated only on the contribution of drag force to material removal in MRF. Limited study was carried out on shear stress that is closely related to drag force, but incorporates the MRF spot area A_s . This article reports on the use of a dual force sensor for the real-time, simultaneous measurement of both drag force and normal force in MRF. We study how the measurable normal and drag forces, and calculated shear stress with respect to the measured projected spot area on the part surface, contribute to material removal in MRF for optical glasses based on

their mechanical properties. The variability of the value for the Preston's coefficient in MRF over the three glass types is examined in terms of the normal force, drag force, shear stress, and a material figure of merit. We propose a new modification to the Preston's equation that predicts MRF material removal rate in terms of mechanical properties and shear stress for optical glasses.

The following sections (1) describe materials tested in this work, the STM experimental platform, data acquisition, and methodology used for characterizing experimental results; (2) present MRF spotting results including spot depth, area and volume, removal rate, and force measurement data; (3) discuss the dependence of drag and normal forces on material properties, the role of shear stress in MRF material removal, and the modified Preston's equation; and (4) present conclusions based on this work.

Experimental Details

1. Materials

Three types of optical glasses were chosen for this study based on their economic importance: phosphate (LHG8), borosilicate (BK7), and fused silica (FS). LHG8 is a phosphate laser glass that is widely used in high-peak-power laser systems. It is mechanically soft and has moderate chemical durability. BK7 and FS are optical glasses commonly used for visible and ultraviolet applications because of their excellent chemical, mechanical, and optical properties. The materials' mechanical properties, ranked in order by increasing Vickers hardness, are listed in Table 117.I. The figure of merit (FOM) shown in Table 117.I is defined as $E/K_c H_V^2$, where E is Young's modulus (resistance to elastic deformation), H_V is Vickers hardness (resistance to plastic deformation), and K_c is fracture toughness (resistance to fracture/crack growth). This figure of merit was originally used by Lambropoulos *et al.*¹² to evaluate volumetric removal in loose-abrasive lapping of optical glasses.

Table 117.I: Physical and mechanical properties of optical glasses rank in order by increasing Vickers hardness.^(a)

Material	Mat. ID	Young's Modulus E (GPa)	Vickers Hardness H_V (GPa)	Fracture Toughness ^(b) K_c (MPa \times m ^{1/2})	Figure of Merit ^(c) $E/K_c H_V^2$ ($\times 10^{-3}$ MPa ⁻² \times m ^{-1/2})	Source
Phosphate	LHG8	62	3.7	0.5	8.71	Hoya
Borosilicate	BK7	81	6.0	0.8	2.81	Schott
Fused Silica	FS	69	7.5	0.8	1.64	Corning

^(a)Mechanical properties are from Ref. 9 where glass hardness was measured using a 100-gf load; errors for all values are less than $\pm 25\%$.

^(b)Fracture toughness numbers were calculated using the model of Evans.¹³

^(c)Figures of merit (FOM) were calculated after Lambropoulos *et al.*¹²

The relationship between the FOM and the removal rate in MRF is discussed on p. 47.

Three pieces of each material were used in this work, except LHG8, for which only one piece was available. All substrates were flats, pitch polished in LLE's Optical Fabrication Shop to a surface flatness of less than $1 \mu\text{m}$ for all materials¹⁴ and to a root-mean-square (rms) surface roughness of less than $\sim 2 \text{ nm}$ (Ref. 15). All substrates were round disks ($\sim 40 \text{ mm}$) with thicknesses varying from $\sim 2 \text{ mm}$ to $\sim 10 \text{ mm}$.

2. Spot-Taking Machine

An MRF spot-taking machine (STM, see Fig. 117.41) was used as a test bed to take removal-rate data in the form of spots on part surfaces *without part rotation*. Unlike a commercial MRF machine, the STM has only z -axis motion and cannot be used to polish a surface. The MRF removal function from the STM is characterized with an MRF spot that is created by lowering a nonrotating part into the rotating MR fluid ribbon. Material is removed in a characteristic D-shaped spot, as shown in Fig. 117.42.

The STM operating settings were kept constant for all spots taken in this work. Fluid temperature was held at $\sim 23^\circ\text{C}$. The mixing rate within the fluid confinement vessel was 1000 rpm,

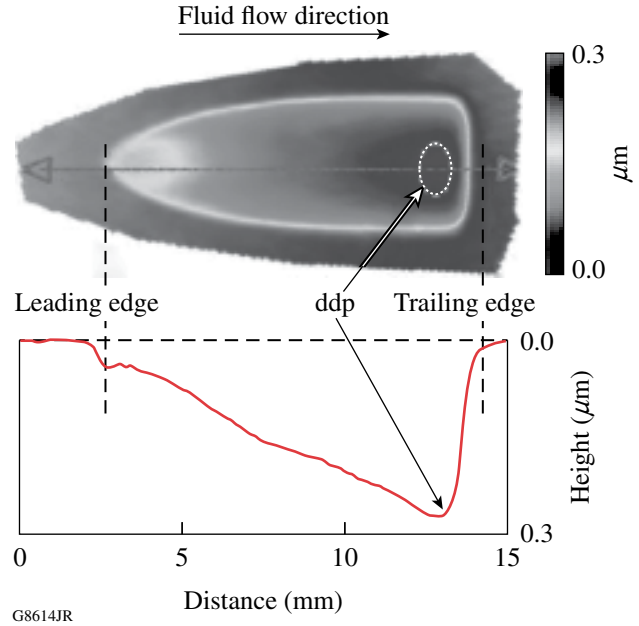


Figure 117.42 Interferometric image of an MRF spot on BK7 glass and its accompanying profile.¹⁴ The dashed ellipse denotes the depth-of-deepest-penetration (ddp) region where a maximum amount of material is removed. Parallel dashed lines indicate the leading edge (where the MRF ribbon starts to contact the part) and the trailing edge (where the MRF fluid ribbon leaves the part). The MR fluid is flowing from left to right. The spot line profile is extracted through the center of the spot image; the distance from the leading edge to the trailing edge is $\sim 12 \text{ mm}$ and the spot depth is $\sim 0.28 \mu\text{m}$.

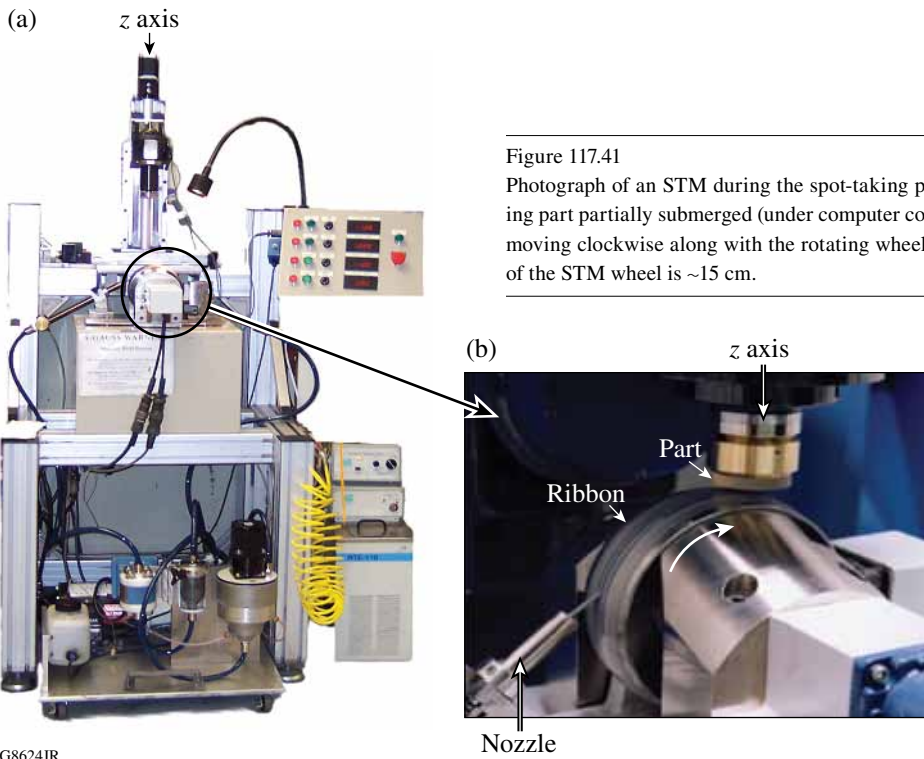


Figure 117.41 Photograph of an STM during the spot-taking process: (a) spot-taking machine; (b) the nonrotating part partially submerged (under computer control) into the stiffened MR fluid ribbon, which is moving clockwise along with the rotating wheel. The STM has only z -axis motion. The diameter of the STM wheel is $\sim 15 \text{ cm}$.

the magnetic pole-piece current was 15 A (resulting in a magnetic field strength of 2 to 3 kG), the wheel speed was 200 rpm, and the out-of-field viscosity was 45 cP, as measured on the STM. The pump speed was adjusted to maintain a ribbon height of 1.6 mm, and the depth of the part immersed into the MR fluid ribbon, precisely controlled by computer, was kept constant at 0.3 mm. Spotting times (i.e., dwell times) varied from 1.17 s to 2.16 s in order to keep spot depths within the measurement range of a laser interferometer (see **Characterization**, p. 46).

A standard aqueous magnetorheological (MR) fluid was used in this experiment. This MR fluid consisted of carbonyl iron (CI) particles, nonmagnetic nanodiamond abrasives, deionized (DI) water, and stabilizers. The CI particles used in the MR fluid had a median particle size of $\sim 4 \mu\text{m}$. A small amount of nanodiamond particles, $\sim 50\text{-nm}$ median size,⁹ were used as polishing abrasives to enhance the material removal efficiency.

3. Dual-Force Sensor/Sample Mounting Device

A mounting device was developed for measuring both drag and normal forces acting on the part surface during MRF spotting, as shown in Fig. 117.43. The device consists of two dynamic piezoelectric force sensors,^{16,17} mounted directly above the MR fluid ribbon and part surface contact zone. This ensures that both the sensors and the part align along the machine's z axis. This configuration limits the spotting experiment to one spot per part, except for LHG8 where only one part was available, requiring a small offset of the part

itself. The sample mount portion of the device was modified to permit this adjustment.

The sensors are suitable for measuring relatively low forces (response threshold less than 0.1 and 0.01 N for the drag and normal force sensors, respectively),^{16,17} which makes it possible to detect subtle changes in substrate type and surface condition, MR fluid composition, and STM machine settings. Special care was taken to keep the part's surface horizontal and perpendicular to the z axis for force measurements during spotting. System noise encountered in previous mounts was overcome by fabricating the force sensor/sample mounting device from aluminum to reduce its overall weight and by installing two 150-Hz filters (hardware) on both dual-mode amplifiers used for data acquisition.

Off-line calibration of the dual-force sensor assembly was performed on each material individually after each part was mounted. The normal-force sensor and drag-force sensor were calibrated separately. The calibration test showed that the vertical load applied for calibrating the normal-force sensor did not introduce a horizontal-force signal in the drag-force sensor, and a horizontal force applied for calibrating the drag-force sensor did not introduce a vertical-force signal in the normal-force sensor.

A LabVIEW interface was designed to record drag- and normal-force signals simultaneously.¹⁸ Force was averaged over the spotting time for each individual measurement.

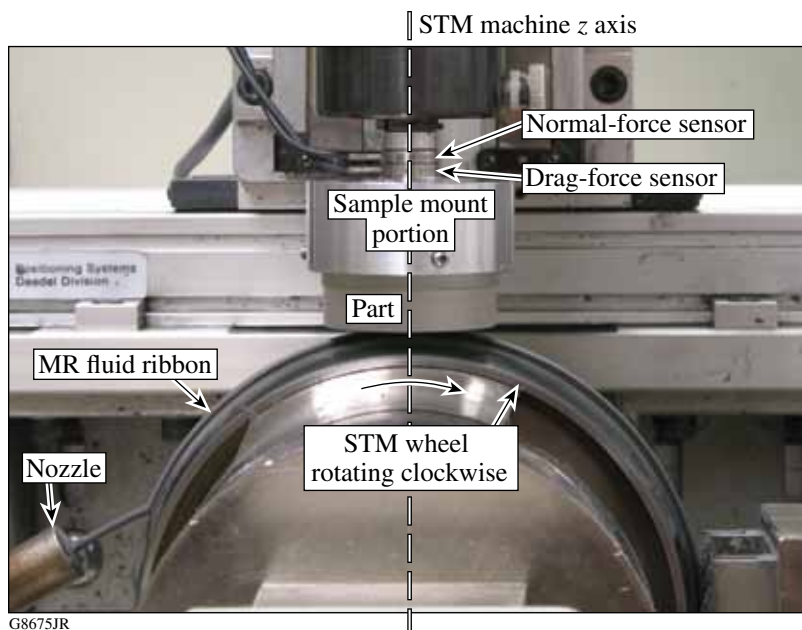


Figure 117.43

Photograph of the dual force sensor/sample mounting device, during spot taking on the STM, indicating the machine's z axis, the normal- and drag-force sensors, the sample mounting device, a part, the MR fluid ribbon, and the rotating wheel (diameter ~ 15 cm). The sensors are located directly above the contact zone between the MR fluid ribbon and the part for real-time *in-situ* measurements. The sample is waxed to a glass disk held by a set of screws against the aluminum housing of the sample mounting device.

4. Characterization

Removal rates for parts were obtained from MRF spots. The initial surface flatness was determined by a Zygo Mark IVxp interferometer (HeNe Fizeau interferometer),¹⁴ which was also used to determine MRF-spot physical properties including spot profile, depth of deepest penetration (ddp), spot area, and spot volume. Spot volume (the volume of material removed in the spot) was measured using the laser interferometer by subtracting the original surface (before spotting) from the new surface that included the spot.¹⁹ Volumetric removal rate was calculated as the spot volume divided by the spotting time. Spot area A_s was obtained by “drawing” a contour line on the spot periphery (light outline seen in the image in Fig. 117.42). Pressure was calculated by dividing normal force by spot area. Shear stress was calculated by dividing drag force by spot area.

It is important to note that in MRF, the contact area A_c and the spot area A_s are not the same. A_c represents the whole area of the part in contact with the MR fluid ribbon, while A_s is where the material removal effectively takes place during MRF spotting. The spot area, within the contact area, is normally slightly smaller, due to the fact that shear stress at the spot edge is almost zero, resulting in negligible material removal. Results from spotting experiments (not described here) demonstrate that A_c is the same for all materials when spotted under the same STM settings; A_s is, however, dependent on material type.

The peak-to-valley (p-v) and root-mean-square (rms) surface roughness within the spot ddp region for all materials was measured with a Zygo NewView 5000 noncontacting

white-light interferometer.¹⁵ Unfiltered areal ($350 \times 260 \mu\text{m}^2$) surface roughness data were acquired at five randomly located sites within the spot ddp region for every spot taken.

Experimental Results

All spotting experiments were conducted under the same STM settings (except for the spotting time described in **Spot-Taking Machine**, p. 44) within a three-day period, approximately ten days after loading the MR fluid into the STM. Table 117.II summarizes the experimental results, including spot ddp, calculated peak removal rate ($\Delta h/\Delta t$), area (projected spot area), volume, calculated volumetric removal rate (VRR), drag force (F_d), normal force (F_n), and p-v and rms surface roughness. The rate of material removal is given in terms of volumetric removal rate. VRR is a practical measure of process efficiency providing a three-dimensional representation of material removal over the whole spot area (notice that the horizontal scale of Fig. 117.42 is in millimeters, whereas the vertical line, i.e., the spot depth, is in micrometers). Surface roughness data entered in Table 117.II for each material are averaged over 15 measurements, taken at five sites within the ddp region of each of three spots.

Drag force (F_d) is between ~ 4 to ~ 5 N, and normal force is between ~ 6 to ~ 9 N. These results fall within the range (2 to 20 N) of normal-force values reported by Schinhaerl *et al.*²⁰ using a three-axis dynamometer and a cerium-oxide MR fluid on BK7 glass over a range of operating conditions. Figure 117.44 plots both normal and drag forces versus the materials' Vickers hardness, where it is seen that only normal force has a positive linear dependence on material hardness.

Table 117.II: Experimental data for materials after spotting.

Material	Spotting time (s)	ddp (μm)	Peak removal rate ($\mu\text{m}/\text{min}$)	Spot area (mm^2)	Spot volume ($\times 10^6 \text{mm}^3$)	Volumetric removal rate (mm^3/min)	F_d (N)	F_n (N)	p-v (nm)	rms (nm)
LHG8	1.17	0.9 ± 0.014	46 ± 0.8	36 ± 2	10.1 ± 0.7	0.517 ± 0.038	4.0 ± 0.0	6.2 ± 0.4	12 ± 2	1.5 ± 0.2
BK7	1.17	0.28 ± 0.001	14 ± 0.1	54 ± 1	5.4 ± 0.2	0.268 ± 0.016	5.1 ± 0.1	8.4 ± 0.2	14 ± 1	1.6 ± 0.3
FS	2.16	0.28 ± 0.016	8 ± 0.4	50 ± 0.1	3.4 ± 0.1	0.102 ± 0.012	4.1 ± 0.1	9.3 ± 0.3	9 ± 1	1.0 ± 0.1

Material	F_d/F_n	F_n/A_s (MPa)	F_d/A_s (MPa)
LH8	0.64 ± 0.04	0.17 ± 0.0157	0.11 ± 0.0001
BK7	0.61 ± 0.01	0.16 ± 0.0052	0.09 ± 0.00126
FS	0.44 ± 0.01	0.19 ± 0.0085	0.08 ± 0.0028

The measured ratio of drag force to normal force (F_d/F_n) falls between ~ 0.4 to ~ 0.6 , which is in the typical range for the coefficient of friction (COF) reported for most materials in the sliding friction mode.²¹ This is the first reported measurement of F_d/F_n for MRF.

The resultant p-v and rms surface roughness after the spotting process is expected since the sample piece is not rotated. These areal rms values of ~ 1 nm are typical of those previously reported for glass spotted on the STM.⁸⁻¹⁰

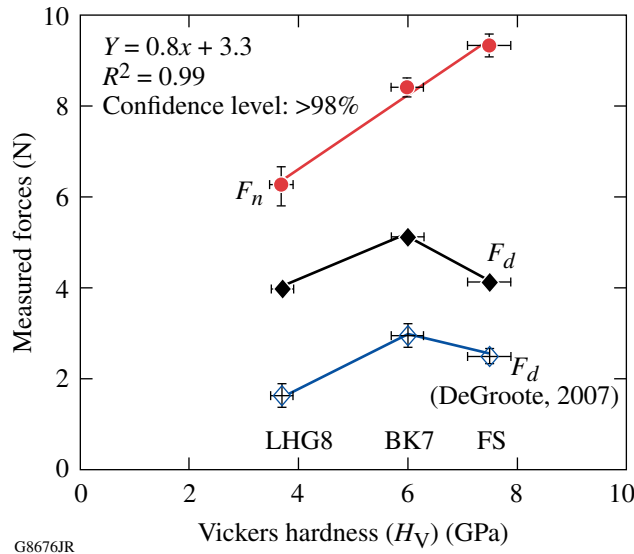


Figure 117.44
Normal force F_n and drag force F_d as a function of the material's Vickers hardness (GPa) for LHG8, BK7, and FS. (See text for a discussion of data taken by DeGrootte.⁹)

Discussion

1. From Normal Force to Hydrodynamic Pressure, from Drag Force to Shear Stress

For the first time, both drag force (F_d) and normal force (F_n) are measured simultaneously *in situ* for MRF. This section discusses how these measured forces correspond to the material removal model presented in the **Introduction** (p. 42) and its validity to MRF.

Normal force shows a positive linear dependence on material type (Fig. 117.44) under the conditions used in this experiment. Broadly speaking, material wear depends on its mechanical hardness, i.e., a soft material will wear more rapidly than a harder one. Our results show that the normal force is sensitive to the substrate surface hardness and, therefore, must have some, as yet undetermined, role to play in the motion/interaction between the MR fluid ribbon and the part.

In addition, the volumetric removal rate decreases as normal force increases, as seen from the data in Table 117.II. However, when an attempt is made to plot and examine (not shown here) the ratio of F_n/A_s , i.e., the hydrodynamic pressure, to material Vickers hardness, no dependence is seen. Likewise, plotting the volumetric removal rate versus the hydrodynamic pressure (not shown here) reveals no dependence. (Note that the calculated hydrodynamic pressure range is from 0.1 to 0.3 MPa. This is comparable to literature values for pressure found in conventional chemical mechanical polishing processes.²²) These results confirm experimentally that hydrodynamic pressure has negligible effect on material removal, and, contrary to previous reports,⁴ the normal force is affected by the material hardness. The next section evaluates the different process parameters that affect the removal rate in MRF.

Figure 117.44 shows that the drag force alone does not depend on material type. This was originally reported by DeGrootte⁹ (see Fig. 117.44) on the STM, using a different force-sensor mounting device that included only a drag-force sensor. The current results are $\sim 100\%$, 20% , and 60% higher for LHG8, BK7, and FS, respectively, compared to those measured previously. This increase in the measured drag force is attributed to improved alignment of the location of the drag-force sensor relative to the STM z axis and different MRF fluid/spotting conditions; otherwise, the results are similar.

It is not clear why drag force does not show an upward or downward trend with material hardness. As suggested by DeGrootte⁹ and DeGrootte *et al.*,¹⁰ the contribution of the glass-surface chemical dissolution to material removal in the MRF process is not explicitly represented by any terms in Eq. (2). The effect of chemistry on lowering the drag force experienced by the phosphate LHG8 could be considerable. A modification of Eq. (2) is offered in the next section, which provides a relatively simple prediction of material removal for MRF from that described by DeGrootte⁹ and DeGrootte *et al.*,¹⁰ without considering chemical contributions in the removal process.

Our results indicate that the hydrodynamic flow pressure in the converging gap, between the workpiece and MR fluid ribbon, depends on the composition of the upper gap surface. If pure no-slip boundary conditions held at the part surface, one would expect both normal and drag (shear) forces to be independent of part composition. We conclude, therefore, that the no-slip boundary condition must be violated to some extent on the part's surface. This is not surprising, given the fact that the MR fluid consists of a high concentration of solid abrasives in an aqueous medium.

Figure 117.45 plots the volumetric removal rate as a function of shear stress, F_d/A_s . It shows a strong dependence between material removal and shear stress, as predicted by Eq. (2), for shear stress values between ~ 0.08 to 0.15 MPa for the three glasses under the specific conditions of this experiment. It can also be extrapolated from these results that, for shear stresses less than about 0.08 MPa, the removal rate practically vanishes. This suggests a shear stress threshold below which material removal is very low; therefore the process efficiency is very low. As seen from Fig. 117.45, the volumetric removal rate does not depend on the hydrodynamic pressure F_n/A_s .

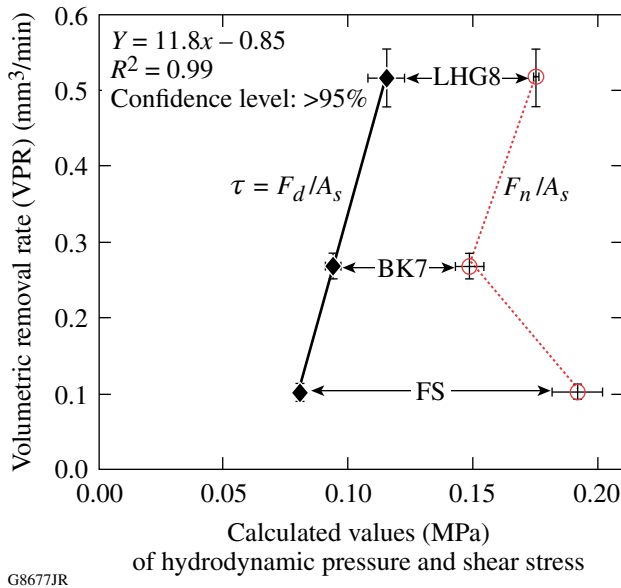


Figure 117.45
Volumetric removal rate (VRR) as a function of shear stress (τ), F_d/A_s , and as a function of the hydrodynamic pressure F_n/A_s .

2. Material Removal Rate Model

Lambropoulos *et al.*²³ found that the material removal rate is linearly proportional to both material mechanical properties (combined into a mechanical FOM) and pressure for loose-abrasive lapping of optical glasses. Their equation is now modified to describe material removal in MRF on the basis of the mechanical contributions to a FOM. Vickers hardness (H_V) is used in this analysis instead of Knoop hardness (H_K). The exponents of the mechanical property components are simplified as $E/K_c H_V^2$ (this term is designated as the mechanical FOM), similar to DeGroot's⁹ and DeGroot *et al.*,¹⁰ where near-surface Young's modulus and nanohardness were used instead of bulk values.

We next discuss the development of a coefficient to describe MRF removal similar to $C'_{p,MRF}(\tau)$ in Eq. (2). To establish such a coefficient, we may use either pressure (as usually done in Preston analysis) or shear stress (as our current work indicates).

The effects of both shear stress (τ) and mechanical properties ($E/K_c H_V^2$) can be incorporated into a predictive equation for material removal as shown in Eq. (3):

$$\text{MRR}_{\text{MRF}} = C'_{p,MRF}(\tau, \text{FOM}) \frac{E}{K_c H_V^2} \times \tau \times V, \quad (3)$$

where $C'_{p,MRF}(\tau)$ is a modification of Preston's coefficient in terms of shear stress τ and the material FOM. MRR_{MRF} could alternatively be written as the ratio $\text{VRR}_{\text{MRF}}/A_s$, which is identified as $\Delta h/\Delta t$, where VRR_{MRF} is the volumetric removal rate for MRF and Δh is a representative height of removal averaged over the whole spot area.

For a linear velocity ~ 1.57 m/s at the wheel edge, assuming that the nanodiamond abrasives and the CI particles in the stiffened MR fluid ribbon are moving at the same speed as the rotating wheel, it is possible to estimate values for each of the three Preston's coefficients identified in Eqs. (2) and (3). Table 117.III shows the calculated values for $C'_{p,MRF}(F_n)$, $C'_{p,MRF}(\tau)$, and $C'_{p,MRF}(\tau, \text{FOM})$ for all materials spotted by MRF along with literature values for C_p from conventional loose-abrasive polishing on a polyurethane pad. The coefficients are calculated from $\text{VRR}_{\text{MRF}}/A_s$, as discussed above. The calculated $C'_{p,MRF}(F_n)$ varies from as low as 1.2×10^{-4} GPa⁻¹ for FS to as high as 8.8×10^{-4} GPa⁻¹ for LHG8, nearly an 8 \times increase. $C'_{p,MRF}(\tau)$ has a smaller range, however, of about 5 \times , from 2.6×10^{-4} GPa⁻¹ for FS to 1.4×10^{-3} GPa⁻¹ for LHG8. Substituting shear stress for pressure narrows the range of Preston's coefficient; however, because of the absence of material properties, there is still a significant variance in $C'_{p,MRF}(\tau)$. Combining shear stress with mechanical properties results in a much tighter range of the coefficient $C'_{p,MRF}(\tau, \text{FOM})$ from 1.6×10^{-4} GPa⁻¹ for FS up to 2.0×10^{-4} GPa⁻¹ for BK7, only a single variance in magnitude. The coefficient $C'_{p,MRF}(\tau, \text{FOM})$ varies by only $\pm 12\%$ among LHG8, BK7, and FS, which may be attributable to the particular surface condition and specific material composition.

Table 117.III: Preston's coefficient for conventional chemical mechanical polishing processes from literature and modified Preston's coefficients calculated for MRF from this work.

Material	C_p (GPa ⁻¹)	$C'_{p,MRF}(F_n)$ (GPa ⁻¹)	$C'_{p,MRF}(\tau)$ (GPa ⁻¹)	$C'_{p,MRF}(\tau, FOM)$ (MPa)
LHG8	–	8.8×10^{-4}	1.4×10^{-3}	1.6×10^{-4}
BK7	8.3×10^{-4} (a) 10.7×10^{-4} (b)	3.4×10^{-4}	5.6×10^{-4}	2.0×10^{-4}
FS	1.7×10^{-4} (a) 3.3×10^{-4} (b)	1.2×10^{-4}	2.6×10^{-4}	1.6×10^{-4}
Variance in magnitude ^(c)	–	8×	5×	≪1×

^(a)From Izumitani,^{24,25} using conventional loose-abrasive lapping, CeO₂ abrasives and polyurethane pad, $p = 20$ KPa, $V = 0.5$ m/s.

^(b)From Cumbo,²⁶ using conventional loose-abrasive lapping, CeO₂ abrasives and polyurethane pad, $p = 5$ KPa, $V = 0.11$ m/s.

^(c)Variance in magnitude is defined by dividing the largest value in the column by the smallest value.

Conclusions

This work reports for the first time on *in-situ* measurements of drag and normal forces in MRF. Three optical glasses ranging in hardness and chemical composition were tested. A spot-taking machine (STM) was used as a test bed for MRF spotting experiments. We examined how the measurable drag and normal forces, and the calculated shear stress as a function of material mechanical properties, contribute to material removal in MRF. A modified Preston's equation, combining shear stress with material mechanical properties, is proposed, which suggests that material removal is dominated by the material mechanical properties. Our main observations are summarized as follows:

- Normal force was measured simultaneously with drag force in MRF for the first time. Normal force was within the range of 6 to 9 N, whereas drag force was within the range of 4 to 5 N. These results are in good agreement with the literature, where either one of these forces was measured individually, but not simultaneously.
- It was confirmed experimentally that the hydrostatic pressure [normal force divided by the projected spot area F_n/A_s , first term of Eq. (1) (see data in Table 117.II and Fig. 117.45)] does not predict the material removal rate in MRF. It was found for the first time that the measured normal force is dependent on material hardness.
- It was also demonstrated for the first time how the calculated shear stress (drag force divided by the projected spot area on

the part) governs the volumetric removal rate, not drag force alone. This experimentally confirms Shorey's⁴ predictions that material removal in MRF is dominated by shear.

- For the glasses tested under the STM geometry and conditions reported here, it was found that there is a threshold for shear stress below which a removal rate becomes negligible. In order to effectively remove material in MRF, shear stress should be kept above ~ 0.08 MPa by adjusting the process parameters. Additional work is required to identify what process parameters affect shear stress, such as the size of the projected spot area on the part. Our results show that drag force is within a range of ~ 4 to 5 N for a range of optical glass materials, ranging from relatively "soft" LHG8 to hard FS. Therefore, by keeping a spot area < 50 mm² while keeping drag force in the range reported above, one should expect efficient material removal in MRF for glasses.
- Preston's coefficient was calculated for MRF in terms of the hydrostatic pressure, shear stress, and a combination of a material's figures of merit and shear stress. These calculated coefficients indicate a narrow range for our modified Preston's coefficient when both material figures of merit and shear stress are considered for a range of optical glasses, providing predictive capabilities for new glasses. Therefore, we conclude that material removal in MRF for optical glasses is governed by a material's mechanical properties and shear stress.

ACKNOWLEDGMENT

The authors thank Alex Maltsev and Mike Kaplun of the Laboratory for Laser Energetics (LLE) for their help with sample preparation. The authors also thank Scott Russell of the Department of Mechanical Engineering at the University of Rochester for his help with the LabVIEW software. The authors acknowledge the Laboratory for Laser Energetics (LLE) at the University of Rochester for continuing support. One of the authors (C. Miao) is an LLE Horton Fellow.

Research was sponsored by the U. S. Army Armament, Research, Development and Engineering Center (ARDEC) and was accomplished under Cooperative Agreement Number W15QKN-06-2-0104 and the U.S. Department of Energy Office of Inertial Confinement Fusion under Cooperative Agreement No. DE-FC52-08NA28302, the University of Rochester, and the New York State Energy Research and Development Authority. The views and conclusions contained in this document are those of the authors and should not be interpreted as representing the official policies, either expressed or implied, of U.S. Army ARDEC or the U.S. Government. The support of DOE does not constitute an endorsement by DOE of the views expressed in this article. The U.S. Government is authorized to reproduce and distribute reprints for Government purposes notwithstanding any copyright notation hereon.

REFERENCES

1. S. D. Jacobs, D. Golini, Y. Hsu, B. E. Puchebner, D. Strafford, Wm. I. Kordonski, I. V. Prokhorov, E. Fess, D. Pietrowski, and V. W. Kordonski, in *Optical Fabrication and Testing*, edited by T. Kasai (SPIE, Bellingham, WA, 1995), Vol. 2576, pp. 372–382.
2. S. D. Jacobs, S. R. Arrasmith, I. A. Kozhinova, L. L. Gregg, A. B. Shorey, H. J. Romanofsky, D. Golini, W. I. Kordonski, P. Dumas, and S. Hogan, in *Finishing of Advanced Ceramics and Glasses*, edited by R. Sabia, V. A. Greenhut, and C. G. Pantano, Ceramic Transactions, Vol. 102 (The American Ceramic Society, Westerville, OH, 1999), pp. 185–199.
3. F. W. Preston, *J. Soc. Glass Technol.* **XI**, 214 (1927).
4. A. B. Shorey, “Mechanisms of Material Removal in Magnetorheological Finishing (MRF) of Glass,” Ph.D. thesis, University of Rochester, 2000.
5. V. H. Bulsara *et al.*, *Trans. ASME, J. Appl. Mech.* **65**, 410 (1998).
6. V. W. Kordonski and D. Golini, in *Proceedings of the Sixth International Conference on Electro-Rheological Fluids, Magneto-Rheological Suspensions and Their Applications*, edited by M. Nakano and K. Koyama (World Scientific, Singapore, 1998), pp. 837–844.
7. D. Golini, H. Pollicove, G. Platt, S. Jacobs, and W. Kordonski, *Laser Focus World* **31**, 83 (1995).
8. A. B. Shorey, S. D. Jacobs, W. I. Kordonski, and R. F. Gans, *Appl. Opt.* **40**, 20 (2001).
9. J. E. DeGroot, “Surface Interactions Between Nanodiamonds and Glass in Magnetorheological Finishing (MRF),” Ph.D. thesis, University of Rochester, 2007.
10. J. E. DeGroot, A. E. Marino, J. P. Wilson, A. L. Bishop, J. C. Lambropoulos, and S. D. Jacobs, *Appl. Opt.* **46**, 7927 (2007).
11. C. Miao, S. N. Shafir, H. Romanofsky, J. Mici, J. C. Lambropoulos, and S. D. Jacobs, in *Optical Fabrication and Testing*, OSA Technical Digest (CD) (Optical Society of America, Washington, DC, 2008), Paper OTThB4.
12. J. C. Lambropoulos, S. D. Jacobs, and J. Ruckman, in *Finishing of Advanced Ceramics and Glasses*, edited by R. Sabia, V. A. Greenhut, and C. G. Pantano, Ceramic Transactions, Vol. 102 (The American Ceramic Society, Westerville, OH, 1999), pp. 113–128.
13. A. G. Evans, in *Fracture Mechanics Applied to Brittle Materials*, edited by S. W. Freiman (American Society for Testing and Materials, Philadelphia, 1979), Vol. ASTM STP 678, Part 2, pp. 112–135.
14. Zygo Mark IVxp™, Zygo Corporation, Middlefield, CT 06455. This instrument is a 4-in. HeNe Fizeau interferometer with a wavelength of 632.8 nm. Peak-to-valley (p–v) for surface flatness and depth of deepest penetration (ddp) of the spot was measured in microns.
15. Zygo NewView 5000 noncontact white light interferometer, Zygo Corporation, Middlefield, CT 06455. Average microroughness data (peak-to-valley, p–v, and root-mean-square, rms) were obtained under the following conditions: 20× Mirau objective; high FDA Res.; 20- μ m bipolar scan length; Min/Mod: 5%, unfiltered. This instrument has a lateral resolution of $\sim 1 \mu\text{m}$ and a vertical resolution of $\sim 0.3 \text{ nm}$.
16. Single-axis slim-line compressive (K9133B21) force sensor measuring system, Kistler Instrument Corp., Amherst, NY 14228-2171.
17. Single-axis slim-line shear (K9143B21) force sensor measuring system, Kistler Instrument Corp., Amherst, NY 14228-2171.
18. The LabVIEW data-collecting program (National Instruments Corporation, Austin, TX 78759-3504) was written by S. Russell and S. N. Shafir of the University of Rochester, Rochester, NY (2008).
19. MetroPro Reference Guide, OMP-0347, Zygo Corporation, Middlefield, CT 06455.
20. M. Schinhaerl *et al.*, in *Current Developments in Lens Design and Optical Engineering IX*, edited by P. Z. Mouroulis, W. J. Smith, and R. B. Johnson (SPIE, Bellingham, WA, 2008), Vol. 7060, p. 706006.
21. B. Bhushan and B. K. Gupta, in *Handbook of Tribology: Materials, Coatings, and Surface Treatments* (Krieger Publishing Company, Malabar, FL, 1997), Chap. 2, Table 2.1, p. 2.11.
22. J. Steigerwald, S. P. Murarka, and R. J. Gutmann, *Chemical Mechanical Planarization of Microelectronic Materials* (Wiley, New York, 1997).
23. J. C. Lambropoulos, S. Xu, and T. Fang, *Appl. Opt.* **36**, 1501 (1997).
24. T. S. Izumitani, in *Optical Fabrication and Testing*, OSA Technical Digest (Optical Society of America, Washington, DC, 1982), pp. 1–4.
25. T. S. Izumitani, in *Optical Fabrication and Testing Workshop*, OSA Technical Digest (Optical Society of America, Washington, DC, 1984), pp. TuB-A1-1–TuB-A1-3.
26. M. J. Cumbo, “Chemo-Mechanical Interactions in Optical Polishing (Glass Finishing),” Ph.D. thesis, University of Rochester, 1993.

Effective Verdet Constant in Terbium-Doped-Core Phosphate Fiber

Faraday rotators are widely used in optical isolators, circulators, Faraday mirrors, and magnetic/current field sensors. Traditional Faraday rotators are based on bulk optics, which require optical coupling for use with fiber-optic systems. Optical fibers continue to be the platform of choice in many optics fields, making the development of all-fiber Faraday rotation components highly desirable. This is particularly true for high-power fiber laser systems, where fiber termination and small free-space beams place restrictions on how much power can be transported through such components in order to avoid damage at optical interfaces.

Several standard silica-fiber Faraday rotators have been reported¹⁻⁴ but are relatively impractical because of long fiber lengths. The small Verdet constant in standard silica fiber, which translates to a long fiber length, makes it difficult to realize all-fiber Faraday rotators. The Verdet constant is only about 1 rad/Tm at 1064 nm in silica, compared with 40 rad/Tm in terbium gallium garnet (TGG) crystals often used in bulk optics.⁵ As an example, if the magnetic field is 0.2 T, the silica fiber length required for a 45° rotation is around 4 m. To maintain a constant orientation of the magnetic field along the entire axial length, the fiber cannot be coiled. This creates an impractical requirement that the magnet structure be as long as the fiber.

To overcome this limitation, Shiraishi⁶ reported the fabrication of a high-Verdet-constant (21× greater than silica fiber) optical fiber using Hoya FR-5 (terbium borosilicate) glass, where both the core and the cladding were doped with terbium (Tb). Ballato and Snitzer⁷ also reported the fabrication of a 54-wt%-terbium-doped optical fiber, measuring the Verdet constant on bulk samples to be 20× higher than silica fiber.

Doping with high-Verdet-constant materials, such as terbium, can be an effective way to increase the total Verdet constant in optical fiber. The Verdet constant experienced by an optical field is different, however, from the material Verdet constants in the core and cladding when they are made of different materials. The results described above did not measure or

predict this effect. The first experimental proof of the effective Verdet constant theory is presented in this article. The effective Verdet constant in a phosphate fiber that is terbium doped in the core only is measured. The experimental results agree well with theory and describe how the effective Verdet constant differs from the value measured from the bulk samples.

The Verdet constant experienced by light in an optical fiber is different from that in bulk glass. In bulk glass, the Verdet constant is normally uniform everywhere. In optical fiber, the core and cladding have different Verdet constants since they are typically made of different materials. Only a portion of the guided mode exists in the core of the fiber waveguide. Thus, the effective Verdet constant V_{eff} is defined as the Verdet constant experienced by the optical mode in the fiber,

$$V_{\text{eff}} = V_{\text{core}}\Gamma + V_{\text{clad}}(1 - \Gamma), \quad (1)$$

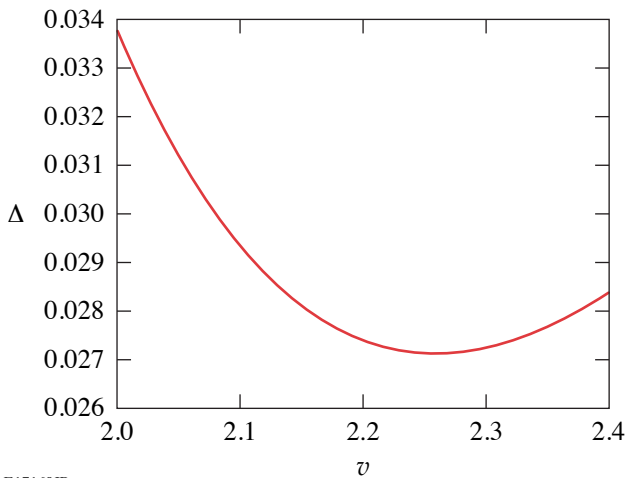
where V_{core} and V_{clad} are the Verdet constants in the core and cladding, respectively, and the confinement factor $\Gamma = P_{\text{core}}/P_{\text{tot}}$ represents the ratio of the power contained in the core, P_{core} , to total power P_{tot} . The confinement factor Γ can be calculated directly by assuming that the fundamental mode profile is Gaussian, $\Gamma = 1 - \exp(-2/\xi^2)$. The ratio of beam-spot size to fiber radius ξ is usually approximated by

$$\xi \approx 0.65 + 1.619 v^{-3/2} + 2.879 v^{-6}, \quad (2)$$

which is accurate to within 1% for $1.2 \leq v \leq 2.4$, where v is the normalized frequency (or V number).⁸ Equation (1) for the effective Verdet constant has a straightforward physical meaning: the Verdet constant includes two parts contributing from the core and the cladding, weighted by the mode overlap in each region.

In recent theoretical work,⁹ the rotation of an optical field in a fiber was derived using Maxwell's equations with a magnetic field applied along the axial direction of the fiber. An empirical equation, which has a relative error of 2% for $1 \leq v \leq 3$, was used to approximate the propagation constant. Using these results,

one can derive the effective Verdet constant directly from the circular birefringence of the propagation constant. After algebraic manipulation, this derivation produces an effective Verdet constant given by $V_{\text{eff}}^{\text{Yoshino}} = V_{\text{core}}\alpha + V_{\text{clad}}(1 + \alpha)$, where the factor $\alpha = 1.306 - 1.138/v$ and is a dimensionless constant. Figure 117.46 shows the relative difference $\Delta = (\alpha - \Gamma)/\alpha$ between factors Γ and α as a function of normalized frequency v . In the region $2 < v < 2.4$, where most single-mode fibers are designed, Δ is less than 4%. Considering that both models use empirical equations during derivation, such a difference is reasonable. Therefore, although not indicated in Ref. 9, the factor α should have the same physical meaning as Γ , representing the light confinement in the core. This indicates that Eq. (1) can also be derived via rigorous electromagnetic calculations.



E17160JR

Figure 117.46 Normalized difference between factors Γ and α for a single-mode fiber as a function of normalized frequency v .

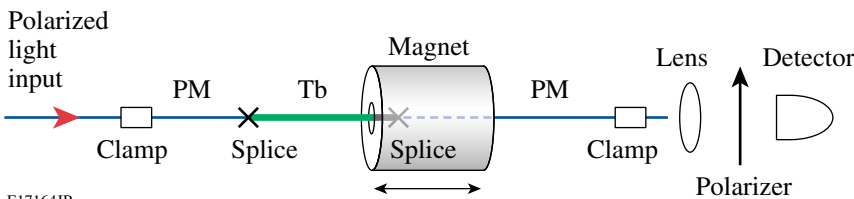
The phosphate optical fiber used in these experiments was fabricated at NP Photonics.¹⁰ It is 25-wt% terbium doped in the single-mode core [numerical aperture (N.A.) = 0.147] and 6-wt% lanthanum doped in the cladding to provide the appropriate core N.A. Core and cladding diameters are $4.5 \mu\text{m}$ and $120 \mu\text{m}$, respectively, and the propagation loss is 0.12 dB/cm

at 980 nm. The Verdet constant is measured at 1053 nm and room temperature using the experimental configuration shown in Fig. 117.47. A 4-cm section of Tb-doped phosphate fiber, spliced between two polarization-maintaining (PM) fibers, goes through a magnet tube. Linearly polarized, 1053-nm light is launched into the fiber, and the polarization direction of the output light is monitored. The N48 NdFeB magnet tube is 4 cm long with inner and outer diameters of 5 mm and 6 cm, respectively. As the magnet is translated along the fiber, the magnetic field imposed on the Tb fiber is changed. By measuring the rotation angle as a function of the magnet's position on the fiber axis, V_{eff} can be extracted, provided the magnetic field is known.

Magnetic fields can be readily calculated by using the geometrical shape of the magnet.¹¹ The axial component of the magnetic-field distribution along the central axis of the magnet tube is derived to be

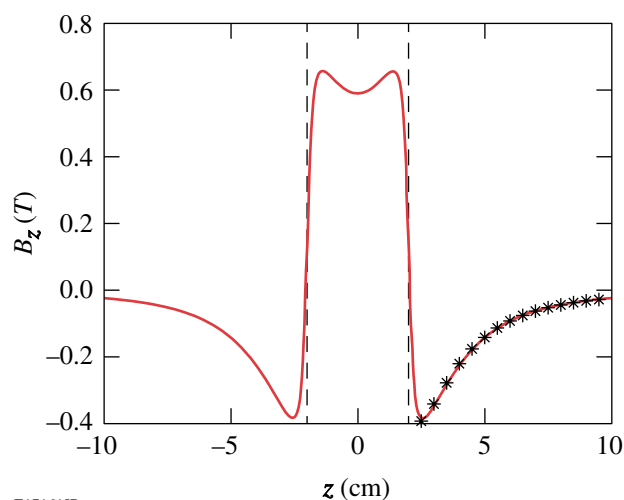
$$B_z(z) = \frac{B_r}{2} \left\{ \frac{z+l/2}{\left[a_1^2 + (z+l/2)^2 \right]^{1/2}} - \frac{z+l/2}{\left[a_2^2 + (z+l/2)^2 \right]^{1/2}} - \frac{z-l/2}{\left[a_1^2 + (z-l/2)^2 \right]^{1/2}} + \frac{z-l/2}{\left[a_2^2 + (z-l/2)^2 \right]^{1/2}} \right\}, \quad (3)$$

where a_1 and a_2 are the inner and outer radii, respectively, l is the length of the magnet, and B_r is the residual magnetic flux density. Figure 117.48 shows the calculated $B_z(z)$ for the N48 magnet used in the experiment ($B_r = 1.35T$) along with the measured magnetic field outside the magnet. The physical ends of the magnet are also shown for reference. The magnetic field, measured only outside the magnet because the probe size is larger than a_1 , agrees very well with the theoretical curve calculated from Eq. (3). The magnetic field has different directions inside and outside the magnet, such that the total integrated field along the z axis is zero, i.e., $\int_{-\infty}^{+\infty} B_z(z) dz = 0$, resulting from Ampère's law. This means that if a sufficiently long piece of fiber with axially uniform V_{eff} goes through the



E17164JR

Figure 117.47 Experimental configuration of the Faraday rotation measurement.



E17161JR

Figure 117.48

Theoretical (solid) and measured (star) magnetic density flux distribution B_z along the center axis z ; dashed lines represent the magnet ends.

magnet, the rotation angles inside and outside the magnet counteract each other and the total rotation angle is zero. If the fiber consists of i different sections of length L_i , the total rotation angle $\Delta\theta_{\text{tot}}$ can be written as a sum of the rotation in each section $\Delta\theta_i$, given by

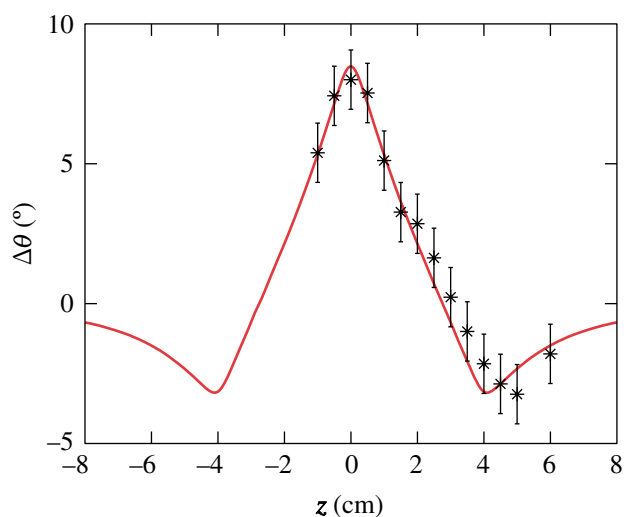
$$\Delta\theta_{\text{tot}} = \sum_i \Delta\theta_i = \sum_i V_{\text{eff}}^i \int_{L_i} B_z(z) dz, \quad (4)$$

where V_{eff}^i and $\int_{L_i} B_z(z) dz$ are the effective Verdet constant and the line integral of the magnetic field in each section, respectively. For the experimental configuration shown in Fig. 117.47, Eq. (4) can be simplified as

$$\Delta\theta_{\text{tot}} = V_{\text{eff}}^{\text{Tb}} \int_{L_{\text{Tb}}} B_z(z) dz + V_{\text{eff}}^{\text{PM}} \int_{L_{\text{PM}}} B_z(z) dz, \quad (5)$$

where the two terms represent the Verdet constant of and the integration over the Tb-doped and PM fibers, respectively. $V_{\text{eff}}^{\text{PM}}$ can be neglected in our experiment because the large linear birefringence in PM fiber suppresses Faraday rotation.

In the experiment, the magnet is axially translated in 5-mm steps. At each step, the direction of the major polarization axis is measured; the power is measured as the polarizer in front of the detector is rotated, and the polarization direction is extracted by fitting this data to a cosine-squared function. Figure 117.49 shows the measured rotation angle and the corresponding curve fit at 1053 nm along the central axis. The error



E17165JR

Figure 117.49

Measured (star) rotation angle and corresponding curve fit (solid) at 1053 nm along the center axis z .

in the measured angle is primarily caused by air flow, and it is determined to be 1° by a polarization stability measurement. The curve fit is obtained by adjusting $V_{\text{eff}}^{\text{Tb}}$, yielding a measured Verdet constant of $V_{\text{measure}} = -6.2 \pm 0.4$ rad/Tm. This value is $6\times$ higher than that of the silica and demonstrates the potential for compact all-fiber Faraday rotators.

The bulk value of the Tb-doped core is calculated from Ref. 7 to be $V_{\text{core}} = -9.3$ rad/Tm, assuming a linear dependence on the terbium ion concentration. Since no Verdet constant data are available in the near-infrared region for the lanthanum-doped phosphate glass used in the cladding, the value is approximated based on two observations: First, the Verdet constant dispersion curve of the lanthanum-doped phosphate glass is roughly 0.8 rad/Tm higher than the curve for SiO_2 in the visible region.^{12,13} Assuming a similar trend in the near-infrared region, the Verdet constant of the lanthanum-doped phosphate glass should be 0.8 rad/Tm larger than that of the SiO_2 . Second, the rare-earth element present in the host material is the dominating factor in determining the Verdet constant. For example, the Verdet constant of the terbium aluminosilicate is similar to that of the terbium phosphate.¹³ Therefore, the Verdet constant of the crystal lanthanum fluoride (LaF_3) measured at 1064 nm (Ref. 12) should also be similar to that of lanthanum phosphate. Both of these observations lead to a value of $V_{\text{clad}} = 1.8$ rad/Tm. Using these values for the core and cladding Verdet constants, the theoretical models predict $V_{\text{eff}} = -6.0$ rad/Tm and $V_{\text{eff}}^{\text{Yoshino}} = -6.3$ rad/Tm, the differ-

ence between the models resulting from the approximations contained in each. They both agree well with the experimental result, which differs substantially from the bulk core value of -9.3 rad/Tm due to the mode confinement properties of the fiber, as described above. This measurement validates the theory of the effective Verdet constant.

Several methods can be used to increase the effective Verdet constant for compact all-fiber Faraday rotators. For example, the same high-Verdet-constant material can be doped in both the core and the cladding. In this case, the V_{eff} will be equal to the material's Verdet constant. If the high-Verdet-constant material is doped only in the core, the N.A. and the core diameter can be increased (while maintaining a V number less than 2.405) to confine more light in the core, therefore increasing V_{eff} . Other rare-earth elements besides terbium can also be doped. For example, praseodymium and dysprosium also have Verdet constants much higher than silica.

In conclusion, the first experimental validation of the effective Verdet constant theory has been reported. The effective Verdet constant of light propagation in a fiber includes contributions from the materials in both the core and the cladding. It is measured in a 25-wt%-terbium-doped-core phosphate fiber to be -6.2 ± 0.4 rad/Tm at 1053 nm, which is $6\times$ larger than silica fiber. The result agrees well with the Faraday rotation theory in optical fibers.

ACKNOWLEDGMENT

This work was supported by the U.S. Department of Energy Office of Inertial Confinement Fusion under Cooperative Agreement No. DE-FC52-08NA28302, the University of Rochester, and the New York State Energy Research and Development Authority. The support of DOE does not constitute an endorsement by DOE of the views expressed in this article.

REFERENCES

1. E. H. Turner and R. H. Stolen, *Opt. Lett.* **6**, 322 (1981).
2. G. W. Day *et al.*, *Opt. Lett.* **7**, 238 (1982).
3. J.-F. Lafortune and R. Vallée, *Opt. Commun.* **86**, 497 (1991).
4. V. Annovazzi-Lodi, S. Merlo, and A. Leona, *J. Lightwave Technol.* **13**, 2349 (1995).
5. E. Khazanov *et al.*, *Appl. Opt.* **41**, 483 (2002).
6. K. Shiraiishi, S. Sugaya, and S. Kawakami, *Appl. Opt.* **23**, 1103 (1984).
7. J. Ballato and E. Snitzer, *Appl. Opt.* **34**, 6848 (1995).
8. G. P. Agrawal, *Lightwave Technology: Components and Devices* (Wiley, Hoboken, NJ, 2004).
9. T. Yoshino, *J. Opt. Soc. Am. B* **22**, 1856 (2005).
10. NP Photonics, Inc., Tucson, AZ 85747, <http://www.npphotonics.com>.
11. M. McCaig and A. G. Clegg, *Permanent Magnets in Theory and Practice*, 2nd ed. (Wiley, New York, 1987).
12. D. R. Lide, *CRC Handbook of Chemistry and Physics*, 82nd ed. (CRC Press, Boca Raton, FL, 2001).
13. M. J. Weber ed., *CRC Handbook of Laser Science and Technology*, edited by M. J. Weber, Supplement 2: Optical Materials (CRC Press, Boca Raton, FL, 1995), Sec. 9.

Publications and Conference Presentations

Publications

- Z. A. Ali, V. Yu. Glebov, M. Cruz, T. Duffy, C. Stoeckl, S. Roberts, T. C. Sangster, R. Tommasini, A. Throop, M. Moran, L. Dauffy, and C. Horsefield, "Tests and Calibration of NIF Neutron Time of Flight Detectors," *Rev. Sci. Instrum.* **79**, 10E527 (2008).
- S.-W. Bahk, J. D. Zuegel, J. R. Fienup, C. C. Widmayer, and J. Heebner, "Spot-Shadowing Optimization to Mitigate Damage Growth in a High-Energy-Laser Amplifier Chain," *Appl. Opt.* **47**, 6586 (2008).
- Z.-M. Bei, T. B. Jones, A. Tucker-Schwartz, and D. R. Harding, "Electric Field Mediated Droplet Centering," *Appl. Phys. Lett.* **93**, 184101 (2008).
- J. L. Bourgade, P. Troussel, A. Casner, G. Huser, T. C. Sangster, G. Pien, F. J. Marshall, J. Fariaud, C. Remond, D. Gontier, C. Chollet, C. Zuber, C. Reverdin, A. Richard, P. A. Jaanimagi, R. L. Keck, R. E. Bahr, W. J. Armstrong, J. DeWandel, R. Maroni, F. Aubard, B. Angelier, C. Y. Cote, and S. Magnan, "A Versatile High-Resolution X-Ray Imager (HRXI) for Laser-Plasma Experiments on OMEGA," *Rev. Sci. Instrum.* **79**, 10E904 (2008).
- J. Bromage, S.-W. Bahk, D. Irwin, J. Kwiatkowski, A. Pruyne, M. Millecchia, M. Moore, and J. D. Zuegel, "A Focal-Spot Diagnostic for On-Shot Characterization of High-Energy Petawatt Lasers," *Opt. Express* **16**, 16,561 (2008).
- B. Ciftcioglu, J. Zhang, L. Zhang, J. R. Marciante, J. D. Zuegel, R. Sobolewski, and H. Wu, "3-GHz Silicon Photodiodes Integrated in a 0.18- μm CMOS Technology," *IEEE Photon. Technol. Lett.* **20**, 2069 (2008).
- V. Yu. Glebov, M. Moran, C. Stoeckl, T. C. Sangster, and M. Cruz, "Neutron Bang Time Detector Based on a Light Pipe," *Rev. Sci. Instrum.* **79**, 10E528 (2008).
- E. T. Gumbrell, A. S. Moore, J. A. Lazarus, E. L. Clark, P. M. Nilson, W. J. Garbett, A. J. Comley, J. S. Robinson, M. Hohenberger, R. D. Edwards, R. E. Eagleton, R. J. Clarke, D. R. Symes, and R. A. Smith, "Laser Heating of Large Noble Gas Clusters: From the Resonant to the Relativistic Interaction Regimes," *New J. Phys.* **10**, 123011 (2008).
- D. G. Hicks, T. R. Boehly, P. M. Celliers, D. K. Bradley, J. H. Eggert, R. S. McWilliams, R. Jeanloz, and G. W. Collins, "High Precision Measurements of the Diamond Hugoniot In and Above the Melt Region," *Phys. Rev. B* **78**, 174102 (2008).
- C. Kim, K. L. Marshall, J. U. Wallace, and S. H. Chen, "Photochromic Glassy Liquid Crystals Comprising Mesogenic Pendants to Dithienylethene Cores," *J. Mater. Chem.* **18**, 5592 (2008).
- D. Pan, G. P. Pepe, V. Pagliarulo, C. De Lisio, L. Parlato, M. Khafizov, I. Komissarov, and R. Sobolewski, "Layered Ferromagnet/Superconductor Heterostructures: Nonequilibrium Quasiparticle Dynamics and Photodetector Applications," *Phys. Rev. B* **78**, 174503 (2008).
- S. N. Shafir, S. D. Jacobs, S. Adar, C. Miao, H. Romanofsky, and J. C. Lambropoulos, "Drag Force and Surface Texture in Material Removal with MRF on Optical Glass and Hard Ceramics," in the *Proceedings of the 12th DoD Electromagnetic Windows Symposium* (U.S. Army Research, Development, and Engineering Center, Redstone Arsenal, AL, 2008), pp. 1–23.
- A. A. Solodov, K. S. Anderson, R. Betti, V. Gotcheva, J. Myatt, J. A. Delettrez, S. Skupsky, W. Theobald, and C. Stoeckl, "Simulations of Electron Transport and Ignition for Direct-Drive Fast-Ignition Targets," *Phys. Plasmas* **15**, 112702 (2008).

C. Stoeckl, K. S. Anderson, R. Betti, T. R. Boehly, J. A. Delettrez, J. A. Frenje, V. N. Goncharov, V. Yu. Glebov, J. H. Kelly, A. J. MacKinnon, R. L. McCrory, D. D. Meyerhofer, S. F. B. Morse, J. F. Myatt, P. A. Norreys, P. M. Nilson, R. D. Petrasso, T. C. Sangster, A. A. Solodov, R. B. Stephens, M. Storm, W. Theobald, B. Yaakobi, L. J. Waxer, and C. D. Zhou, "Fast-Ignition Target Design and Experimental-Concept Validation on OMEGA," *Plasma Phys. Control. Fusion* **50**, 124044 (2008) (invited).

M. Storm, I. A. Begishev, R. J. Brown, C. Guo, D. D. Meyerhofer, C. Mileham, J. F. Myatt, P. M. Nilson, T. C.

Sangster, C. Stoeckl, W. Theobald, and J. D. Zuegel, "A High-Resolution Coherent Transition Radiation Diagnostic for Laser-Produced Electron Transport Studies," *Rev. Sci. Instrum.* **79**, 10F503 (2008) (invited).

A. Trajkovska Petkoska and S. D. Jacobs, "Effect of Different Dopants on Polymer Cholesteric Liquid Crystal Flakes," *Mol. Cryst. Liq. Cryst.* **495**, 334 (2008).

C. D. Zhou and R. Betti, "A Measurable Lawson Criterion and Hydro-Equivalent Curves for Inertial Confinement Fusion," *Phys. Plasmas* **15**, 102707 (2008).

Forthcoming Publications

E. Bambrink, H. G. Wei, B. Brabrel, P. Audebert, A. Benuzzi, T. Boehly, T. Endo, C. Gregory, T. Kimura, R. Kodama, N. Ozaki, M. Rabec le Gloahec, and M. Koenig, "X-Ray Source Studies for Radiography of Dense Matter," to be published in *Physics of Plasmas*.

T. R. Boehly, D. H. Munro, P. M. Celliers, R. E. Olson, D. G. Hicks, V. N. Goncharov, H. F. Robey, S. X. Hu, J. A. Marozas, T. C. Sangster, O. L. Landen, and D. D. Meyerhofer, "Demonstration of the Shock-Timing Technique for Ignition Targets," to be published in *Physics of Plasmas* (invited).

X. L. Cross, X. Zheng, P. D. Cunningham, L. M. Hayden, Š. Chromik, M. Sojkova, V. Štrbík, P. Odier, and R. Sobolewski, "Pulsed-THz Characterization of Hg-Based, High-Temperature Superconductors," to be published in *IEEE Transactions on Applied Superconductivity*.

C. Dorrer, "Statistical Analysis of Incoherent Pulse Shaping," to be published in *Optics Express*.

V. N. Goncharov, "Ablative Richtmyer–Meshkov Instability: Theory and Experimental Results," to be published in the *Proceedings of the Scottish Summer School*.

V. N. Goncharov, "Direct-Drive Inertial Fusion: Basic Concepts and Ignition Target Designing," to be published in the *Proceedings of the Scottish Summer School*.

W. Guan and J. R. Marciante, "Complete Elimination of Self-Pulsations in Dual-Clad Ytterbium-Doped Fiber Lasers at All Pumping Levels," to be published in *Optics Letters*.

D. G. Hicks, T. R. Boehly, P. M. Celliers, J. H. Eggert, S. J. Moon, D. D. Meyerhofer, and G. W. Collins, "Laser Driven Single Shock Compression of Fluid Deuterium from 45 to 220 GPa," to be published in *Physical Review B*.

Z. Jiang and J. R. Marciante, "Comments on 'Beam Quality Factor of Higher Order Modes in a Step-Index Fiber,'" to be published in the *Journal of Lightwave Technology*.

A. M. Kaplan, G. P. Agrawal, and D. N. Maywar, "All-Optical Flip-Flop Operations of a VCISOA," to be published in *Electronics Letters*.

J. Kitaygorsky, S. Dorenbos, E. Reiger, R. Schouten, V. Zwiller, and R. Sobolewski, "New Read-Out Technique for Dark- and Photon-Count Studies in NbN Superconducting Single-Photon Detectors," to be published in *IEEE Transactions on Applied Superconductivity*.

J. Kitaygorsky, R. Shouten, S. Dorenbos, E. Reiger, V. Zwiller, and R. Sobolewski, "Resolving Dark Pulses from Photon Pulses in NbN Superconducting Single-Photon Detectors," to be published in the *Journal of Modern Optics*.

J. R. Marciante, "Gain Filtering for Single-Spatial-Mode Operation of Large-Mode-Area Fiber Amplifiers," to be published in the *IEEE Journal of Selected Topics in Quantum Electronics*.

P. M. Nilson, W. Theobald, J. F. Myatt, C. Stoeckl, M. Storm, J. D. Zuegel, R. Betti, D. D. Meyerhofer, and T. C. Sangster, "Bulk Heating of Solid-Density Plasmas During High-Intensity Laser–Plasma Interactions," to be published in *Physical Review E*.

G. P. Pepe, D. Pan, V. Pagliarulo, L. Parlato, N. Marrocco, C. De Lisio, G. Peluso, A. Barone, U. Scotti di Uccio, A. Casaburi, F. Tafuri, M. Khafizov, T. Taneda, and R. Sobolewski, "Ultrafast Photoresponse of Superconductor/Ferromagnet Hybrid Nanostructures," to be published in *IEEE Transactions on Applied Superconductivity*.

J. E. Schoenly, W. Seka, and P. Rechmann, "Laser Ablation of Dental Calculus Around 400 nm Using a Ti:Sapphire Laser," to be published in the *Proceedings of SPIE*.

V. A. Smalyuk, R. Betti, T. R. Boehly, R. S. Craxton, J. A. Delettrez, D. H. Edgell, V. Yu. Glebov, V. N. Goncharov,

D. R. Harding, S. X. Hu, J. P. Knauer, F. J. Marshall, R. L. McCrory, P. W. McKenty, D. D. Meyerhofer, P. B. Radha, S. P. Regan, T. C. Sangster, W. Seka, R. W. Short, D. Shvarts, S. Skupsky, J. M. Soures, C. Stoeckl, B. Yaakobi, J. A. Frenje, C. K. Li, R. D. Petrasso, and F. H. Séguin, "Cryogenic Target Performance and Implosion Physics Studies on OMEGA," to be published in *Physics of Plasmas* (invited).

Y. Zhu, J. D. Zuegel, J. R. Marciante, and H. Wu, "Distributed Waveform Generator: A New Circuit Technique for Ultra-Wideband Pulse Generation, Shaping, and Modulation," to be published in the *IEEE Journal of Solid-State Circuits*.

Conference Presentations

R. L. McCrory, "Progress in Direct-Drive Inertial Confinement Fusion," 22nd IAEA Fusion Energy Conference, Geneva, Switzerland 13–18 October 2008.

The following presentations were made at *Frontiers in Optics 2008*, Rochester, NY, 19–23 October 2008:

W. Guan and J. R. Marciante, "Elimination of Self-Pulsations in Dual-Clad, Ytterbium-Doped Fiber Lasers."

W. Guan and J. R. Marciante, "Single-Frequency Hybrid Brillouin/Ytterbium Fiber Lasers."

L. Ji, W. R. Donaldson, and T. Y. Hsiang, "Multi-Wavelength Electro-Optic Pulse Sampling."

Z. Jiang and J. R. Marciante, "Precise Model Decomposition in Multimode Optical Fibers by Maximizing the Sum of Modal Weights."

L. Sun, S. B. Jiang, J. D. Zuegel, and J. R. Marciante, "Measurement of the Verdet Constant in a Terbium-Core-Doped Fiber."

L. J. Waxer, J. H. Kelly, B. E. Kruschwitz, J. Qiao, I. A. Begishev, J. Bromage, C. Dorrer, J. L. Edwards, L. Folsbee, M. J. Guardalben, S. D. Jacobs, R. Jungquist, T. J. Kessler, R. W. Kidder, S. J. Loucks, J. R. Marciante, D. N. Maywar,

R. L. McCrory, D. D. Meyerhofer, S. F. B. Morse, A. V. Okishev, J. B. Oliver, G. Pien, J. Puth, A. L. Rigatti, A. W. Schmid, M. J. Shoup, III, C. Stoeckl, K. A. Thorp, and J. D. Zuegel, "The OMEGA EP High-Energy, Short-Pulse Laser System," *Laser Science XXIV*, Rochester, NY, 19–23 October 2008 (invited).

The following presentations were made at the *Optical Fabrication and Testing Topical Meeting*, Rochester, NY, 19–23 October 2008:

J. H. Kelly, R. Jungquist, L. J. Waxer, M. J. Guardalben, B. E. Kruschwitz, J. Qiao, I. A. Begishev, J. Bromage, C. Dorrer, J. L. Edwards, L. Folsbee, S. D. Jacobs, T. J. Kessler, R. W. Kidder, S. J. Loucks, J. R. Marciante, D. N. Maywar, R. L. McCrory, D. D. Meyerhofer, S. F. B. Morse, A. V. Okishev, J. B. Oliver, G. Pien, J. Puth, A. L. Rigatti, A. W. Schmid, M. J. Shoup, III, K. A. Thorp, and J. D. Zuegel, "Optical Engineering of the OMEGA EP Laser System."

T. J. Kessler, "Surface Artifacts in Manufacturing and Use of Large Imaging Optics" (invited).

C. Miao, S. N. Shafir, H. Romanofsky, J. Mici, J. C. Lambropoulos, and S. D. Jacobs, "Frictional Investigation for Magnetorheological Finishing (MRF) of Optical Glass and Hard Ceramics."

S. Salzman, H. Romanofsky, S. N. Shafir, J. C. Lambropoulos, and S. D. Jacobs, “*In-Situ* Drag Force Measurements in MRF of Optical Glasses.”

S. N. Shafir, C. Miao, H. Romanofsky, J. C. Lambropoulos, and S. D. Jacobs, “Surface Texture in Material Removal with MRF on Optical Ceramics.”

The following presentations were made at the International Conference on Ultrahigh Intensity Lasers, Shanghai-Tongli, China, 27–31 October 2008:

J. Bromage, S.-W. Bahk, D. Irwin, J. Kwiatkowski, A. Pruyne, M. Millecchia, M. Moore, and J. D. Zuegel, “A Focal-Spot Diagnostic for On-Shot Characterization of OMEGA EP.”

J. Bromage, M. Moore, S.-W. Bahk, B. E. Kruschwitz, R. Earley, D. Irwin, D. Canning, R. Jungquist, G. King, J. Kwiatkowski, D. Weiner, M. J. Shoup III, and J. D. Zuegel, “Tools and Techniques for Focusing OMEGA EP.”

C. Dorrer, J. Bromage, and J. D. Zuegel, “High-Dynamic-Range, Single-Shot Cross-Correlator Using a Pulse Replicator.”

T. J. Kessler and H. Huang, “Spatial Chirp Smoothing Within Temporal Pulse Compression.”

J. Qiao, J. H. Kelly, J. Bunkenburg, A. Kalb, D. Canning, and T. Nguyen, “Construction and Activation of Large-Aperture, Tiled-Grating Compressors for High-Energy, Petawatt-Class Chirped-Pulse-Amplification Systems.”

J. Qiao, J. H. Kelly, L. J. Waxer, B. E. Kruschwitz, I. A. Begishev, J. Bromage, S.-W. Bahk, C. Dorrer, J. L. Edwards, L. Folsbee, M. J. Guardalben, S. J. Jacobs, R. Jungquist, T. J. Kessler, R. W. Kidder, S. J. Loucks, J. R. Marciante, D. N. Maywar, R. L. McCrory, D. D. Meyerhofer, S. F. B. Morse, A. V. Okishev, J. B. Oliver, G. Pien, J. Puth, A. L. Rigatti, A. W. Schmid, M. J. Shoup III, C. Stoeckl, K. A. Thorp, and J. D. Zuegel, “Activation of the OMEGA EP High-Energy, Short-Pulse Laser System.”

J. D. Zuegel, C. Dorrer, I. A. Begishev, J. Bromage, R. Brown, A. V. Okishev, P. M. Nilson, W. Theobald, V. Ovchinnikov, J. F. Myatt, B. Eichman, S. Ivancic, M. Storm, O. V. Gotchev, C. Stoeckl, T. C. Sangster, R. Betti, and D. D. Meyerhofer,

“High-Temporal-Contrast Target Experiments Using a Hybrid OPCPA-Nd:Glass Multi-Terawatt (MTW) Laser System.”

The following presentations were made at IEEE LEOS 2008, Newport Beach, CA, 9–13 November 2008:

W. R. Donaldson, J. R. Marciante, and R. G. Roides, “Single-Shot, Electro-Optic Measurements at 10 GHz with a Dynamic Range of 2400:1.”

L. Ji, W. R. Donaldson, and T. Y. Hsiang, “Multi-Wavelength Electro-Optic Pulse Characterization.”

S. P. Regan, B. Yaakobi, R. Epstein, J. A. Delettrez, V. N. Goncharov, H. Sawada, D. D. Meyerhofer, P. B. Radha, T. C. Sangster, V. A. Smalyuk, R. C. Mancini, D. A. Haynes, J. A. Koch, and R. Tommasini, “Applied Plasma Spectroscopy I: Laser Fusion Experiments,” 13th International Workshop on Radiative Properties of Hot Dense Matter, Santa Barbara, CA, 10–14 November 2008.

The following presentations were made at the 50th Annual Meeting of the APS Division of Plasma Physics, Dallas, TX, 17–21 November 2008:

K. S. Anderson, A. A. Solodov, R. Betti, P. W. McKenty, and W. Theobald, “Parametric Study of Direct-Drive, Fuel-Assembly Simulations of Fast-Ignition, Cone-in-Shell Targets.”

M. A. Barrios, D. E. Fratanduono, T. R. Boehly, D. D. Meyerhofer, D. G. Hicks, P. M. Celliers, and J. H. Eggert, “Precision Equation-of-State (EOS) Measurements Using Laser-Driven Shock Waves Using the OMEGA Laser.”

T. R. Boehly, D. H. Munro, P. M. Celliers, R. E. Olson, D. G. Hicks, V. N. Goncharov, H. F. Robey, S. X. Hu, J. A. Marozas, T. C. Sangster, O. L. Landen, and D. D. Meyerhofer, “Demonstration of the Shock-Timing Technique for Ignition Targets” (invited).

D. T. Casey, J. A. Frenje, C. K. Li, F. H. Séguin, M. Manuel, R. D. Petrasso, V. Yu. Glebov, D. D. Meyerhofer, S. Roberts,

- and T. C. Sangster, "Using GEANT4 to Model the Magnetic Recoil Spectrometer (MRS) for Down-Scattered and Primary-Neutron Measurements at OMEGA."
- H. Chen, S. C. Wilks, E. Liang, J. F. Myatt, K. Cone, L. Elbersson, D. D. Meyerhofer, M. Schneider, R. Shepherd, R. Stafford, R. Tommasini, and P. Beiersdorfer, "Making Positrons Using the Titan Short-Pulse Laser."
- T. J. B. Collins, F. J. Marshall, M. J. Bonino, R. Forties, V. N. Goncharov, I. V. Igumenshchev, J. A. Marozas, P. W. McKenty, and V. A. Smalyuk, "3-D Modeling of Planar Target-Mount Perturbation Experiments on OMEGA."
- R. S. Craxton, P. W. McKenty, J. A. Marozas, and A. M. Cok, "Simulations of Polar-Drive NIF Targets Optimized for High Neutron Yields."
- J. A. Delettrez, V. N. Goncharov, A. V. Maximov, J. F. Myatt, P. B. Radha, T. C. Sangster, W. Seka, V. A. Smalyuk, C. Stoeckl, B. Yaakobi, and J. A. Frenje, "Transport of Energetic Electrons Produced from Two-Plasmon Decay in the 1-D Hydrodynamic Code *LILAC*."
- D. H. Edgell, W. Seka, J. A. Delettrez, R. S. Craxton, V. N. Goncharov, I. V. Igumenshchev, J. F. Myatt, A. V. Maximov, R. W. Short, T. C. Sangster, and R. E. Bahr, "Precision Scattered-Laser-Light Spectroscopy in Direct-Drive Implosions."
- R. Epstein, J. A. Delettrez, V. N. Goncharov, S. X. Hu, P. W. McKenty, F. J. Marshall, P. B. Radha, V. A. Smalyuk, W. Theobald, and B. Yaakobi, "Simulation and Optimization of Backlit Images of Cryogenic Implosions on OMEGA."
- D. E. Fratanduono, M. A. Barrios, T. R. Boehly, D. D. Meyerhofer, D. G. Hicks, P. M. Celliers, S. Wilks, and R. Smith, "Optical Properties of Materials at High Pressure Using 'Sandwich' Targets."
- J. A. Frenje, D. T. Casey, C. K. Li, J. R. Rygg, F. H. Séguin, R. D. Petrasso, V. Yu. Glebov, T. C. Sangster, D. D. Meyerhofer, and K. A. Fletcher, "First Measurements of the Down-Scattered and Primary Neutron Spectrum Using the Magnetic Recoil Spectrometer (MRS) at OMEGA."
- M. C. Ghilea, T. C. Sangster, D. D. Meyerhofer, D. J. Lonobile, R. A. Lerche, and L. Disdier, "First Tests on OMEGA of a Bubble Chamber for Neutron Detection."
- V. N. Goncharov, T. C. Sangster, T. R. Boehly, P. B. Radha, R. L. McCrory, D. D. Meyerhofer, and S. Skupsky, "Multiple-Picket, Direct-Drive Target Designs for OMEGA and the NIF."
- O. V. Gotchev, R. Betti, P. Chang, J. P. Knauer, D. D. Meyerhofer, J. A. Frenje, C. K. Li, M. Manuel, R. D. Petrasso, and F. H. Séguin, "Magnetized Hot-Spot Implosions Via Laser-Driven Flux Compression."
- J. D. Hager, V. A. Smalyuk, S. X. Hu, D. D. Meyerhofer, and T. C. Sangster, "Rayleigh–Taylor Measurements in Planar Cryogenic D₂ Targets Using X-Ray Radiography on OMEGA."
- S. X. Hu, P. B. Radha, J. A. Marozas, R. Betti, T. J. B. Collins, R. S. Craxton, J. A. Delettrez, D. H. Edgell, R. Epstein, V. N. Goncharov, I. V. Igumenshchev, J. P. Knauer, F. J. Marshall, R. L. McCrory, P. W. McKenty, D. D. Meyerhofer, S. P. Regan, T. C. Sangster, W. Seka, S. Skupsky, V. A. Smalyuk, C. Stoeckl, B. Yaakobi, and D. Shvarts, "Two-Dimensional Investigation of Neutron-Yield Performance in Direct-Drive, Low-Adiabatic D₂ Implosions on OMEGA."
- I. V. Igumenshchev, F. J. Marshall, J. A. Marozas, V. A. Smalyuk, R. Epstein, T. J. B. Collins, M. J. Bonino, V. N. Goncharov, and T. C. Sangster, "Investigation of the Effects of Target Mounting in Direct-Drive Implosions on OMEGA."
- J. P. Knauer, V. N. Goncharov, J. A. Delettrez, V. Yu. Glebov, F. J. Marshall, J. A. Frenje, C. K. Li, R. D. Petrasso, and F. H. Séguin, "Optimization of Multiple-Picket, Direct-Drive Laser-Pulse Shapes with Foam Shells."
- C. K. Li, "Proton Radiography of Electromagnetic Fields Associated with ICF Implosions and Laser-Irradiated Hohlräume."
- D. Li, V. N. Goncharov, A. V. Maximov, I. V. Igumenshchev, and S. Skupsky, "Modeling of Multiple-Ion Heat Transport in ICF Implosions."
- G. Li, C. Ren, R. Yan, V. N. Goncharov, T. L. Wang, W. B. Mori, and J. Tonge, "Three-Dimensional Effects in Laser Channeling in Fast-Ignition Targets."
- J. A. Marozas, J. D. Zuegel, and T. J. B. Collins, "1.0-MJ CH-Foam Ignition Targets on the NIF Using 1-D Multi-FM SSD with 0.5 THz of Bandwidth."

F. J. Marshall, R. S. Craxton, R. Epstein, V. Yu. Glebov, V. N. Goncharov, J. P. Knauer, P. W. McKenty, D. D. Meyerhofer, P. B. Radha, T. C. Sangster, W. Seka, S. Skupsky, V. A. Smalyuk, J. A. Frenje, C. K. Li, R. D. Petrasso, and F. H. Séguin, “Low-Adiabatic Polar-Drive Implosion Experiments on OMEGA.”

A. V. Maximov, J. F. Myatt, R. W. Short, W. Seka, C. Stoeckl, and J. A. Delettrez, “Modeling of Two-Plasmon-Decay Instability in OMEGA Plasmas.”

D. D. Meyerhofer, J. Bromage, V. Yu. Glebov, J. H. Kelly, B. E. Kruschwitz, S. J. Loucks, R. L. McCrory, S. F. B. Morse, J. F. Myatt, P. M. Nilson, J. Qiao, T. C. Sangster, C. Stoeckl, W. Theobald, R. D. Petrasso, F. H. Séguin, J. A. Frenje, C. K. Li, A. J. MacKinnon, and P. K. Patel, “Initial Experiments Using the OMEGA EP Laser System.”

J. F. Myatt, D. H. Edgell, W. Seka, A. V. Maximov, R. W. Short, D. F. DuBois, D. A. Russell, and H. X. Vu, “Two-Plasmon-Decay Hot-Electron Distributions from Anisotropic Thick-Target Bremsstrahlung Measurements.”

P. M. Nilson, W. Theobald, J. F. Myatt, C. Stoeckl, P. A. Jaanimagi, J. A. Delettrez, M. Storm, R. Betti, D. D. Meyerhofer, T. C. Sangster, J. S. Green, K. L. Lancaster, P. A. Norreys, F. Beg, R. B. Stephens, and M. H. Key, “Fast-Electron-Energy Deposition in Dense Plasma.”

O. Polomarov and R. Betti, “MHD Effects in Laser-Produced Plasmas.”

P. B. Radha, V. N. Goncharov, T. C. Sangster, R. Betti, J. A. Delettrez, S. X. Hu, D. D. Meyerhofer, S. Skupsky, V. A. Smalyuk, C. Stoeckl, J. A. Frenje, C. K. Li, R. D. Petrasso, and D. Shvarts, “Modeling Observables to Diagnose Areal Density in OMEGA Implosions.”

S. P. Regan, T. C. Sangster, D. D. Meyerhofer, W. Seka, R. L. McCrory, C. Stoeckl, V. Yu. Glebov, N. B. Meezan, L. J. Suter, D. J. Strozzi, E. A. Williams, W. L. Kruer, O. S. Jones, D. A. Callahan, M. D. Rosen, O. L. Landen, S. H. Glenzer, C. Sorce, and B. J. MacGowan, “Hohlraum Energetics with a Plastic-Lined Laser Entrance Hole.”

T. C. Sangster, V. N. Goncharov, P. B. Radha, J. A. Delettrez, R. Betti, T. R. Boehly, V. Yu. Glebov, S. X. Hu, J. P. Knauer, F. J. Marshall, R. L. McCrory, P. W. McKenty, D. D. Meyerhofer,

S. P. Regan, V. A. Smalyuk, W. Seka, S. Skupsky, C. Stoeckl, B. Yaakobi, J. A. Frenje, C. K. Li, R. D. Petrasso, F. H. Séguin, and D. Shvarts, “Recent Experimental Results from Cryogenic Implosions on OMEGA.”

H. Sawada, S. P. Regan, P. B. Radha, R. Epstein, D. Li, V. N. Goncharov, S. X. Hu, D. D. Meyerhofer, J. A. Delettrez, P. A. Jaanimagi, V. A. Smalyuk, T. R. Boehly, T. C. Sangster, B. Yaakobi, and R. C. Mancini, “Experimental Investigation of Thermal-Transport Models in Direct-Drive Targets Using X-Ray Absorption Spectroscopy.”

W. Seka, H. A. Baldis, D. H. Edgell, J. F. Myatt, A. V. Maximov, R. S. Craxton, R. W. Short, V. N. Goncharov, A. Simon, and R. E. Bahr, “Two-Plasmon-Decay Instability in Direct-Drive Implosion Experiments.”

R. W. Short, “Two-Plasmon Decay Driven by Multiple Obliquely Incident Laser Beams.”

A. Shvydky, F. J. Marshall, P. W. McKenty, I. V. Igumenshchev, R. Epstein, J. A. Marozas, R. S. Craxton, T. C. Sangster, S. Skupsky, and R. L. McCrory, “Numerical Investigation of OMEGA Saturn Implosions.”

N. Sinenian, J. A. Frenje, C. K. Li, F. H. Séguin, R. D. Petrasso, and J. A. Delettrez, “Measurements of Ablator-Ion Spectra for Preheat and Compression Studies.”

S. Skupsky, V. N. Goncharov, and D. Li, “Nonlocal Ion-Heat and Momentum Transport in ICF Implosions.”

V. A. Smalyuk, R. Betti, T. R. Boehly, R. S. Craxton, J. A. Delettrez, D. H. Edgell, V. Yu. Glebov, V. N. Goncharov, D. R. Harding, S. X. Hu, J. P. Knauer, F. J. Marshall, R. L. McCrory, P. W. McKenty, D. D. Meyerhofer, P. B. Radha, S. P. Regan, T. C. Sangster, W. Seka, R. W. Short, D. Shvarts, S. Skupsky, J. M. Soures, C. Stoeckl, B. Yaakobi, J. A. Frenje, C. K. Li, R. D. Petrasso, and F. H. Séguin, “Cryogenic Target Performance and Implosion Physics Studies on OMEGA” (invited).

A. A. Solodov, K. S. Anderson, R. Betti, V. Gotcheva, J. F. Myatt, J. A. Delettrez, S. Skupsky, W. Theobald, and C. Stoeckl, “Integrated Simulations of Implosion, Electron Transport, and Ignition for Direct-Drive, Fast-Ignition Targets.”

C. Stoeckl, K. S. Anderson, T. R. Boehly, R. Betti, J. A. Delettrez, V. N. Goncharov, V. Yu. Glebov, R. L. McCrory, D. D. Meyerhofer, J. F. Myatt, P. M. Nilson, T. C. Sangster, A. A. Solodov, M. Storm, W. Theobald, B. Yaakobi, C. D. Zhou, J. A. Frenje, R. D. Petrasso, A. J. MacKinnon, P. A. Norreys, and R. B. Stephens, "Advanced Ignition Experiments on OMEGA."

M. Storm, C. Guo, D. D. Meyerhofer, C. Mileham, J. F. Myatt, P. M. Nilson, T. C. Sangster, A. A. Solodov, C. Stoeckl, and W. Theobald, "High-Current Electron Transport Studies Using Coherent Transition Radiation."

W. Theobald, V. Ovchinnikov, B. Eichman, S. Ivancic, P. M. Nilson, C. Stoeckl, J. F. Myatt, J. A. Delettrez, L. Von Woerkom, R. R. Freeman, C. Ren, R. B. Stephens, J. D. Zuegel, and T. C. Sangster, "Intense Laser-to-Fast-Electron Coupling Efficiency in Wedge-Shaped-Cavity Targets."

D. R. Harding, Z. Bei, S. H. Chen, R. Q. Gram, T. Jones, M. Moynihan, and R. Garrell, "Microfluidic Methods for Producing Millimeter-Size Fuel Capsules for Inertial Fusion Energy," 2008 MRS Fall Meeting, Boston, MA, 1–5 December 2008.

